

11-18-2009

Metal-insulator-insulator-metal plasmonic waveguides and devices

Jing Chen

Follow this and additional works at: https://digitalrepository.unm.edu/ece_etds

Recommended Citation

Chen, Jing. "Metal-insulator-insulator-metal plasmonic waveguides and devices." (2009). https://digitalrepository.unm.edu/ece_etds/48

This Dissertation is brought to you for free and open access by the Engineering ETDs at UNM Digital Repository. It has been accepted for inclusion in Electrical and Computer Engineering ETDs by an authorized administrator of UNM Digital Repository. For more information, please contact disc@unm.edu.

Jing Chen

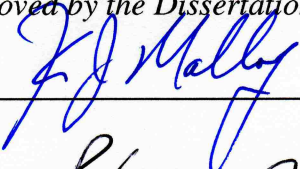
Candidate

Electrical and Computer Engineering

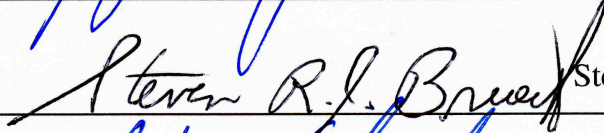
Department

This dissertation is approved, and it is acceptable in quality and form for publication:

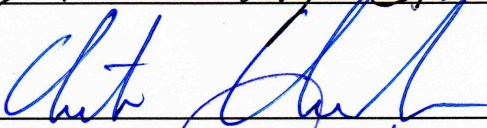
Approved by the Dissertation Committee:



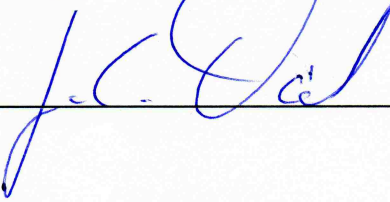
Kevin J. Malloy, Chairperson



Steven R. J. Brueck



Christos Christodoulou



Jean-Claude Diels

**METAL-INSULATOR-METAL PLASMONIC
WAVEGUIDES AND DEVICES**

BY

JING CHEN

B.S., Physics, Hunan Normal University, 1994
M.S., Electromagnetics and Microwave Technology,
Beijing University of Posts and Telecommunications, 1997
M.S., Electrical Engineering, University of New Mexico, 2003

DISSERTATION

Submitted in Partial Fulfillment of the
Requirements for the Degree of

Doctor of Philosophy

Engineering

The University of New Mexico
Albuquerque, New Mexico

August, 2009

©2009, Jing Chen

**To my parents,
my husband Songhe Cai and son Daniel Cai.**

ACKNOWLEDGMENTS

It is my great pleasure to thank all the people that have supported me during my dissertation work and beyond.

First and foremost, I would like to thank my advisor, Professor Kevin Malloy, for his guidance, constant support and encouragements during these years. I am greatly benefited from his knowledge.

I want to express my sincere thanks to Prof. Steve Brueck for his valuable advices. I am grateful to Dr. Gennady Smolyakov for his code. I would also like to thank Dr. Andreas Stintz for his consistent assistance and useful discussions.

I am thankful to Prof. Christos Christodoulou and Prof. Jean-Claude Diels for serving as my committee members.

Thanks to our group members Alexander Albrecht and Felix Jaeckel, your help are greatly appreciated. I am indebted to Zahyun Ku for his aid.

I cannot forget to thank the many support from CHTM staffs. My thanks also go to my friends who help and encourage me.

Finally, it is impossible to achieve this task without the love, supports and encouragements from my parents and husband.

**METAL-INSULATOR-METAL PLASMONIC
WAVEGUIDES AND DEVICES**

BY

JING CHEN

ABSTRACT OF DISSERTATION

Submitted in Partial Fulfillment of the
Requirements for the Degree of

Doctor of Philosophy

Engineering

The University of New Mexico
Albuquerque, New Mexico

August, 2009

METAL-INSULATOR-METAL PLASMONIC WAVEGUIDES AND DEVICES

by

Jing Chen

B.S., Physics, Hunan Normal University, 1994

M.S., Electromagnetics and Microwave Technology,

Beijing University of Posts and Telecommunications, 1997

M.S., Electrical Engineering, University of New Mexico, 2003

Ph.D., Engineering, University of New Mexico, 2009

ABSTRACT

Metal-insulator-metal (MIM) plasmonic waveguides have been proposed for highly integrated subwavelength structures. In this work, waveguiding and coupling of surface plasmon polaritons (SPPs) within finite planar MIM plasmonic waveguides are examined both theoretically and experimentally. Gain (dye-doped polymer)-assisted MIM waveguides and terahertz quantum cascade laser MIM waveguides are numerically analyzed.

The numerical analysis of finite planar MIM waveguides using the transfer matrix formalism reveals both bound and leaky SP modes: three lowest energy bound modes and the highest energy mode consisting of non-radiative (bound) and radiative (leaky) portions separated by a spectral gap at the light line. The leaky regime is further divided

into antenna and reactive mode regions. Spatial dispersion effect on the S_H mode yields a reduced wave vector in its dispersion curve and an increased propagation loss.

The MIM radiative SPPs are probed using attenuated total reflection in the Kretschmann configuration and using free space coupling. Both single- and double-sided leaky waves are analyzed. The leaky wave dispersion relation and its antenna mode radiation pattern are determined through both angle- and wavelength-dependent reflectance of TM polarized free space incident light.

The inclusion of a dye-doped polymer into realistic finite MIM plasmonic waveguides is analyzed. The propagation of three bound SP modes, each within respective optimized symmetric glass-Ag-Rh6G/PMMA-Ag-glass waveguides, is calculated for core material exhibiting optical gain at 594 nm. The critical gain coefficients for lossless propagation of these three bound SP modes are determined. Only lossless propagation of the S_H mode is predicted. For MIM structure with gain in adjacent medium in ATR geometry, the reflectance and energy flux distribution at resonance conditions versus gain coefficients are examined.

The waveguide loss, confinement factor and threshold gain for terahertz quantum cascade laser SP waveguides are modeled from 2 - 7 THz. The effects of plasma layer thickness, plasma doping and substrate thickness and the effects of active region thickness are investigated for semi-insulating surface-plasmon and metal-metal waveguides, respectively. A surface emitting quantum cascade laser SP leaky waveguide are proposed, with emission properties controlled by varying plasma layer thickness.

TABLE OF CONTENTS

LIST OF FIGURES.....	xiii
LIST OF TABLES	xx
CHAPTER 1 INTRODUCTION.....	1
1.1 Introduction.....	1
1.2 Outline of the Dissertation	2
References.....	4
CHAPTER 2 THEORETICAL BACKGROUND.....	7
2.1 Introduction.....	7
2.2 Electromagnetic Complex Waves.....	7
2.3 Waveguide Theory	12
2.3.1 Waveguide Eigenmode	13
2.3.2 Dispersions of Lossless Dielectric Slab Waveguide.....	20
2.4 Dielectric Function of Metals	24
2.4.1 Lorentz Model.....	24
2.4.2 Drude Model	26
2.4.3 Metal Empirical Optical Constants.....	28
2.5 Surface Plasmon Polaritons Basics.....	30
2.5.1 SPPs at a Single Metal-Dielectric Interface.....	31
2.5.2 SPPs in Insulator-Metal-Insulator Waveguide.....	34
2.5.3 SPP Gap Modes in Semi-infinite Metal-Insulator-Metal Waveguide	38
2.5.4 Optical Excitation of Surface Plasmon Polaritons.....	42

References.....	49
CHAPTER 3 BOUND AND LEAKY MODES OF PLANAR FINITE METAL-INSULATOR-METAL PLASMONIC WAVEGUIDES.....	54
3.1 Numerical Method	54
3.2 Code Validation	54
3.3 SPPs in Finite Planar MIM Plasmonic Waveguides.....	54
3.3.1 Dispersion and Spatial Mode Profiles.....	55
3.3.2 Propagation and Confinement Factor	62
3.3.3 Leaky Wave Analysis.....	65
3.4 Spatial Dispersion Effects on MIM SPPs	71
References.....	74
CHAPTER 4 LEAKY MODES IN FINITE PLANAR METAL-INSULATOR-METAL PLASMONIC WAVEGUIDES.....	76
4.1 ATR Kretschmann Coupling	77
4.2 Free Space Coupling.....	82
References.....	86
CHAPTER 5 GAIN-ASSISTED PROPAGATION OF SPPS IN MIM PLASMONIC WAVEGUIDES.....	87
5.1 Numerical Method and Validation with Gain Inclusion.....	88
5.2 Mode Analysis of Gain-Assisted Symmetric MIM Plasmonic Waveguides	91
5.3 Gain-Assisted MIM SPPs Propagation in ATR Geometry.....	98
References.....	107

CHAPTER 6 MIM PLASMONIC WAVEGUIDES IN TERAHERTZ QUANTUM CASCADE LASER.....	111
6.1 Introduction.....	111
6.2 Basics of Quantum Cascade Laser	114
6.2.1 Quantum Casecade Laser Active Region.....	114
6.2.2 Quantum Casecade Laser Waveguides	115
6.3 Electromagnetic Modeling of THz QCL Waveguides.....	118
6.3.1 Semi-infinite Surface Plamson Waveguide Design.....	120
6.3.2 Metal-Metal Waveguide Design	126
6.3.3 THz QCL SP Leaky Waveguide Design.....	129
References.....	132
 CHAPTER 7 CONCLUSIONS AND FUTURE WORKS	135
7.1 Conclusions.....	135
7.2 Suggestions for Future Works.....	136
 APPENDIX A GENERAL ELECTROMAGNETICS THEORY	140
A.1 Maxwell’s Equations.....	140
A.2 Constitutive Relations	141
A.3 Boundary Conditions	141
A.4 The Wave Equation.....	142
 APPENDIX B SURFACE PLASMON POLARITONS AT A SINGLE INTERFACE	147
 APPENDIX C THIN FILM TRANSFER MATRIX METHOD	150

C.1 Transfer Matrix Formulation.....	150
C.2 Application of Transfer Matrix Method in Multilayer Waveguide.....	152
APPENDIX D COMPLEX ROOT SEARCHING: NEWTON-RAPHSON	
METHOD	154
APPENDIX E FUNDAMENTALS OF PLASMA PHYSICS.....	
E.1 Basic Concepts of Plasma Physics	157
E.1.1 Plasmas in Nature	157
E.1.2 Plasma Parameters.....	157
E.1.3 Plasma Frequency and Debye Length.....	160
E.2 Principles of Electrodynamics of Media with Dispersion in Space and Time	162
E.2.1 Dispersion in Time and Space.....	162
E.2.2 Electromagnetic Waves in the Medium.....	163
E.3 Equations of Plasma Dynamics	164
E.3.1 Kinetic Equation with a Field.....	164
E.3.2 Boltzmann Kinetic Equation	165
E.4 Dielectric Permittivity of a Homogeneous Isotropic Plasma.....	166
E.4.1 Dielectric Permittivity of a Collisionless Nondegenerate Plasma.....	168
E.4.2 Dielectric Permittivity of a Collisionless Degenerate Plasma.....	168
E.4.3 Dielectric Permittivity of a Degenerate Plasma Taking Account of Particle Collisions	169
References.....	171

LIST OF FIGURES

Figure 2.1 Constant amplitude (solid lines) and constant phase (dash lines) surfaces of a plane wave propagating in the upper half xz -plane.	9
Figure 2.2 Complex waves in the complex k_x and k_z planes.	11
Figure 2.3 The real and imaginary parts of the complex wave propagation vector in the upper half xz -plane. The yz -plane is the interface plane... ..	12
Figure 2.4 Schematic representation of eigenvalues of the (a) continuum, and (b) improper expansion in the complex longitudinal propagation constant k_z -plane. *'s, discrete bound modes; ■'s, discrete leaky modes; bold solid black and gray lines, continuum radiation modes.	15
Figure 2.5 Field profiles (left) and ray pictures (right) of the four types of mode in the continuum modal basis (panels (a)-(d)) and double-sided leaky mode (panel (e)).....	15
Figure 2.6 Dispersion behaviors for the first two TM-even modes of a symmetric slab waveguide. For the TM_2 mode, the proper real mode and the improper real mode are respectively highlighted by blue and red lines. The waveguide consists of a 2 cm thick dielectric layer with refractive index of $n_0 = 1.5$ sandwiched between two semi-infinite open media with refractive indexes of $n_c = n_s = 1.0$. The imaginary propagation constant is not shown.	22
Figure 2.7 Real and imaginary parts of the optical dielectric constant of Ag using the Brendel–Bormann (BB) (solid curves) and LD (dashed curves) models. Also shown are the selected experimental data points from Dold and Mecke, Winsemius et al., and Leveque et al.	29

Figure 2.8 SPPs at the interface between a metal and a dielectric material arise via the coupling between the TM EM wave and the collective surface charge oscillation31

Figure 2.9 Dispersion relations of SPPs at a single, flat Ag-SiO₂ interface computed using: (a) a free electron gas dispersion model, (b) the empirical optical constants of Johnson and Christy. The SiO₂ light line (gray) is included for reference.33

Figure 2.10 Geometry and characteristic tangential magnetic field profiles H_y for a metal slab waveguide with metal thickness d . (a) The low-energy, antisymmetric mode (A); (b) The high-energy, symmetric mode (S). The wave propagates along the positive z direction.35

Figure 2.11 Dispersion for the SiO₂-Ag-SiO₂ geometry for various Ag thicknesses (12, 20, 35, and 50 nm) using silver optical constants of Johnson and Christy. (a) Low-energy, antisymmetric mode (A); (b) High-energy, symmetric mode(S).36

Figure 2.12 Geometry and characteristic tangential magnetic field profile H_y for the semi-infinite MIM waveguide with core insulator thickness d . (a) The high-energy, antisymmetric field mode (A); (b) The low-energy, symmetric field mode (S). The waves propagate along the positive z direction.40

Figure 2.13 TM dispersion relations of MIM (Ag-SiO₂-Ag) structures for various oxide thicknesses (12, 20, 35, and 50 nm) using silver optical constants of Johnson and Christy. Dispersion for a Ag-SiO₂ interface is plotted in black as reference. (a) High-energy antisymmetric (A) mode; (b) Low-energy symmetric (S) mode.41

Figure 2.14 SPPs excitation configurations: (a) Kretschmann geometry, (b) two-layer Kretschmann geometry, (c) Otto geometry, (d) excitation with a near-field scanning optical microscopy (NSOM) probe, (e) diffraction on a grating, (f) diffraction on surface features, and (g) excitation with highly focused optical beams.43

Figure 2.15 Prism coupling and SPP dispersions at the interfaces of a thin metal film bounded with a vacuum ($\epsilon_c = 1$) and a prism ($\epsilon_{prism} = 2.25$). Also plotted are the vacuum

and prism light lines (dashed lines) and the corresponding surface plasmon frequencies (dotted lines). The dashed portion of SPP at the metal-air interface, lying to the right of the vacuum light line while inside the prism light cone, is accessible. This excited SPP localizes at the metal-air interface and leaks energy into the prism. The metal used for plots is silver with $\omega_p=11.9989 \times 10^{15} s^{-1}$ and a thickness of 30 nm.45

Figure 3.1 TM dispersion relations (A) and characteristic tangential field profiles (B) for a symmetric Ag-air-Ag planar MIM structure bounded by free space with insulator thickness $d_I=300$ nm and metal thickness $d_M=50$ nm. (B) illustrates fields at vacuum wavelengths of 400 nm (black) and 600 nm (gray). Panels (a)-(e) plot the tangential magnetic field (H_y) for the conventional metal-clad waveguide mode, and modes S_L , A_L , S_H , and A_H respectively. Panel (f) shows the tangential electric fields (E_z) of mode A_H57

Figure 3.2 Surface charge distributions associated with the four coupled SP modes in a finite planar MIM waveguide.60

Figure 3.3 MIM dispersion as a function of insulator thickness (a) and metal film thickness (b). The arrow indicates increasing thickness. (a): MIM geometry with metal thickness $d_M=50$ nm and insulator thickness $d_I=20, 50, 100$ and 200 nm (for modes S_L , A_L and S_H) and $d_I=100, 200$ and 300 nm (for mode A_H). Dispersion relations for air-Ag (50 nm)-air IMI waveguide, low energy antisymmetric modes (top two panels) and high energy symmetric modes (bottom two panels), are plotted in solid black lines as reference. (b): MIM geometry with insulator thickness $d_I=300$ nm and metal thickness $d_M=20, 35,$ and 50 nm. Dispersion relations for semi-infinite MIM waveguide, low energy symmetric modes (left two panels) and high energy antisymmetric modes (right two panels) are also plotted in solid black lines as reference.61

Figure 3.4 Wavelength-dependent propagation length and confinement factor for a MIM structure of $d_I=300$ nm and $d_M=50$ nm. It has the same waveguide structure and mode color assignment as that in Fig. 3.1.63

Figure 3.5 Propagation length L (black lines and symbols) and confinement factor Γ (gray lines and symbols) for the MIM plasmonic waveguide at a free-space wavelength of 500 nm as a function of (a) metal ((b) insulator) thickness with fixed (a) insulator thickness $d_I = 100$ nm ((b) metal thickness, $d_M = 20$ nm).64

Figure 3.6 Schematic of a radiative MIM SP wave which exponentially decays along the $+z$ axis with an exponentially growing field along the $-x$ axis. Only one side radiation in $x < 0$ is shown here.68

Figure 3.7 MIM leaky wave-front tilt θ (a) and radiation free-space coupling pattern at a free-space wavelength of 633nm (b) as a function of insulator and metal thickness (d_{IM}). In (a), the transition from purple to black in the plot curves occurs at the wavelength where the MIM waveguide modal propagation constant has equal real and imaginary values.70

Figure 3.8 TM dispersion relation (a), propagation loss (b) and confinement factor (c) for S_L mode by using dielectric constant without (dashed lines) and with (solid lines) spatial dispersion. The simulated Ag-air-Ag MIM structures in free space have the metal thickness of 20 nm and core layer thickness of 2 nm (blue lines) and 5 nm (red lines).73

Figure 4.1 Symmetric (a) and asymmetric (b) MIM ATR Kretschmann configurations.78

Figure 4.2 ATR reflectance curves at 633nm for (a) symmetric glass-Au-MgF₂-Au-glass and (b) asymmetric air-Au-MgF₂-Au-glass MIM geometries. See the text for discussion of θ_0 , θ_A , θ_B , θ_C and θ_D79

Figure 4.3 Normalized Poynting vector fields of (a) symmetric and (b) asymmetric MIM geometries when on or off resonance. The angles θ_0 , θ_A , θ_B , θ_C and θ_D are the same as those shown in Fig. 4.2.81

Figure 4.4 (a) Experimental TM reflectance for the Au-Al ₂ O ₃ -Au MIM structure. (b) The dispersion curves for the radiative SPs of sample B. (c) Radiation patterns (left to right) of the radiative SP at 720, 750 and 780nm.	83
Figure 5.1 The geometry and coordinates of the reflection of a plane wave on a planar interface between two different media.	89
Figure 5.2 (a): Geometry for enhanced reflectance using SP excitation. Thickness of gain medium is assumed to be infinite. (b): Reflectance vs angle of incidence near surface plasmon angle for several values of the gain parameter α	91
Figure 5.3 Schematic of a symmetric glass-silver-Rh6G/PMMA-silver-glass planar MIM structure. The silver and Rh6G/PMMA thickness are labeled as d_M , d_I , respectively.	92
Figure 5.4 Propagation length and confinement factor of SP modes in a symmetric glass-silver-Rh6G/PMMA-silver-glass planar MIM structure at free-space wavelength 594 nm as a function of metal (d_M) and insulator (d_I) thickness.	93
Figure 5.5 The normalized propagation constant imaginary part v.s. Rh6G/PMMA gain coefficient. The red dots label gain coefficient value where $k_z'' = 0$	95
Figure 5.6 Propagation length of S _H mode versus metal (d_M) and insulator (d_I) thickness at free-space wavelength 594 nm for a symmetric glass-silver-Rh6G/PMMA-silver-glass planar MIM structure with zero core gain (black dash lines) and core gain coefficient $\gamma = 420 \text{ cm}^{-1}$ (red solid lines).	98
Figure 5.7 Schematic of SPP excitation in an ATR geometry.	99
Figure 5.8 ATR reflectance curve at 594nm for SF ₁₁ prism-MgF ₂ -Ag-PMMA-Ag-Rh6G/PMMA geometry, sketched in Fig. 5.7, as a function of incidence angle θ with zero Rh6G gain.	100

Figure 5.9 Reflectance of the MIM structure in ATR geometry (depicted in Fig.5.7) as a function of incidence angle θ for various gain values. The gain values are given by $n''_{Rh6G/PMMA}$ the imaginary part of refractive index of Rh6G/PMMA. For the red curve labeled double gain layer, the central PMMA layer is replaced by Rh6G/PMMA.101

Figure 5.10 Normalized Poynting vector fields versus gain value.at the incidence angle of 56.1° . The gain values are given in terms of the imaginary part of refractive index of Rh6G/PMMA ($n''_{Rh6G/PMMA}$). Subplots (A) - (D) correspond to gain values of 0 , 1.0×10^{-3} , 1.5×10^{-3} and 2.0×10^{-3} , respectively. Subplot (E) corresponds to the double gain layer case with both gain values of 2.0×10^{-3}104

Figure 6.1 Road map of electromagnetic spectrum.111

Figure 6.2 Schematic diagrams of THz QC-laser waveguides for (a) SI-SP and (b) MM waveguides. n^+ indicates heavily doped semiconductor and $\text{Re}\{\epsilon\} < 0$ indicates the real part of the dielectric permittivity is less than zero.115

Figure 6.3 SI-SP waveguide simulated results for (a) waveguide loss α_w , (b) confinement factor (Γ), and (c) threshold gain (g_{th}) versus plasma doping (n_{pl}) for plasma layer thickness of 400 nm at frequencies 2.0, 3.0, 4.0, 5.0 and 7.0 THz.122

Figure 6.4 SI-SP waveguide simulated results for (a) waveguide loss (α_w), (b) confinement factor (Γ), and (c) threshold gain (g_{th}) versus plasma doping for plasma layer thickness (t_{pl}) of 200, 400, 600 and 800 nm at 4 THz.124

Figure 6.5 SI-SP waveguide simulated results for waveguide loss (α_w), confinement factor (Γ), and threshold gain (g_{th}) versus substrate thickness at 3 THz (left) and 5 THz (right). The plasma layer is 400 nm thick at plasma doping (n_{pl}) of 1.0×10^{18} , 3.0×10^{18} and $5.0 \times 10^{18} \text{ cm}^{-3}$126

Figure 6.6 Waveguide loss (α_w), confinement factor (Γ), and threshold gain (g_{th}) for MM waveguide with active region thicknesses of 5 and 10 μm at frequencies $f = 2.0, 3.0, 5.0$

and 7.0 THz. Between the top/bottom Au contacts, the active region is sandwiched between two contact layers (one is 100nm thick and another one is 400 nm thick) both doped at $5 \times 10^{18} \text{ cm}^{-3}$. The results for a SI-SP waveguide with 10 μm thick active region are included as reference. Its upper contact layer (100 nm) and bottom plasma layer (400 nm) are both doped the same as that in MM waveguide.128

Figure 6.7 Schematic for THz QCL MIM Leaky Waveguide129

Figure 6.8 Leaky wave-front tilt θ (a) for waveguides with active region thicknesses (d_{active}) of 10 and 15 μm and with plasma layer thicknesses (d_{pl}) of 400 and 800 nm; Radiation patterns at wavelength 112 μm (b) for waveguides with $d_{active} = 15 \mu\text{m}$ and $d_{pl} = 400 \text{ nm}, 800 \text{ nm}$. The plasma layer is doped at $5 \times 10^{18} \text{ cm}^{-3}$130

Figure 7.1 (a) The configuration of actuator modulator based on free-space coupling. (b) Schematic of intensity modulation of the reflected light induced by a periodically varying PZT thickness. The curves (red and green) are modeled with PZT index of 2.5, incidence angle of 30° with respect to the normal direction.139

Figure B.1 Geometry for SPPs propagation at a single planar interface between semi-infinite dielectric and metal.147

Figure C.1 Geometry of a multilayer planar waveguide150

Figure C.2 The propagating exponential components (arrow) and the field distribution profile (dash) in a multilayer waveguide outermost regions of (a) guided mode, (b) radiation mode, and (c) leaky mode. Note: Only double-sided radiation mode is shown in (b).153

Figure D.1 Newton’s method extrapolates the local derivative to find the next estimate of the root.154

LIST OF TABLES

Table 2.1 k_x and k_z for various complex waves: proper and improper waves	11
Table 2.2 Properties of forward propagating modes in a lossless planar waveguide	19
Table 2.3 Values of the LD Model Parameters	30
Table 5.1 Optimum symmetric glass-Ag-Rh6G/PMMA-Ag-glass MIM structure	94
Table 6.1 List of the parameters used for SI-SP waveguide simulation	121
Table 6.2 Optimum plasma layer doping range ($\times 10^{18} \text{ cm}^{-3}$) and respective g_{th} (cm^{-1}) ..	125

Chapter 1 Introduction

1.1 Introduction

Surface plasmon polaritons (SPPs), or surface plasmons (SPs) in short, are the transverse magnetic (TM) waves propagating along metal-dielectric interfaces with fields exponentially decaying in both media. The studies of surface electromagnetic (EM) waves started in the early 1900's. Zenneck [1] in 1907 firstly theoretically analyzed the surface wave property of the so-called "Zenneck wave" at a planar boundary between free space and a half space with a finite conductivity. Sommerfield [2] in 1909 realized the possibility of radio waves propagating around the earth by treating the upper half space as a pure dielectric and the lower one as a conductor. Fano [3] in 1941 proposed that surface EM wave resulted in the Wood's anomalies [4] in metal diffraction gratings. After that, Ritchie [5], Ferrell [6,7] and Powell [8-10] had theoretically and experimentally confirmed the existence of surface plasmons at a metal surface. SPPs were observed optically in the attenuated total reflection (ATR) experiments by Otto [11] and Kretschmann and Raether [12] in 1968. Since then SPPs have been extensively explored for several decades for their potentials in nanophotonics [13, 14], metamaterials [15] and biosensing [16-19].

The surface localization property of SPs, confining the optical mode to subwavelength scale and minimizing the optical mode size, makes plasmonic waveguides an intriguing alternative to conventional dielectric-based waveguides. Long-range SP waveguides based on thin metal films or strips (referred to as insulator-metal-insulator (IMI) waveguides) have been studied previously [20, 21], but metal-insulator-metal

(MIM) SP waveguides [22, 23], offering higher confinement factors and closer spacing to adjacent waveguides or structures [24], have been proposed for this and other potential applications [25-29]. Study also suggests that MIM subwavelength plasmonic waveguide bends and splitters have low loss over a wide frequency range [30]. Gain-induced switching in MIM plasmonic waveguides has been also proposed [31].

1.2 Outline of the Dissertation

The objective of this work is to investigate characteristics of finite planar MIM plasmonic waveguides. This document is organized as follows:

Chapter 2 outlines the requisite background theories underlying this dissertation. The concept of improper leaky wave, its role in waveguide mode expansion, and the physical origin of spectral gap when a mode changes from bound to leaky upon crossing the light line are introduced. The theoretical models and empirical data parameterization for metal dielectric constants are presented. The fundamentals of SPPs at a single metal-dielectric interface and in multilayer systems, including IMI and semi-infinite MIM waveguides, as well as SPPs optical excitation schemes are reviewed.

In Chapter 3, numerical analysis of finite planar MIM waveguides using the transfer-matrix formalism reveals both bound and leaky SP modes. The dispersion relations, propagation lengths and confinement factors for these SP modes are presented. The highest energy SP mode is revealed consisting of non-radiative (bound) and radiative (leaky) portions separated by a spectral gap. The leaky regime is further divided into two distinct regions and its wave-front tilt and radiation pattern are discussed. The spatial dispersion effects on dispersion, propagation loss and confinement factor of the lowest

energy SPP mode of MIM structures with a thin core layer at large wave vectors are examined.

In Chapter 4, the radiative MIM SPPs are investigated theoretically and experimentally. Leaky waves are probed using ATR Kretschmann configuration and using free space coupling. Both single- and double-sided leaky waves are analyzed. Free-space coupling to the antenna leaky wave is experimentally demonstrated. The leaky wave dispersion relation and its antenna mode radiation pattern are determined through both angle- and wavelength-dependent reflectance of TM polarized free space incident light.

Chapter 5 numerically analyzes realistic finite MIM plasmonic waveguides with the inclusion of dye-doped polymer. The propagation of three bound SP modes within each respective optimized MIM waveguide is analyzed numerically for a core material exhibiting optical gain. For MIM structure in ATR geometry, the reflectance and energy flux distribution at resonance conditions versus gain coefficients in adjacent dielectric medium are discussed.

Chapter 6 provides modeling of finite MIM waveguides for terahertz quantum cascade lasers. The waveguide loss, confinement factor and threshold gain are characterized. The influences of plasma layer doping, plasma layer thickness as well as substrate thickness are analyzed for the semi-insulating surface-plasmon waveguide, and the effects of active region thickness are discussed for the metal-metal waveguide. The leaky waveguide characterization is also discussed.

Chapter 7 summarizes the work presented in this dissertation and gives an outlook on future works of MIM plasmonic waveguides.

References

- [1] J. Zenneck, "On the propagation of plane electromagnetic waves along a planar conductor surface and its relationship to wireless telegraphy," *Ann Phys.* **23**, 848 (1907).
- [2] A. Sommerfeld, "On the propagation of waves in the wireless telegraphy," *Ann Phys.* **28**, 665 (1909).
- [3] U. Fano, "The theory of anomalous diffraction gratings and of quasi-stationary waves on metallic surfaces (Sommerfeld's waves)," *J. Opt. Soc. Am.* **31**, 213 (1941).
- [4] R. W. Wood, "On a remarkable case of uneven distribution of light in a diffraction grating spectrum," *Phil. Mag.* **4**, 396 (1902).
- [5] R. H. Ritchie, "Plasma losses by fast electrons in thin films," *Phys. Rev.* **106**, 874 (1957).
- [6] R. A. Ferrell, "Predicted radiation of plasma oscillations in metal films," *Phys. Rev.* **111**, 1214 (1958).
- [7] E. A. Stern, and R. A. Ferrell, "Surface plasma oscillations of a degenerate electron gas," *Phys. Rev.* **120**, 130 (1960).
- [8] C. J. Powell, J. L. Robins, and J. B. Swan, "Effects of contamination on the characteristic loss spectrum of tungsten," *Phys. Rev.* **110**, 657 (1958).
- [9] C. J. Powell, and J. B. Swan, "Origin of the characteristic electron energy losses in aluminum," *Phys. Rev.* **115**, 4 (1959).
- [10] C. J. Powell, "The origin of the characteristic electron energy losses in ten elements," *Proc. Phys. Soc. (London)* **76**, 593 (1960).
- [11] A. Otto, "Excitation of nonradiative surface plasma waves in silver by the method of frustrated total reflection," *Z. Phys.* **216**, 398 (1968).
- [12] E. Kretschmann, and H. Raether, "Radiative decay of nonradiative surface plasmons excited by light," *Z. Naturforsch. Teil, A* **23**, 2135 (1968).
- [13] W. L. Barnes, A. Dereux, and T. W. Ebbesen, "Surface plasmon subwavelength optics," *Nature* **424**, 824 (2003).

- [14] E. Ozbay, "Plasmonics: Merging photonics and electronics at nanoscale dimensions," *Science* **311**, 189 (2006).
- [15] V. M. Shalaev, "Optical negative-index metamaterials," *Nat. Photon.* **1**, 41 (2007).
- [16] K. Kneipp, Y. Wang, H. Kneipp, L. T. Perelman, I. Itzkan, R. R. Dasari, and M. S. Feld, "Single molecule detection using surface-enhanced raman scattering (SERS)," *Phys. Rev. Lett.* **78**, 1667 (1997).
- [17] S. Nie, and S. R. Emory, "Probing single molecules and single nanoparticles by surface-enhanced raman scattering," *Science* **275**, 1102 (1997).
- [18] S. Lal, S. Link, and N. J. Halas, "Nano-optics from sensing to waveguiding," *Nat. Photonics* **1**, 641 (2007).
- [19] J. N. Anker, W. P. Hall, O. Lyandres, N. C. Shah, J. Zhao, and R. P Van Duyne, "Biosensing with plasmonic nanosensors," *Nat. Mater.* **7**, 442 (2008).
- [20] T. Goto, Y. Katagiri, H. Fukuda, H. Shinojima, Y. Nakano, I. Kobayashi, and Y. Mitsuoka, "Propagation loss measurement for surface plasmon-polariton modes at metal waveguides on semiconductor substrates," *Appl. Phys. Lett.* **84**, 852 (2004).
- [21] R. Charbonneau, N. Lahoud, G. Mattiussi, and P. Berini, "Demonstration of integrated optics elements based on long-ranging surface plasmon polaritons," *Opt. Express* **13**, 977 (2005).
- [22] J. A. Dionne, L. A. Sweatlock, and H. A. Atwater, "Plasmon slot waveguides: Towards chip-scale propagation with subwavelength-scale localization," *Phys. Rev. B* **73**, 035407 (2006).
- [23] J. Chen, G. A. Smolyakov, S. R. J. Brueck, and K. J. Malloy, "Surface plasmon modes of finite, planar, metal-insulator-metal plasmonic waveguides," *Opt. Express* **16**, 14902 (2008).
- [24] R. Zia, M. D. Selker, P. B. Catrysse, and M. L. Brongersma, "Geometries and materials for subwavelength surface plasmon modes," *J. Opt. Soc. Am. A.* **21**, 2442 (2004).
- [25] P. Tournois, and V. Laude, "Negative group velocities in metal-film optical waveguides," *Opt. Commun.* **137**, 41 (1997).
- [26] Y. Wang, "Wavelength selection with coupled surface plasmon waves," *Appl. Phys. Lett.* **82**, 4385 (2003).

- [27] H. Shin, M. F. Yanik, S. Fan, R. Zia, and M. L. Brongersma, "Omnidirectional resonance in a metal–dielectric–metal geometry," *Appl. Phys. Lett.* **84**, 4421 (2004).
- [28] John S. Q. Liu, and Mark L. Brongersma, "Omnidirectional light emission via surface plasmon polaritons," *Appl. Phys. Lett.* **90**, 091116 (2007).
- [29] J. Feng, T. Okamoto, J. Simonen, and S. Kawata, "Color-tunable electroluminescence from white organic light-emitting devices through coupling surface plasmons," *Appl. Phys. Lett.* **90**, 081106 (2007).
- [30] G. Veronis, and S. Fan, "Bends and splitters in metal–dielectric–metal subwavelength plasmonic waveguides," *Appl. Phys. Lett.* **87**, 131102 (2005).
- [31] Z. Yu, G. Veronis, S. Fan and, M. L. Brongersma, "Gain-induced switching in metal-dielectric-metal plasmonic waveguides," *Appl. Phys. Lett.* **92**, 041117 (2008).

Chapter 2 Theoretical Background

2.1 Introduction

This chapter presents a brief review of the requisite background theories underlying this dissertation.

In chapter 2.2, the various types and corresponding mathematic representations of electromagnetic complex waves are presented. The improper waves with exponential growing field profiles are pointed out. In chapter 2.3.1, three types of waveguide mode, i.e. bound, radiation and leaky modes, are reviewed. The role of discrete improper leaky mode, characterized by exponential growing field profile in one or both outermost media, in modal expansion is discussed. In chapter 2.3.2, as an example, the evolution of dispersion behavior for TM-even mode of a symmetric slab waveguide clearly shows the proper and improper mode branches and the physical origin of spectral gap separating the physical bound and leaky modes. In chapter 2.4, the theoretical models and empirical data parameterization for metal dielectric constants are presented. The characteristic properties of SPPs sustained at a single metal-dielectric interface and in multilayer systems, including IMI and semi-infinite MIM waveguides, as well as SPPs optical excitation schemes are reviewed in chapter 2.5.

2.2 Electromagnetic Complex Waves

There are various EM wave types such as surface wave, leaky wave and other guided waves. It is very important to recognize these various types and their

corresponding mathematical representations. An EM wave in general form is usually called complex waves. As presented in Fig. 2.1, the yz -plane is the interface plane between two semi-infinite media and a plane wave $\mathbf{E}(x, z, t)$ propagating in the upper half-space ($x > 0$), which is filled with a homogeneous lossless medium with a relative permittivity ϵ_r , is examined. The wave is assumed containing a time dependence of the form $\exp(-i\omega t)$, where ω is the radian frequency and t is the time variable. This time dependence convention is used throughout the whole dissertation.

The wave satisfies a wave equation (see Appendix A: equation (A.6a)) and leads to a two-dimensional Helmholtz equation,

$$(\nabla^2 + k^2)\mathbf{E}(x, z) = \left(\frac{\partial^2}{\partial x^2} + \frac{\partial^2}{\partial z^2} + k^2 \right) \mathbf{E}(x, z) = 0 \quad (2.1)$$

where $k = \sqrt{\epsilon_r}k_0$, k_0 is the vacuum wave vector. The above equation has solution of the form $\mathbf{E}(x, z) = \mathbf{E}_0 e^{i(k_x x + k_z z)}$, where \mathbf{E}_0 is a constant vector transverse to the propagation vector \mathbf{k} , $\mathbf{k} = k_x \hat{x} + k_z \hat{z} = k \hat{k}$, with

$$k_x^2 + k_z^2 = k^2 \quad (2.2)$$

Rewrite (2.2) as $k_x = \pm \sqrt{k^2 - k_z^2}$, this indicates that the plane wave function has branch points of order 2 at $\pm k$ in the complex k_z -plane. The complex k_z -plane is divided into two Riemann sheets: a *proper* sheet (or top sheet) on which $\text{Im}\{k_x\} > 0$, and an *improper* sheet (or bottom sheet) on which $\text{Im}\{k_x\} < 0$. These two sheets are connected on the curve $\text{Im}\{k_x\} = 0$. In the proper Riemann sheet, $\mathbf{E}(x, z)$ represents a physical proper wave with exponentially decaying amplitude at the $x > 0$ half-space. In contrast, in the improper Riemann sheet, $\mathbf{E}(x, z)$ is an improper wave with exponentially growing

amplitude at the $x > 0$ half-space. In many problems it is convenient to use branch cuts that separate a proper wave from an improper wave.

Without losing generality, we write $k_x = k'_x + ik''_x$, $k_z = k'_z + ik''_z$, $\mathbf{r} = x\hat{x} + z\hat{z}$, $\mathbf{k}' = k'_x\hat{x} + k'_z\hat{z}$, and $\mathbf{k}'' = k''_x\hat{x} + k''_z\hat{z}$. Here and after, single ['] and double ['] primes stand for real and imaginary parts of complex numbers, and the italic bold letter denotes a vector. Then the plane wave can be re-written as

$$\mathbf{E}(x, z) = \mathbf{E}_0 \exp[i\mathbf{k}' \cdot \mathbf{r}] \exp[-\mathbf{k}'' \cdot \mathbf{r}] \quad (2.3)$$

The phase and attenuation of the plane wave are governed respectively by the real part (\mathbf{k}') and imaginary part (\mathbf{k}'') of the propagation vector. From (2.2a), we get

$$k_x'^2 + k_z'^2 - (k_x''^2 + k_z''^2) = k^2 \quad (2.4a)$$

$$k_x'k_x'' + k_z'k_z'' = \mathbf{k}' \cdot \mathbf{k}'' = 0 \quad (2.4b)$$

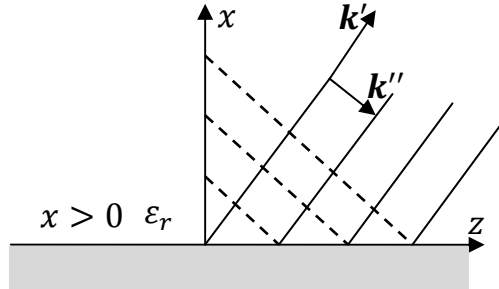


Fig. 2.1 Constant amplitude (solid lines) and constant phase (dash lines) surfaces of a plane wave propagating in the upper half xz -plane.

According to (2.3), the constant-phase surfaces and constant-amplitude surfaces are given respectively by

$$\mathbf{k}' \cdot \mathbf{r} = \text{Constant A} \quad (2.5a)$$

$$\mathbf{k}'' \cdot \mathbf{r} = \text{Constant B} \quad (2.5b)$$

Equation (2.5) indicates that the constant-phase surfaces (dash lines in Fig. (2.1)) are perpendicular to \mathbf{k}' and the constant-amplitude surfaces (solid lines in Fig. (2.1)) are perpendicular to \mathbf{k}'' . Given $\mathbf{k}' \cdot \mathbf{k}'' = 0$ in (2.4b), the constant-phase surfaces and the constant-amplitude surfaces are perpendicular to each other.

In the complex k_z plane, a curve defined by equation $k_z = k + R\exp(i\theta)$ with $R < k$ is considered. The k_z curve and corresponding k_x curve in the complex k_x -plane are shown in Fig. 2.2. Several k_z points (A through H), determined by various values of θ and lying on the top (proper) and bottom (improper) sheets of the complex k_z -plane, are chosen. The solid (dash) circle lies on the top (bottom) sheet. The circle on the bottom sheet is shown larger for clarity [1]. Points B-D and F-H lie respectively on the top and bottom sheet, and points A and E lie on the branch cut. Points B, C and D represent proper waves whereas points F, G and H represent improper waves. A variety of wave types, identified by various k_x and k_z values, and their corresponding terminologies are summarized in Table 2.1 [1]. The real and imaginary parts of these complex wave propagation vectors ($\mathbf{k} = \mathbf{k}' + i\mathbf{k}''$) in space are shown in Fig. 2.3 [1, 2]. More details about these wave types can be found in Ref. [2].

Among the wave types list in Table 2.1, only the forward propagating waves are considered here and after. The trapped surface wave, Zenneck wave and forward leaky wave will appear in the rest part of this dissertation. Surface waves are waves that propagate along the interface between two different mediums without radiation. Trapped surface waves are surface waves with exponentially decaying field profiles in the transverse direction. The Zenneck wave is a TM polarized surface wave exists at the interface between a dielectric and a media with a finite conductivity. The amplitude of

this wave decays exponentially in the directions both parallel and perpendicular to the boundary (with differing decay constants).

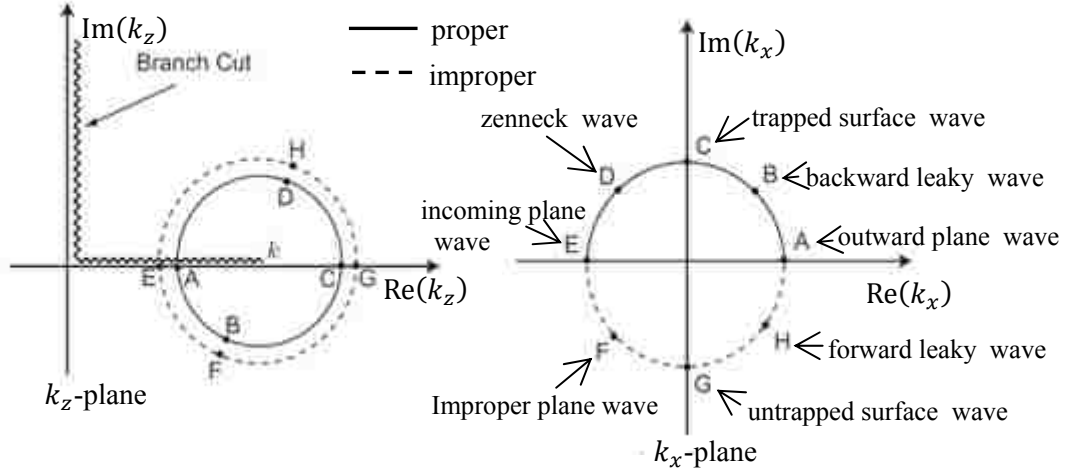


Fig. 2.2 Complex waves in the complex k_x and k_z planes [1].

Table 2.1 k_x and k_z for various complex waves: proper and improper waves [1]

Point	k'_z	k''_z	k'_x	k''_x	Complex wave
A	$< k$	0	> 0	0	Outward plane wave
B	> 0	< 0	> 0	> 0	Backward leaky wave
C	$> k$	0	0	> 0	Trapped surface wave
D	> 0	> 0	< 0	> 0	Zenneck wave
E	$< k$	0	< 0	0	Incoming plane wave
F	> 0	< 0	< 0	> 0	Improper plane wave
G	$> k$	0	0	< 0	Untrapped surface wave
H	> 0	> 0	> 0	< 0	Forward leaky wave

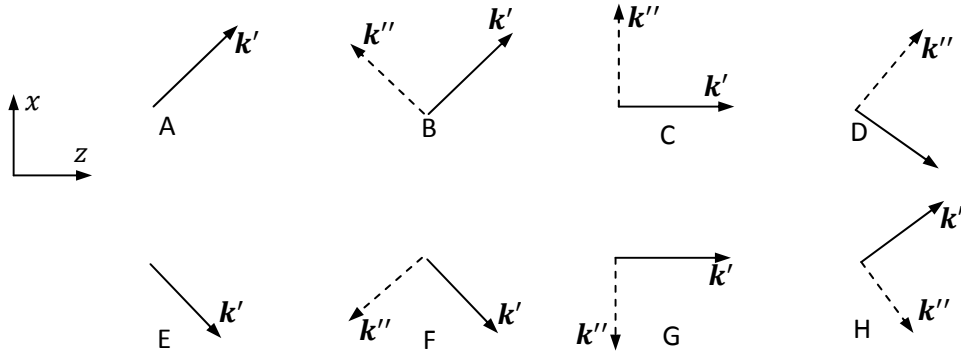


Fig. 2.3 The real and imaginary parts of the complex wave propagation vector in the upper half xz -plane [1, 2]. The yz -plane is the interface plane.

2.3 Waveguide Theory

Determination of modes of one-dimensional (1-D) multilayer planar waveguide plays a crucial role in modeling of photonic devices. The waveguide modes can be classified into three categories: guided (bound) modes, radiation modes and leaky modes. It is shown in this section that the leaky modes, with forward leaky wave (characterized by point F in Table 2.1 and Fig. 2.3, possessing exponentially increasing *improper* field profiles away from the waveguide structure) in one or both of the bounding media, are mathematically valid but “improper” solutions of the same eigenvalue problem describing the guided modes, with trapped surface waves (characterized by point C in Table 2.1 and Fig. 2.3, possessing exponentially decaying *proper* field profiles away from the waveguide structure) in both outermost media. The role of improper leaky modes in modal expansion is also discussed. The evolution of dispersion behavior for the TM-even mode of a symmetric slab waveguide is presented in Chapter 2.3.2 as an example to show how the character of the eigenmode changes between *proper* and

improper and the existence of spectral gap when a mode changes from physical *proper* bound to physical *improper* leaky mode upon crossing the light line.

2.3.1 Waveguide Eigenmode

Let's consider an asymmetric planar slab waveguide. The waveguide structure and the coordinate system are depicted in Fig. 2.5. It consists of a dielectric layer with refractive index n_0 sandwiched between two semi-infinite open media with refractive indexes n_c and n_s , which are referred as the upper (cover) and lower (substrate) regions, respectively. All materials are assumed to be homogeneous, isotropic and lossless. Their refractive indices satisfy the inequalities $n_0 > n_s > n_c$.

Throughout the rest of this dissertation, only the forward-propagating (along the positive- z direction) modes will be considered. Thus the mode fields vary longitudinally as $\exp[-ik_z z]$, where k_z is the longitudinal propagation constant. The transverse complex modal amplitude $\varphi(x)$ satisfies 1-D Helmholtz equation (See equation (C.3)) and has solution of the form $\varphi(x) = A\exp[ik_x x] + B\exp[-ik_x x]$, where A and B are constants determined by the boundary conditions, the transverse propagation constants k_x are given by $k_{xj} = \sqrt{(n_j k_0)^2 - k_z^2}$, $j = 1, 2, 3$. In principle, planar structures with layer numbers larger than three can be treated in the same way.

The most popular method for finding the modes of a planar waveguide is the thin-film transfer matrix method [3], which is described in Appendix C. This method provides implicit waveguide eigenvalue equations, also called dispersion equations, formulated by letting the elements of the transfer matrix T (See appendix C: equation (C.7)), say T_{11} ,

equal to zero. The zeros of this dispersion equation correspond to the mode propagation constant k_z . Then the effective index n_{eff} , also called modal index, is defined via $n_{eff} = k_z/k_0$.

The waveguide modes can be classified into three categories: guided (bound) modes, radiation modes and leaky modes, which are expressed in terms of the closed, continuum and improper expansions, respectively [4]. The locations of the guided modes, radiation modes and leaky modes in the complex longitudinal propagation constant plane are shown schematically in Fig. 2.4. The modal field profiles and schematic ray pictures of the four mode types found in the continuum modal expansion basis are plotted in Fig. 2.5.

(i) Guided (Bound) Modes

For guided, or bound modes, the discrete values of k_z , labeled by “*” in Fig.2.4, are determined from an eigenvalue equation. This equation is a consistency condition, or transverse resonance condition derived from the source-free Maxwell equations, subject to the requirements that the mode fields (i) go to zero at infinity, and (ii) satisfy boundary conditions at the layer interfaces. Among all discrete eigenvalues, only the values that correspond to proper waves are guided modes. The proper wave is characterized by exponentially decaying field amplitude and is therefore square integrable. All other solutions that associate with field amplitudes diverging at infinity are not included in this category.

For guided modes, the bounding media, i.e. the cover and the substrate, have only outgoing field components with amplitudes exponentially decaying away from the core/cladding interfaces, as that shown in Fig. C.1(a) in Appendix C. The guided modes

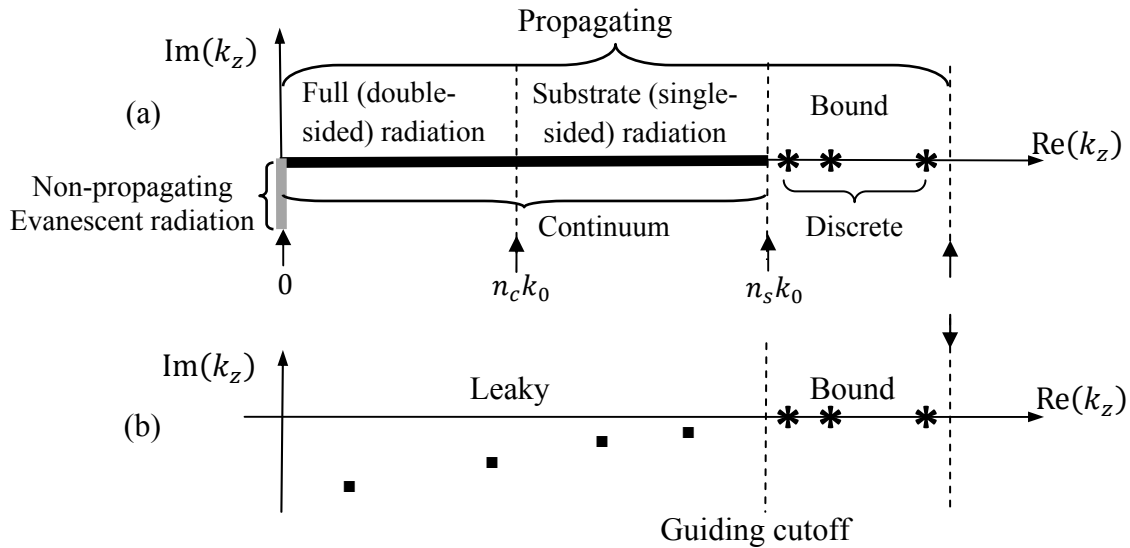


Fig. 2.4 Schematic representation of eigenvalues of the (a) continuum, and (b) improper expansion in the complex longitudinal propagation constant k_z -plane. *'s, discrete bound modes; ■'s, discrete leaky modes; bold solid black and gray lines, continuum radiation modes.

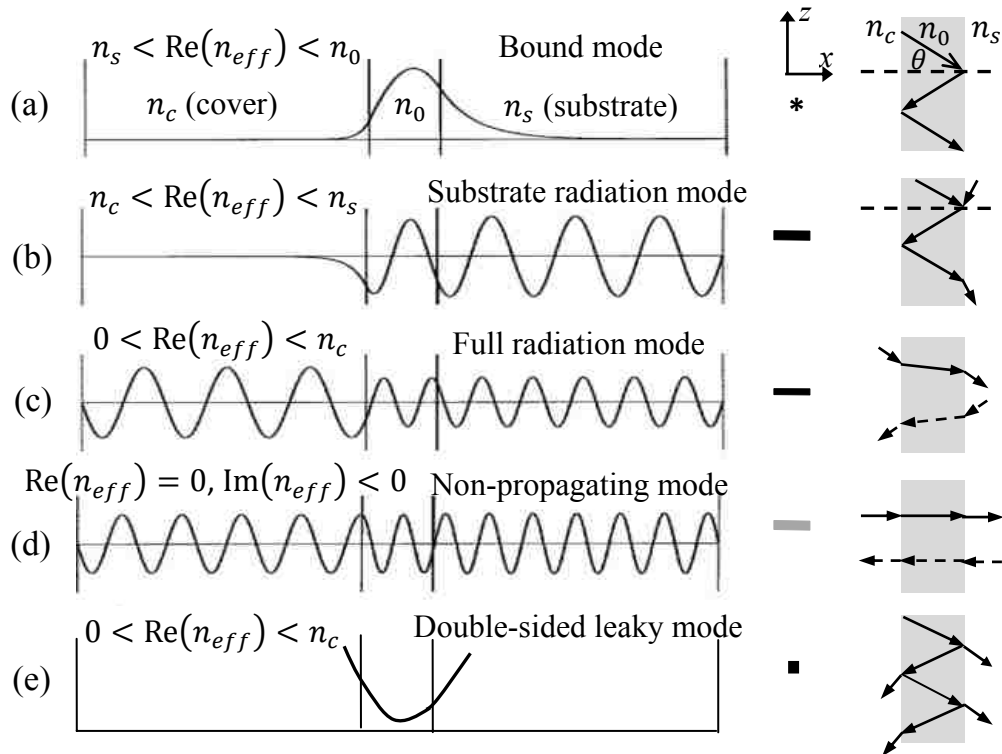


Fig. 2.5 Field profiles (left) and ray pictures (right) of the four types of mode in the continuum modal basis (panels (a)-(d)) and double-sided leaky mode (panel (e)).

posses trapped surface waves (characterized by point C in Table 2.1 and Fig. 2.3) in both outermost media. In ray picture, the bound mode energy is confined inside the core layer by total internal reflection (TIR) principle (See Fig. 2.5(a)) and flows along the guiding direction, which we have taken as the $+z$ direction. For the current lossless dielectric system, k_z is real and satisfies the condition $n_0 k_0 > k_z > n_s k_0$, and no power is lost from the waveguide. However, in a general lossy system, k_z is complex and the field amplitudes decay exponentially along the propagation direction.

(ii) Radiation Modes

Beyond the cutoff condition, values of $\text{Re}(k_z)$ smaller than $n_s k_0$ correspond to the continuum non-bound radiation modes, which are labeled by bold black and gray lines in Fig. 2.4(a). When the condition $n_c k_0 < \text{Re}(k_z) < n_s k_0$ holds, TIR no longer occurs (as in the case of bound modes) at the core/substrate interface. Both the inward- and outward-traveling field components in the substrate region are required to form standing wave to assure that there is no power flow along the lateral direction since the modes propagation constants are real. These single-sided radiation modes are called substrate radiation modes (or substrate modes in short) exhibiting standing sinusoids in the substrate region and exponentially decaying fields in the cover region (See Fig 2.5(b)). Similarly, the double-sided radiation modes, called full radiation modes, satisfying the condition $0 < \text{Re}(k_z) < n_c k_0$, exhibit standing sinusoids in both outermost regions (See Fig. 2.5(c) and Fig. C.1(b) in Appendix C). With these additional inward-going components in at least one of the bounding media, the number of unknown variables is larger than that of boundary conditions, therefore, no eigenvalue equation can be established and a continuum of propagation constants can be chosen (See Fig. 2.4(a))

bold black and gray solid lines). The substrate and full radiation modes in ray picture are depicted respectively in the right panels of Fig. 2.5(b) and (c), where the rays, coming from the regions outside the core, are partially reflected and partially pass through the waveguide core.

In the case that $\text{Re}(k_z) = 0$ and $\text{Im}(k_z) < 0$, the modes are associated with longitudinal exponentially decaying fields. Therefore, these special radiation modes are called non-propagating or evanescent modes [5] (labeled by the bold gray solid line in Fig. 2.4(a)). They also exhibit standing waves in both outermost regions and are represented with ray direction perpendicular to the waveguide material-interface planes See Fig. 2.5(d)).

The discrete guided and continuum radiation modes form a complete orthogonal modal basis of planar waveguides, which is capable of expressing any field, either bound or non-bound, in an open waveguide structure [6]. In spite of the completeness and exactness of this modal basis, the modal expansion with the inclusion of continuum radiation modes is very complicated because a large number of sampled radiation modes are needed owing to their continuous spectrum.

(iii) Leaky Modes

The continuum radiation modes occur beyond cutoff. Although they satisfy the substrate-to-cover transfer equations (See appendix C: Equation (C.7)), they are not solutions of the eigenvalue equation. However, in addition to the discrete real-valued proper bound mode solutions, discrete complex solutions (denoted by “■” in Fig. 2.4(b)) of the eigenvalue equation can be found below cutoff if assuming the substrate and/or cover layers only have outward-traveling wave with exponentially growing field profiles

(See Fig. C.1(c) in Appendix C). These complex solutions are termed as improper leaky modes [6-10]. The improper leaky modes have forward leaky wave (characterized by point F in Table 2.1 and Fig. 2.3) in one or both of the bounding media. The leaky modes on slab waveguides are caused by frustrated total internal reflection. (See Fig. 2.5(e) for double-sided leaky modes).

The discrete leaky modes along with the discrete bound modes do not form a complete basis. The inclusion of leaky modes in modal expansion encounters the power normalization and modal orthogonality problems because the leaky modes unbounded field shapes make them not square integrable in the transverse plane. In spite of these mathematical difficulties, extensive research on leaky modes has been conducted [11-17]. On the other hand, the usage of leak modes in modal expansion is attractive because, in many applications, a summation of discrete leaky modes can be used to replace the contribution from the continuous spectrum of the radiation modes [6, 17-20]. In addition, in some leaky waveguides, the mode shape of the leaky modes resembles the actual waveguide field distribution within a limited range, especially within the waveguide region [18, 21]. Furthermore, the real part of the complex propagation constants of a leaky mode can replace that of a continuous spectrum of radiation modes in the sense of modal expansion [17], and its imaginary part represents accurately the radiative decay of power temporarily confined to the guide [22]. We will further discuss the leaky modes of multilayer planar open waveguides in Chapter 2.3.2.

In general multilayer planar open waveguides, the propagation constant k_z is real or complex depending on the type of solution of the eigenvalue equation and whether the waveguide material system is lossless or lossy. The refractive indexes of the substrate (S)

and the cover (C) are labeled as n_s and n_c , respectively. Without losing generality, we assume that $n_s \geq n_c$. The transverse propagation constants in the S and C regions are labeled as k_s and k_c , respectively. To summarize: (i) for bound modes ($\text{Re}(n_{eff}) > n_s$), k_z and thus n_{eff} are discrete real in the waveguide composed of lossless materials and discrete complex in the lossy material case; (ii) for radiation modes ($\text{Re}(n_{eff}) < n_s$), k_z and n_{eff} are always continuum real (or continuum pure imaginary for the evanescent radiation modes); (iii) for leaky waves ($\text{Re}(n_{eff}) < n_s$), k_z and n_{eff} are always discrete complex. The properties of forward propagating modes in a lossless multilayer planar waveguide are summarized in Table 2.2.

Table 2.2 Properties of forward propagating modes in a lossless planar waveguide.

Mode		n_{eff}	$k_{x(c,s)}$	Field exponential components in the S and C regions	Field transverse distribution $\varphi(x)$ in the S and C regions	Forward propagating field longitudinal distribution $\varphi(z)$
Discrete guided		real $n_s < \text{Re}(n_{eff})$	imaginary	outward-going	exponential decaying (proper)	sinusoid
Continuum Radiation	Substrate radiation	real $n_c < \text{Re}(n_{eff}) < n_s$	S: real C: imaginary	S: inward- and outward-going C: outward-going	S: sinusoid C: exponential decaying (proper)	sinusoid
	Full radiation	real $0 < \text{Re}(n_{eff}) < n_c$	real	inward- and outward-going	sinusoid	sinusoid
	Evanescent	imaginary $\text{Re}(n_{eff}) = 0$ $\text{Im}(n_{eff}) < 0$	real	inward- and outward-going	sinusoid	exponential decaying
Discrete leaky		complex $0 < \text{Re}(n_{eff}) < n_s$ $\text{Im}(n_{eff}) < 0$	complex	outward-going	exponential growing (improper)	sinusoid with exponential decaying envelope

2.3.2 Dispersions of Lossless Dielectric Slab Waveguide

As discussed in previous section, both the discrete proper bound and improper leaky solutions are obtained from the same waveguide eigenvalue function. The dispersion behaviors of the waveguide proper and improper modes are examined in this section. The dispersion relations for TM-even modes of a symmetric slab waveguide are presented as an example.

Before analyzing the symmetric slab waveguide, some general dispersion properties of the longitudinal homogeneous waveguide are presented following the notation given in Ref. [23]. Let's consider a waveguide structure which is invariant along the waveguiding direction $+z$ axis. We write the waveguide dispersion equation in general form as

$$H(k_z, \omega) = 0 \quad (2.6)$$

where H is a smooth analytic function of the two complex variables (k_z, ω) , k_z is the modal propagation constant and ω is the radian frequency. The solutions of (2.6) correspond to discrete mode dispersion functions $k_{zm}(\omega)$, $m = 0, 1, 2, \dots$.

For any longitudinal homogeneous waveguides composed of reciprocal media, the following condition is satisfied:

$$H(-k_z, \omega) = 0 \quad (2.7)$$

Further, for lossless media and $\omega = \text{Re}\{\omega\}$ or $\omega = \text{Im}\{\omega\}$, complex roots occur in conjugate pairs for multilayer slab waveguide [24], which is mathematically expressed as

$$H(\pm k_z, \omega) = H(\pm k_z^*, \omega) = 0 \quad (2.8)$$

where $\pm k_z^*$ are complex conjugates of $\pm k_z$. The conditions defined in (2.7) and (2.8) hold for our considered problems.

Assuming at a frequency point $= \omega_f$, the branches (k_z, k_z^*) meet in the complex k_z -plane. This represents that the two first-order zeros of (2.6) coalesce to form a second-order zero of (2.6). It leads to

$$H(k_{zf}, \omega_f) = H'(k_{zf}, \omega_f) = 0 \quad (2.9)$$

The frequency point ω_f determined from (2.9) can be guaranteed to be a branch point to separate the conjugated mode pair (k_z, k_z^*) if it also satisfies the following nonzero condition

$$\delta = H'_\omega(k_{zf}, \omega_f) H''_{k_z k_z}(k_{zf}, \omega_f) \neq 0 \quad (2.10)$$

The frequency point defined by (2.9) and (2.10) is a first-order branch point for the conjugated mode pair (k_z, k_z^*) and denoted as $\omega_f^{(1)}$. The first-order branch point means that one complete rotation about $\omega_f^{(1)}$ results in an interchange of mode in the conjugate pair [25]. The equations (2.9) and (2.10), which define the branch point ω_f in the ω plane, are also used as the definition of the critical fold (turning) point in the (k_z, ω) plane [26, 27]. The occurrence of fold (turning) point is associated with the transition from a pair of real (proper-improper or improper-improper) modes to a complex-conjugate improper mode pair in the “spectral gap” region [28]. It should be noted that in the event of material loss, complex conjugate solutions no longer exist, but two complex modes (those which become conjugate modes when loss is removed) still coalesce at a complex fold point, given by (2.9) and (2.10) [29]. These above-mentioned basic dispersion properties of the longitudinal homogeneous waveguide will be used in the following simple case, a symmetric lossless dielectric slab waveguide.

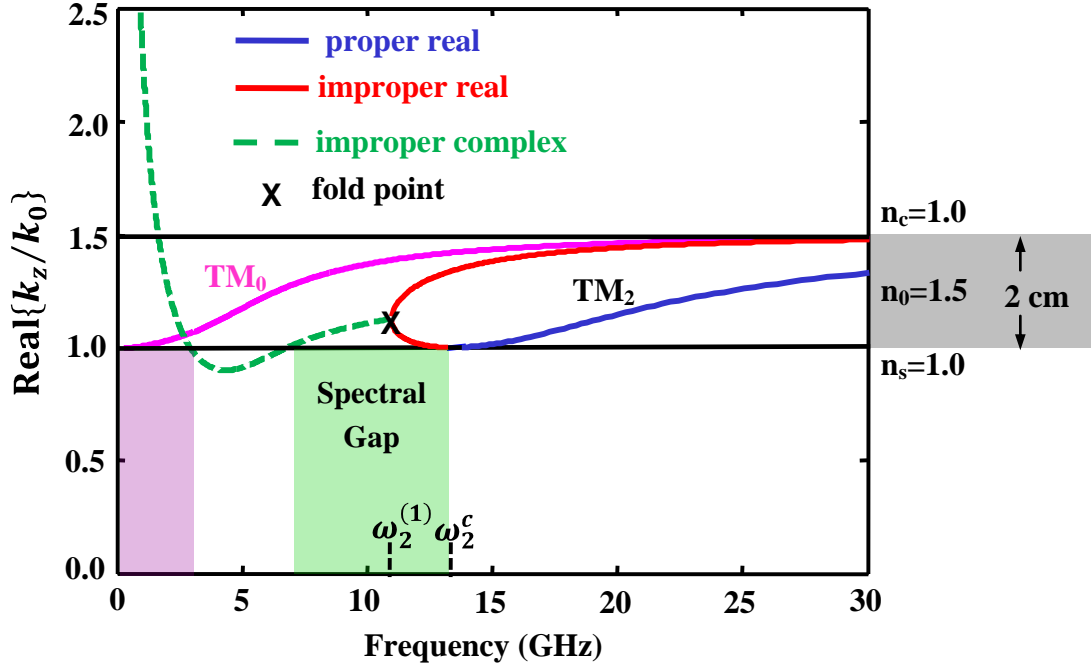


Fig. 2.6 Dispersion behaviors for the first two TM-even modes of a symmetric slab waveguide [23]. For the TM_2 mode, the proper real mode and the improper real mode are respectively highlighted by blue and red lines. The waveguide consists of a 2 cm thick dielectric layer with refractive index of $n_0 = 1.5$ sandwiched between two semi-infinite open media with refractive indexes of $n_c = n_s = 1.0$. The imaginary propagation constant is not shown.

The waveguide structure parameters and its TM modal variation with real frequency are depicted in Fig. 2.6 [23]. The transverse propagation constant along the x axis is given by $k_x = \sqrt{k_z^2 - n_1 \omega/c}$, where c is the light velocity in free space. Therefore the branch points of order 2 occur in the complex k_z -plane at $k_z = \pm n_1 \omega/c$. The points $\omega_m^{(1)}$ and ω_m^c are special points for the m th mode. ω_m^c is the cutoff frequency. Below ω_m^c , the mode pair both reside on the improper k_z -plane Riemann sheet, while above ω_m^c , one mode of the mode pair goes above cutoff and changes from the improper to the proper k_z -plane Riemann sheet. The point $\omega_m^{(1)}$ is the first-order branch point

where the conjugate branches (k_{zm}, k_{zm}^*) join together. It is also called the leaky-wave cutoff frequency, below which one mode of the conjugate (k_{zm}, k_{zm}^*) pair is the traditional below-cutoff leaky mode. As frequency is increased from $\omega = 0$ along the real frequency axis, the mode pair (k_{zm}, k_{zm}^*) for $m > 0$ follow a trajectory maintaining conjugate symmetry (the imaginary part of (k_{zm}, k_{zm}^*) not shown in Fig. 2.6) until meeting on the real k_z axis (which is a second-order root of (2.6)) at the fold point $\omega_m^{(1)}$. Between $\omega_m^{(1)}$ and ω_m^c , the modes separate and move in different directions along the real k_z axis. One mode, moving away from the origin, remains on the improper k_z -plane Riemann sheet throughout real frequencies larger than $\omega_m^{(1)}$, whereas the other mode, moving initially toward the origin, passes through the k_z -plane branch point $k_z = \pm n_1 \omega/c$ at $\omega = \omega_m^c$ onto the proper k_z Riemann sheet, becoming an ordinary, proper, surface-wave mode. More detail descriptions about Fig. 2.6 can be found in Ref. [23].

Now let's focus on the dispersion curves of the TM_2 mode. For this mode, the color-highlighted regions have no physical meaning since here, the real part of the effective index of the leaky mode (improper solutions) are larger than the index of outmost region. Therefore, the unphysical green high-lighted region is labeled as a “spectral gap” separating the physical bound (proper real) and leaky (improper complex) modes. There exists a fold point (labeled by ‘x’ in Fig. 2.6) in the “spectral gap” region where several dispersion curves join together. As mentioned above, the complex-valued modes occur in conjugate pairs. This fold point is associated with the transition from a real improper–improper mode pair to a complex-conjugate improper mode pair.

2.4 Dielectric Function of Metals

The dielectric constant, also called permittivity, characterizes the macroscopic response of a homogeneous material to applied electric fields. In this section, we will first briefly review the classical theoretical Lorentz-Drude (LD) model for calculating the frequency dependent complex dielectric constants of metals. In this model, the electrons are modeled as classical damped dipole oscillators. Then the parameterization of the optical constants of silver by LD model fit to empirical data will be present.

2.4.1 Lorentz Model

The classical Lorentz dipole oscillator model [30] is used to describe how the bound electrons within the atoms interact with an external EM wave at frequency ω . The oscillating electric field of the EM wave exerts forces on the electrons and nucleus and drives them into harmonic motion. If ω coincides with one of the natural resonant frequencies of the atom, the resonance phenomenon occurs. The atoms can therefore absorb energy from the external wave and the medium exhibits absorption. Oppositely, if ω does not coincide with any natural resonant frequencies, the atoms will not show absorption and the medium will be optically transparent.

Let's consider the interaction between an EM wave and an atom with a single natural resonant frequency ω_0 . The damping factor will be included owing to the fact that the oscillating dipoles can lose their energy by various collisional processes (such as electron-electron interaction, electron-phonon interaction, and etc.). The damping effect is modeled as a frictional force to impede the motion.

The time dependence of the electric field is given by $E(t) = E_0 e^{-i\omega t}$, and the electron displacement is denoted as x . Various forces acting on the oscillator are written as:

$$\text{Driving force: } -eE(t) = -eE_0 e^{-i\omega t}$$

$$\text{Spring (restoring) force: } -K_s x$$

$$\text{Damping force: } -\gamma v = -\gamma dx/dt$$

where e is the magnitude of the electric charge of the electron, γ is the damping (or relaxation) rate, and K_s is the spring constant satisfying the condition $\omega_0 = \sqrt{K_s/m_e}$, m_e is the electron mass.

Following the Newton's second law, the motion equation is given as

$$m_e \frac{d^2 x}{dt^2} + m_e \gamma \frac{dx}{dt} + m_e \omega_0^2 x = -eE_0 e^{-i\omega t} \quad (2.11)$$

It is obviously that (2.11) has solutions of the following form

$$x(t) = A e^{-i\omega t} \quad (2.12)$$

where A is undetermined constant. Substituting (2.12) into (2.11), we get

$$A = -\frac{eE_0}{m_e} \frac{1}{\omega_0^2 - \omega^2 - i\gamma\omega} \quad (2.13)$$

The displacement of the electrons from their equilibrium position results in a time varying dipole moment $p(t) = -ex(t)$. The resonant macroscopic polarization (dipole moment per unit volume) of the medium is given by

$$P_{\text{resonant}} = NP = -Nex = \frac{Ne^2}{m_e} \frac{1}{\omega_0^2 - \omega^2 - i\gamma\omega} E \quad (2.14)$$

where N is the electron density. The electric displacement \mathbf{D} is related to the electric field and polarization through (See appendix A: equation (A.2a))

$$\mathbf{D} = \varepsilon_0 \mathbf{E} + \mathbf{P} \quad (2.15)$$

For isotropic material, the relative permittivity is defined by

$$\mathbf{D} = \varepsilon_0 \varepsilon_r \mathbf{E} \quad (2.16)$$

We combine (2.14), (2.15) and (2.16) to obtain:

$$\begin{aligned} \varepsilon_r(\omega) &= 1 + \frac{Ne^2}{m_e} \frac{1}{\omega_0^2 - \omega^2 - i\gamma\omega} = 1 + \frac{\omega_p^2}{\omega_0^2 - \omega^2 - i\gamma\omega} \\ &= \varepsilon_r' + i\varepsilon_r'' \end{aligned} \quad (2.17)$$

where $\omega_p = \sqrt{Ne^2/m_e\varepsilon_0}$ is the plasma frequency, and the real and imaginary parts of the dielectric constant are given as

$$\begin{aligned} \varepsilon_r' &= 1 + \frac{\omega_p^2(\omega_0^2 - \omega^2)}{(\omega_0^2 - \omega^2)^2 + \gamma^2\omega^2} \\ \varepsilon_r'' &= \frac{\omega_p^2\gamma\omega}{(\omega_0^2 - \omega^2)^2 + \gamma^2\omega^2} \end{aligned}$$

The complex refractive index is obtained as $n = \sqrt{\varepsilon_r} = n' + in''$, where $n'^2 - n''^2 = \varepsilon_r'$ and $2n'n'' = \varepsilon_r''$.

For system with multiple oscillators, the Lorentz model is expressed as

$$\varepsilon_r(\omega) = 1 + \sum_{j=1}^m \frac{f_j \omega_{pj}^2}{\omega_j^2 - \omega^2 - i\gamma_j\omega}$$

where f_j is the oscillator strength.

2.4.2 Drude Model

Metals contain significant numbers of free electrons. These electrons are not bound to any atoms and can move freely without experiencing any restoring force. This

implies that the spring constant is zero, and hence the natural resonant frequency ω_0 equals zero. Therefore we get the relative complex permittivity of metals

$$\varepsilon_r = 1 - \frac{\omega_p^2}{\omega^2 + i\gamma\omega} = \varepsilon_r' + i\varepsilon_r'' \quad (2.18)$$

with

$$\varepsilon_r' = 1 - \frac{\omega_p^2}{\omega^2 + \gamma^2}$$

$$\varepsilon_r'' = \frac{\omega_p^2\gamma}{\omega(\omega^2 + \gamma^2)}$$

This is called free electron Drude model. Typically, $\omega_p > \gamma$. This dissertation work is limited to frequencies below ω_p , where metals retain their metallic character ($\varepsilon_r' < 0$).

For large frequencies close to ω_p , $\omega \gg \gamma$, leading to negligible damping. Thus ε_r is predominant real and (2.18) simplifies to

$$\varepsilon_r(\omega) = 1 - \left(\frac{\omega_p}{\omega}\right)^2, \quad (2.19)$$

which defines the dielectric function of an undamped free electron plasma. At frequencies $\omega < \omega_p$, the relative permittivity of metal exhibits negative value.

Free electron Drude model, given in (2.19), is commonly quoted as an adequate optical dielectric function of metals. However, a more accurate optical characterization of metals throughout the electromagnetic spectrum requires using metal empirical optical constants.

2.4.3 Metal Empirical Optical Constants

Silver and gold are two most used metals in SP applications. The widely quoted empirical optical constants of these two metals are taken from the data sets of Johnson and Christy [31] and Palik [32]. In addition, the experimental data of other metals (such as Al, Fe, and etc.) are given in Ref. [33]. The optical dielectric constants of silver obtained from Ref. [31] and [32] have been compared [34]. The observed differences are caused by their different measurement methods. The optical constants of Johnson and Christy were determined through measurements of reflection and transmission at normal incidence and transmission of TM-polarized light at 60°. The optical constants compiled by Palik, composed of the works of Dold and Mecke [35] between 0.125 and 0.98 eV, Winsemius et al. [36] between 0.65 and 3.3 eV, and Leveque et al. [37] from 3.3 to 26.5 eV, were obtained via polarimetric measurements and reflectance measurements using synchrotron radiation.

In this dissertation, the dielectric constant of silver is fit to the Palik data sets over a wide spectral range (0.1 to 6 eV) by a Lorentz–Drude model, which explicitly including both the intraband Drude free-electron effects and interband Lorentz bound-electron effects [38]. The LD model is expressed as

$$\epsilon_r(\omega) = 1 - \frac{f_0\omega_p^2}{\omega(\omega - i\Gamma_0)} + \sum_{j=1}^m \frac{f_j\omega_p^2}{\omega_j^2 - \omega^2 - i\Gamma_j\omega} \quad (2.20)$$

The LD model dielectric function agrees well in slope and magnitude with the Palik data sets, as depicted in Fig. 2.7. Also shown in this figure is the Brendel–Bormann (BB) model, which replaces a Lorentz oscillator with a superposition of an infinite number of

oscillators with Gaussian line shape. The details can be found in Ref. [38] and will not be discussed here. The optimal parameterization of the optical constants of silver by LD model is highlighted in Table 2.3.

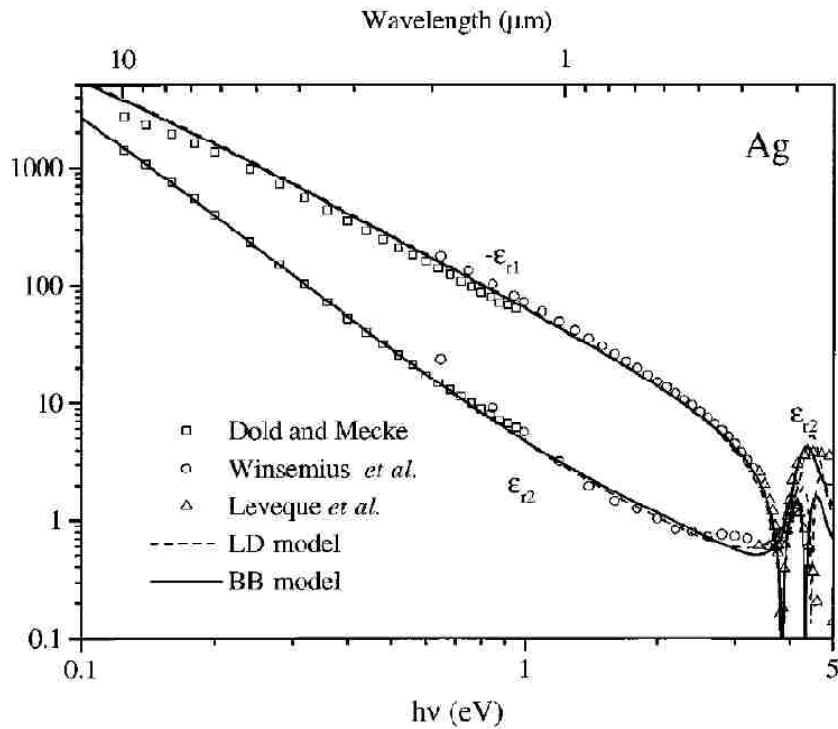


Fig. 2.7 (Taken from Ref. [38]) Real and imaginary parts of the optical dielectric constant of Ag using the Brendel–Bormann (BB) (solid curves) and LD (dashed curves) models. Also shown are the selected experimental data points from Dold and Mecke [35], Winsemius et al. [36], and Leveque et al. [37].

Table 2.3 Values of the LD Model Parameters [38]

Parameters	Metal										
	Ag	Au	Cu	Al	Be	Cr	Ni	Pd	Pt	Ti	W
f_0	0.845	0.760	0.575	0.523	0.084	0.168	0.096	0.330	0.333	0.148	0.206
Γ_0	0.048	0.053	0.030	0.047	0.035	0.047	0.048	0.008	0.080	0.082	0.064
f_1	0.065	0.024	0.061	0.227	0.031	0.151	0.100	0.649	0.191	0.899	0.054
Γ_1^a	3.886	0.241	0.378	0.333	1.664	3.175	4.511	2.950	0.517	2.276	0.530
ω_1^a	0.816	0.415	0.291	0.162	0.100	0.121	0.174	0.336	0.780	0.777	1.004
f_2	0.124	0.010	0.104	0.050	0.140	0.150	0.135	0.121	0.659	0.393	0.166
Γ_2	0.452	0.345	1.056	0.312	3.395	1.305	1.334	0.555	1.838	2.518	1.281
ω_2	4.481	0.830	2.957	1.544	1.032	0.543	0.582	0.501	1.314	1.545	1.917
f_3	0.011	0.071	0.723	0.166	0.530	1.149	0.106	0.638	0.547	0.187	0.706
Γ_3	0.065	0.870	3.213	1.351	4.454	2.676	2.178	4.621	3.668	1.663	3.332
ω_3	8.185	2.969	5.300	1.808	3.183	1.970	1.597	1.659	3.141	2.509	3.580
f_4	0.840	0.601	0.638	0.030	0.130	0.825	0.729	0.453	3.576	0.001	2.590
Γ_4	0.916	2.494	4.305	3.382	1.802	1.335	6.292	3.236	8.517	1.762	5.836
ω_4	9.083	4.304	11.18	3.473	4.604	8.775	6.089	5.715	9.249	19.43	7.498
f_5	5.646	4.384	—	—	—	—	—	—	—	—	—
Γ_5	2.419	2.214	—	—	—	—	—	—	—	—	—
ω_5	20.29	13.32	—	—	—	—	—	—	—	—	—

^aIn electron volts.

2.5 Surface Plasmon Polaritons Basics

Surface plasmon polaritons are the TM waves propagating along an interface between a dielectric and a conductor (usually metal) materials possessing opposite signs of the real part of their dielectric permittivities, evanescently confined in the perpendicular direction. The term “surface plasmon polariton” reflects the hybrid nature of this particular surface wave: it involves the resonant coupling between a light wave (photon) and a collective surface electron charge density oscillation (plasmon), which is schematically shown in Fig. 2.8.

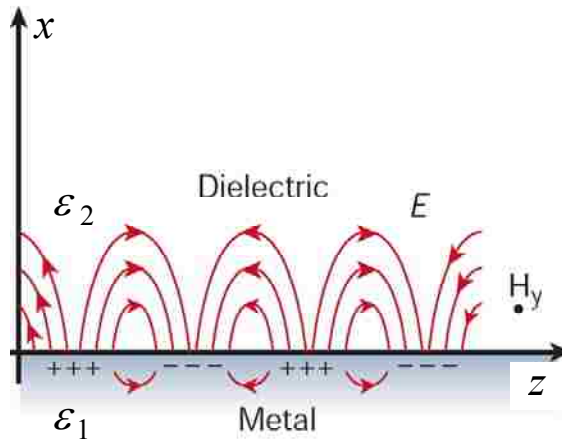


Fig. 2.8 SPPs at the interface between a metal and a dielectric material arise via the coupling between the TM EM wave and the collective surface charge oscillation [39].

In this section, the fundamentals of TM polarized SPPs in various geometries such as single metal-dielectric interface, multilayer structures (IMI and semi-infinite MIM waveguides) are reviewed. The TM polarized SP mode is uniquely characterized by its magnetic field lying in the plane of the metal-insulator surface and perpendicular to the wave propagation direction. The modal symmetry properties (either symmetric-S or antisymmetric- A) used to label the modes in this dissertation are therefore defined by the symmetry of the tangential magnetic field with respect to the waveguide median plane. This description differs from other literature definitions for IMI and infinite MIM structures, based on the tangential electric field in propagation direction.

2.5.1 SPPs at a Single Metal-Dielectric Interface

The dispersion relation $\omega(k_z)$ of SPPs, sustained at a single flat interface between semi-infinite metal and dielectric and propagating along the positive z direction (See Fig. 2.8), is given by (See appendix B: equation (B.4)) [40]:

$$k_z = \frac{\omega}{c} \sqrt{\frac{\epsilon_1 \epsilon_2}{\epsilon_1 + \epsilon_2}} \quad (2.20a)$$

$$k_{x1,2}^2 = \epsilon_{1,2} \left(\frac{\omega}{c}\right)^2 - k_z^2 \quad (2.20b)$$

Here and throughout Chapter 2.5.4, the complex dielectric functions of metal and dielectric are denoted as ϵ_1 and ϵ_2 , respectively.

Figure 2.9, taken from Ref. [41], shows the SPPs dispersion relation, using equation (2.20), for a Ag-SiO₂ interface. A cross section of the geometry is shown as an inset. Significant dispersion differences are revealed between panel (a) where the metal silver is described by a free electron gas model and panel (b) by the empirical optical constants of Johnson and Christy [31].

Panel (a), plotted with metal silver described by Drude model without damping, $\epsilon_1(\omega) = 1 - \omega_p^2/\omega^2$ with $\omega_p = 8.85 \times 10^{15} \text{s}^{-1}$, shows the existence of a “plasmon bandgap” between the surface plasmon frequency ω_{sp} and the plasma frequency ω_p . The surface plasmon frequency ω_{sp} is defined as the wavelength where $\epsilon_1' = -\epsilon_2$, thus $\omega_{sp} = \omega_p/\sqrt{1 + \epsilon_2}$. For energies inside this bandgap, the plasmon modes are forbidden with purely imaginary wave vectors (dotted line). Outside this plasmon bandgap, the allowed plasmon modes (solid lines) consist of the radiative plasmon-polariton (RPP) mode at higher energies ($\omega > \omega_p$) and the typical bound SPP mode at lower energies ($\omega < \omega_{sp}$). At small wave vectors corresponding to low frequencies, the bound SPP dispersion is asymptotically close to the light line, and the waves extend over many wavelengths into the dielectric region while negligible penetration into the conductor leading to highly delocalized fields. Thus SPPs at this regime are known as *Sommerfeld-*

Zenneck waves. Its characteristics are described by point D in Table 2.1. and Fig. 2.3.

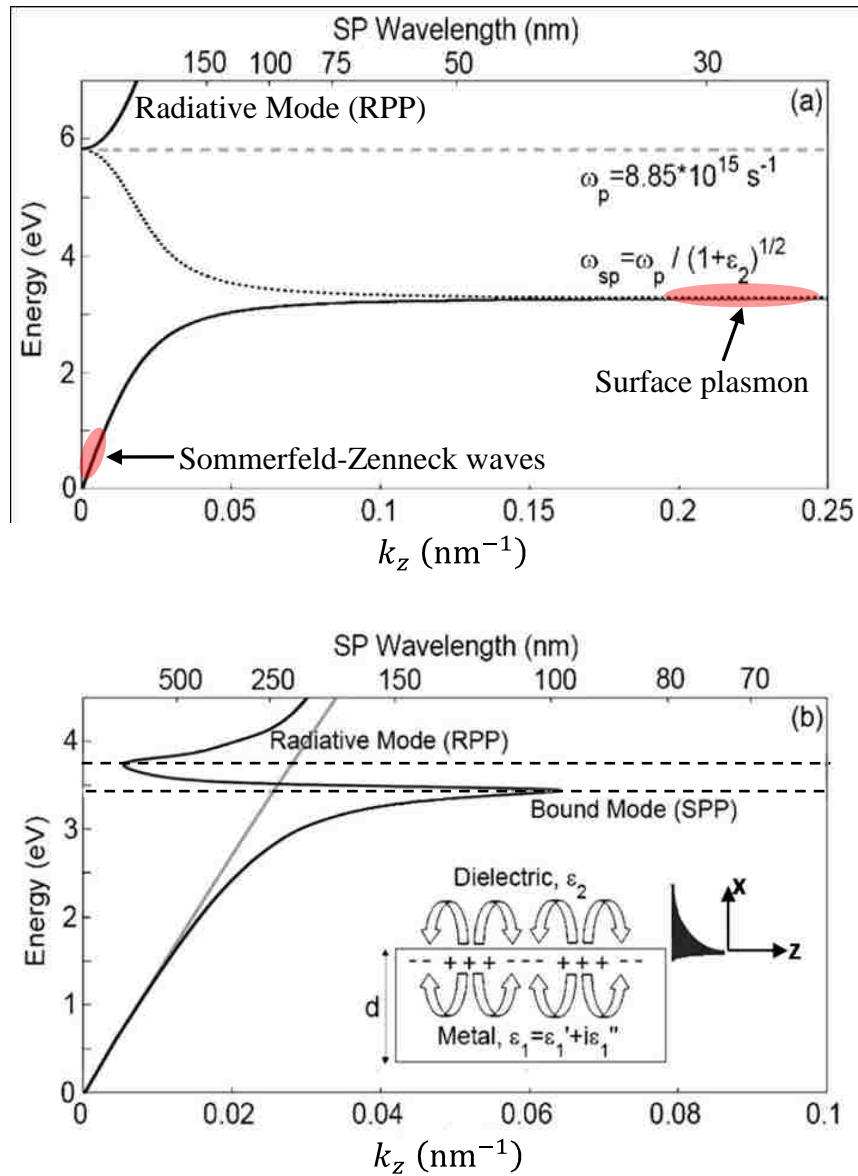


Fig. 2.9 (Take from Ref. [41]) Dispersion relations of SPPs at a single, flat Ag-SiO₂ interface computed using: (a) a free electron gas dispersion model, (b) the empirical optical constants of Johnson and Christy. The SiO₂ light line (gray) is included for reference.

At large wave vectors, the SPP dispersion is asymptotically close to ω_{sp} . The longitudinal wave vector k_z approaches infinity and the group velocity $v_g \rightarrow 0$ ($v_g =$

$d\omega/dk_z$) as the frequency approaches ω_{sp} . SPPs at this regime are electro static in character, and are thus known as the *surface plasmon* [42].

In contrast to panel (a), panel (b), plotted using the real metal including both free-electron and interband damping, shows that plasmon modes are allowed throughout the entire frequency range shown. RPP mode is observed at energies satisfying the relation $\epsilon_1'' > |\epsilon_1'|$. The SPP wave vector approaches the light line at low energies and terminates at a finite limit at ω_{sp} . For energies between the SPP and RPP modes, a mode with negative phase velocities is observed. This mode is labeled as a transition mode between the SPP and RPP modes.

The bound nature of SPP modes result in their dispersion curves lying to the right of the light line of dielectric. Thus, the momentum-mismatching between light and SPPs of the same frequency must be bridged by special techniques such as prism coupling or grating, and etc., which will be discussed in Chapter 2.5.4. The trade-off between the localization and loss is observed. The better the confinement, the lower the propagation length. More details can be found in Ref. [41].

2.5.2 SPPs in Insulator-Metal-Insulator Waveguide

In a multilayer waveguide structures consisting of alternating conducting and dielectric thin films, the bound SPPs sustained at each interface may interact with others forming coupled SP modes when the separation between adjacent interfaces is comparable to or smaller than the penetration depth of the single interface mode. As a block to understand the basic properties of coupled SPPs, two specific three-layer structures, an insulator-metal-insulator (IMI) waveguide as depicted in Fig. 2.10 and a

metal-insulator-metal (MIM) structure as depicted in Fig. 2.12, will be discussed in this and following sections, respectively.

A schematic of the IMI waveguide geometry [41], a thin metallic film of thickness d centered at $x = 0$ and embedded in two infinitely thick dielectric media, is shown in Fig. 2.10. The waves propagate along the positive z direction.

For a thin metal film, when the SPP evanescent field tails from each interface show considerable overlap, the coupling between individual SPs at each interface results in two bound and two leaky SP modes of opposite parities [43].

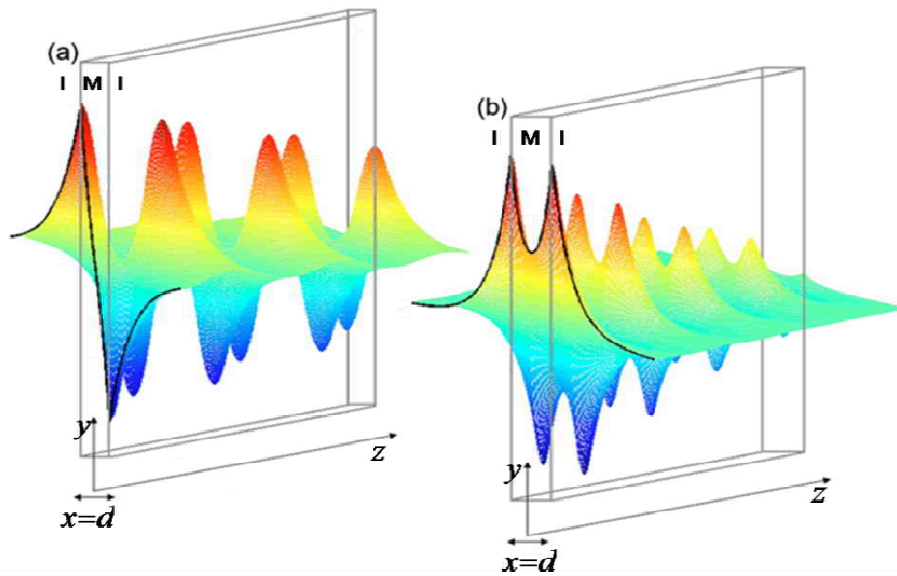


Fig. 2.10 Geometry and characteristic tangential magnetic field profiles H_y for a metal slab waveguide with metal thickness d . (a) The low-energy, antisymmetric mode (A); (b) The high-energy, symmetric mode (S). The wave propagates along the positive z direction. (Taken from Ref. [41]).

For a symmetric IMI structure, there exist two bound SPP modes: a low-energy odd mode as depicted in Fig. 2.10 (a), showing an antisymmetric distribution of the tangential magnetic field H_y (A mode), and a high-energy even mode as plotted in Fig.

2.10 (b), exhibiting symmetric H_y field distribution (S mode). Their dispersion relations take the following forms, respectively, [41]:

Low-energy, antisymmetric mode (A):

$$\varepsilon_1 k_{x2} + \varepsilon_2 k_{x1} \coth\left(\frac{-ik_{x1}d}{2}\right) = 0 \quad (2.21)$$

High-energy, symmetric mode (S):

$$\varepsilon_1 k_{x2} + \varepsilon_2 k_{x1} \tanh\left(\frac{-ik_{x1}d}{2}\right) = 0 \quad (2.22)$$

where k_{x1} and k_{x2} are defined by Eq. (2.20b).

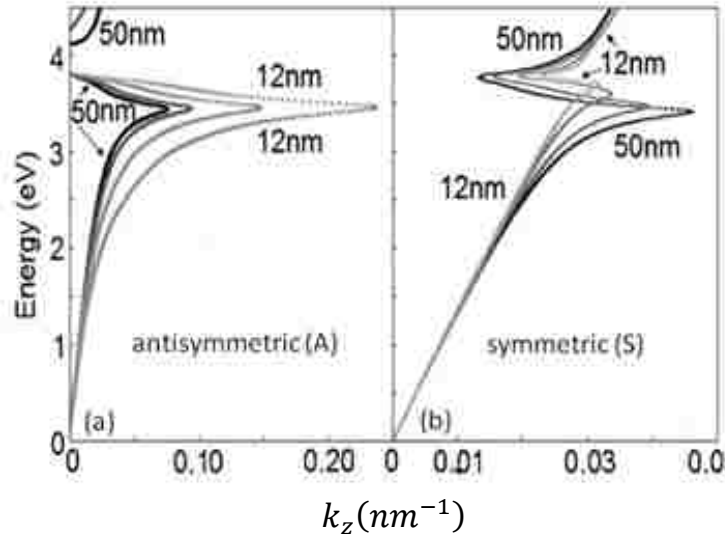


Fig. 2.11 Dispersion for the $\text{SiO}_2\text{-Ag-SiO}_2$ geometry for various Ag thicknesses (12, 20, 35, and 50 nm) using silver optical constants of Johnson and Christy. (a) Low-energy, antisymmetric mode (A); (b) High-energy, symmetric mode(S) [41].

Using (2.21) and (2.22) as well as the empirical Ag optical constants of Johnson and Christy, the dispersion curves for $\text{SiO}_2\text{-Ag-SiO}_2$ IMI structure with various metal

film thicknesses [41] are shown in Fig. 2.11. Similar to SPPs sustained at single metal-dielectric interface, the IMI dispersion relations also consists of SPP mode, RPP mode, and a transition mode with negative phase velocities lying between the SPP and RPP modes. For the A mode in panel (a), at a given frequency, the bound SPP mode is pushed toward larger wave vectors as film thickness decreases. A maximum finite wave vector is reached at the frequency ω_{sp} . A forbidden band exists between SPP and RPP branches. For the S mode in panel (b), the bound SPPS mode, in contrast to the flattening of A mode, is getting stiffer with smaller wave vector at the same frequency with decreasing film thickness. The SPP doesn't asymptote to ω_{sp} . Before bending back to the transition mode, the maximum finite wave vector is reached at energy higher than ω_{sp} as the film thickness decreases.

The longitudinal electric field component E_z , given by $\partial H_y / \partial x$, is the dominant electric field of SPs and has opposite symmetry to that of field H_y . In contrast to the low-energy A mode, the high-energy S mode exhibits a longitudinal electric field node in the IMI waveguide median plane and significantly lower energy density magnitudes at the metal-dielectric interface. Thus the S mode has propagation loss one to two orders magnitude lower than the A mode and has been named as long-range surface plasmon (LRSP) [44].

The comprehensive behaviors, including dispersion, propagation, field skin depth and energy density, of mode A and S with various film thickness have been investigated in Ref. [41]. With decreasing film thickness, the A and S modes exhibit opposite behaviors with respect to the propagation constant (this has been described above), the attenuation and the skin depth into the dielectric (defined as the $1/e$ decay length of the

SP electric field into the dielectric) — the bound S mode shows increasing propagation length, because of less and less penetration of the E_z field component into the metal, decreasing wave vector and increasing skin depth into the dielectric. Conversely, the bound A mode exhibits decreasing propagation length, because of more and more field confinement in the metal, increasing wave vector and decreasing skin depth into the dielectric. For both the A and S modes, the propagation distances generally decrease with increasing SP momentum and the dielectric energy density generally decreases with decreasing film thickness. The energy density extends well into the dielectric for the symmetric mode while fall fairly quickly for the antisymmetric mode.

In a symmetric IMI geometry, both bound S and A modes do not show a cutoff thickness. While for a thin metal film embedded in an asymmetric environment, much more complicated situation occurs and will not be described here. The detailed results can be found in Ref. [43].

2.5.3 SPP Gap Modes in Semi-infinite Metal-Insulator-Metal Waveguide

In IMI waveguides, there exists a trade-off between localization and loss of plasmon modes — the long-range waveguiding based on the LRSP mode sustained by thin IMI waveguides (corresponding to $d < 20\text{nm}$) is accompanied by weak confinement with the field evanescent tail extending over multiple wavelengths into the dielectric region. For example, for LRSP mode of a thin Ag film ($\sim 10\text{nm}$) excited at telecommunications frequencies ($\sim 1.5\mu\text{m}$), the electric field skin depths can exceed $5\mu\text{m}$ [41, 43]. Thus subwavelength confinement cannot be achieved. The low confinement of IMI geometry fundamentally limits the packing density of IMI waveguides [45] and

therefore makes IMI structures unsuitable for designing subwavelength photonic and plasmonic structures.

In contrast, for metal-insulator-metal (MIM) geometry, the SPP mode confinement is determined by field decay length into the metallic regions. For Ag-SiO₂ interface, the SPP skin depth into the metal remains roughly constant at ~20nm for wavelengths beyond the plasmon resonance [41]. Therefore, subwavelength confinement and potential high packing density of MIM waveguides can be achieved with subwavelength-sized dielectric core. In terms of creating highly integrated subwavelength plasmonic structures, MIM geometry has been proposed as an alternative to the low-confined IMI waveguide structure from two points of view – (i) MIM SPs waveguides offer higher confinement factors and smaller pitch size between adjacent waveguides [45]. For example, at working wavelength $\lambda = 1.5 \mu\text{m}$, Al-based MIM structures meet the requirements of 700nm pitch between adjacent waveguide cores and a 50 μm -propagation length; (ii) MIM 90° bends and splitters can potentially be realized with no additional losses over a wide frequency range [46].

A schematic of semi-infinite MIM waveguide geometry [47], an insulator core layer of thickness d centered at $x = 0$ surrounded by two metallic half-spaces, is shown in Fig. 2.12. The waves propagate along the positive z direction. The propagating EM modes are confined in the subwavelength dielectric core in the form of a coupled SP modes supported by the metal-insulator boundaries. As the plasmon mode splitting in IMI waveguides, MIM can also support two SPP modes — a high-energy, antisymmetric field mode shown in panel (a) and a low-energy, symmetric field mode shown in panel (b) [47-49].

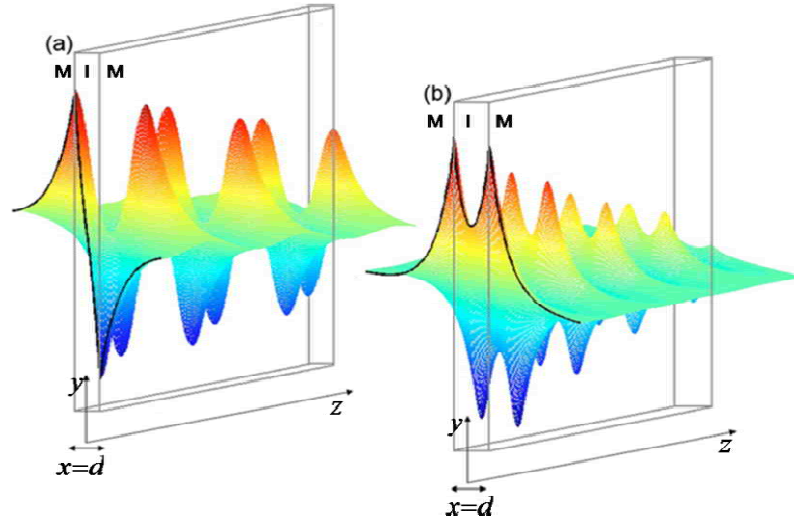


Fig. 2.12 Geometry and characteristic tangential magnetic field profile H_y for the semi-infinite MIM waveguide with core insulator thickness d . (a) The high-energy, antisymmetric field mode (A); (b) The low-energy, symmetric field mode (S). The waves propagate along the positive z direction. (Taken from Ref. [47]).

The MIM SPP dispersion relations can easily be obtained from the IMI dispersion formulations (See (2.12) and (2.22)) by switching the subscripts 1 and 2. Computed with the empirical Ag optical constants of Johnson and Christy, the SPP dispersion curves for Ag-SiO₂-Ag MIM structures with various oxide layer thicknesses [47] are illustrated in Fig. 2.13. Both the antisymmetric and symmetric modes exhibit plasmon-like dispersion, while the results show marked differences in their behaviors with decreasing film thickness from that observed in IMI waveguides.

In panel (a), the high-energy antisymmetric (A) mode is seen to exhibit dispersion behaviors similar to that of the low-energy IMI antisymmetric mode, with larger wave vectors achieved at lower energies for thinner films. In simple words, the MIM A mode gets flattened with decreasing gap distance between the two metal claddings. As IMI waveguide, the dispersion curve reaches a maximum, finite wave vector at the surface

plasmon frequency ω_{sp} , and then cycle through the higher energy modes [41]. However, unlike IMI structures whose SP momentum always exceed photon momentum, the MIM A mode dispersion curves cross the single-interface (thick insulator film) limit with the low-energy portions lying above the limit. In addition, the low-energy asymptotic behavior of the A mode dispersion curve indicates low effective index of this mode, with thick films ($d \sim 50$ nm) achieving effective indices as low as $n = 0.15$.

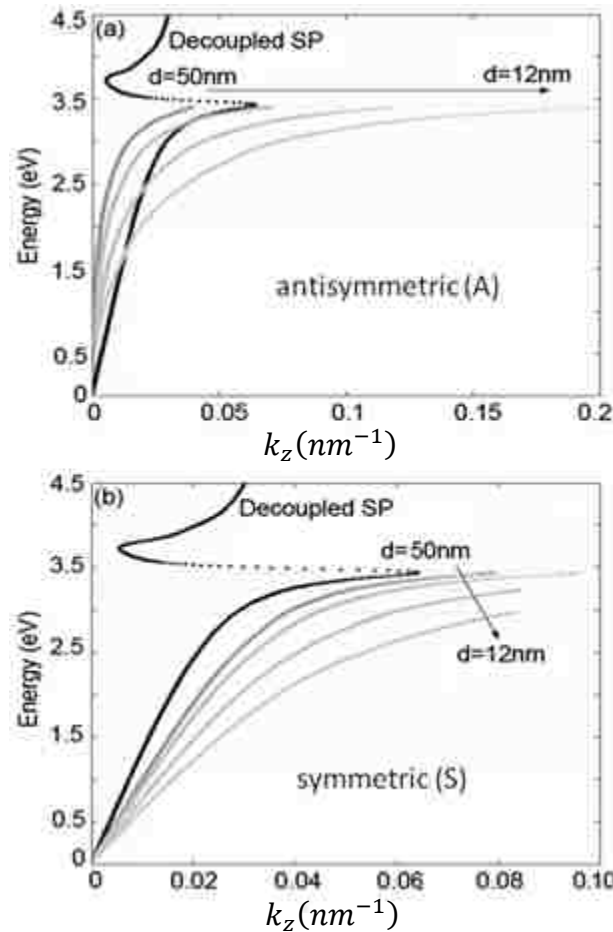


Fig. 2.13 TM dispersion relations of MIM (Ag-SiO₂-Ag) structures for various oxide thicknesses (12, 20, 35, and 50 nm) using silver optical constants of Johnson and Christy. Dispersion for a Ag-SiO₂ interface is plotted in black as reference. (a) High-energy antisymmetric (A) mode; (b) Low-energy symmetric (S) mode.

In contrast to IMI high-energy symmetric mode whose dispersion gets stiffened to approach the light line for thinner films, the MIM low-energy symmetric (S) mode dispersion, shown in panel (b), behaving like that of the low-energy IMI antisymmetric mode, gets flattened away from the single-interface limiting case, i.e. with larger wave vectors achieved at lower energies for thinner films. Unlike MIM antisymmetric mode which does not have a cut-off gap size, the MIM symmetric mode exhibits a cut-off for core films thinner than 20 nm, terminating on energies below ω_{sp} .

2.5.4 Optical Excitation of Surface Plasmon Polaritons

To excite a SPPs propagating along a flat metal-dielectric interface by a TM-polarized incident light beam from the adjacent dielectric medium, the incident light parallel wave vector component must equal the SPP wave vector, which is defined by $k_z = (\omega/c)\sqrt{\epsilon_1\epsilon_2/(\epsilon_1 + \epsilon_2)}$ (See equation (2.20a)). As seen from the dispersion relation shown in Fig. 2.9(b), the bound nature of SPP mode results in its dispersion curve lying to the right of the light line of the dielectric medium. Thus, SPPs can't be excited directly by light beam unless special phase-matching techniques, such as prism coupling or grating, and etc., are employed [40]. While the SPPs can also be excited by end-fire coupling technique, which is based on spatial-mode matching instead of phase-matching. This coupling scheme will not be discussed. The phase mismatch between the photon and SPPs can be bridged by using photon tunneling in the total internal reflection (TIR) geometry (Kretschmann and Otto configurations), or diffraction effects, or near-field effect, which are schematically shown in Fig. 2.14.

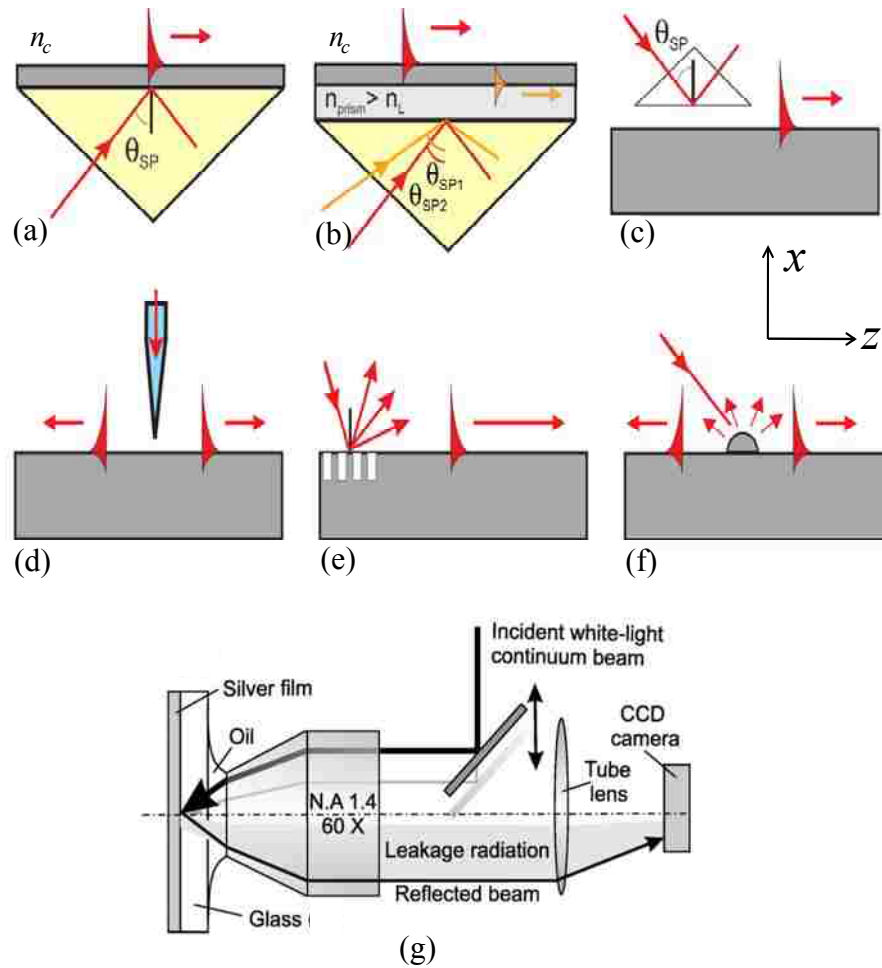


Fig. 2.14 SPPs excitation configurations: (a) Kretschmann geometry, (b) two-layer Kretschmann geometry, (c) Otto geometry, (d) excitation with a near-field scanning optical microscopy (NSOM) probe, (e) diffraction on a grating, (f) diffraction on surface features, and (g) excitation with highly focused optical beams. Note: subplots (a)-(e) are taken from Ref. [50] and subplot (f) is gotten from Ref. [51].

(i) Prism Coupling

The prism coupling technique for SPPs excitation is also known as ATR. It involves photon tunneling to the metal-dielectric interface where SPP excitation occurs. Three different geometries for prism coupling are depicted in subplots (a)-(c).

The most common approach is the Kretschmann configuration (Fig. 2.14a) [52], in which a thin metal film is sandwiched between a higher-index insulator, normally in

the form of prism (n_{prism}), and a lower-index insulator (n_c). For simplicity, we assume the lower-index insulator to be free space ($n_c = 1$). The metal film is illuminated through the prism at an incidence angle of θ greater than the critical angle for TIR. The photon momentum is increased in the optically denser medium. Thus the in-plane momentum $k_z = k_0 n_{prism} \sin \theta$ is sufficient to excite SPPs at the lower-index dielectric-metal interface, in current case at the air-metal interface. Therefore the dashed portion of the SPPs dispersion at the air-metal interface, possessing wave vectors between the respective light lines of air and the prism, can be excited (See Fig. 2.15). At the phase-matching incidence angle θ_{SP} at which the photon in-plane wave vector equals the wave vector of SPP at the air-metal interface, resonant light tunnels through the metal film to excite SPP at the air-metal interface. The excitation of SPPs is accompanied with a minimum in the reflected beam intensity. The SPP at the prism-metal interface, however, can't be excited since its SPP dispersion lies outside the prism light cone (See Fig. 2.15).

In a two-layer Kretschmann geometry (Fig. 2.14b), we still assume $n_c = 1$, and an additional dielectric layer with a refractive index (n_L) smaller than n_{prism} is inserted between the prism and the metal film, the photon tunnels through this additional dielectric layer to excite SPP at the inner metal interface. Therefore, both SPPs at the metal film interface pair can be excited at different angles.

In the Otto configuration (Fig. 2.14c) [53], in which the prism and the metal film are separated by a thin air gap, TIR takes place at the prism-air interface and the evanescent field tunnels through the air gap to provide resonant excitation of SPP at the inner air-metal interface. The Otto configuration is preferable in two cases – (i) When

the Kretschmann geometry is not suitable for thick metal films; (ii) When direct contact with the metal surface is undesirable.

The prism coupling technique can also be used for exciting thin metal film coupled SPP mode pair. Its usage for finite MIM SPP excitation will be discussed in Chapter 4. In the two-layer Kretschmann geometry, by using an appropriate index-matching fluid (its index matches to n_c), as the layer between the prism and metal, both the long-ranging low-energy symmetric mode and the high-energy antisymmetric mode of higher attenuation have been excited [54].

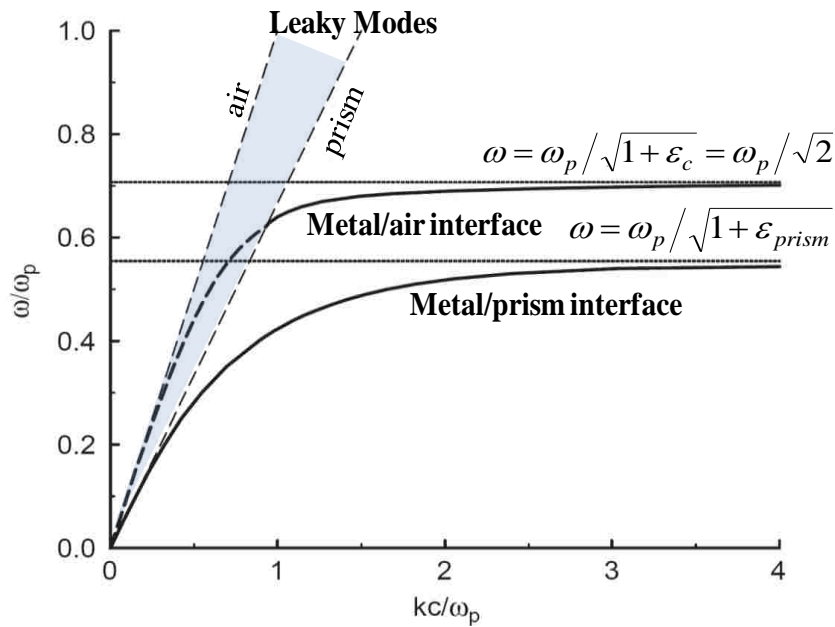


Fig. 2.15 Prism coupling and SPP dispersions at the interfaces of a thin metal film bounded with a vacuum ($\epsilon_c = 1$) and a prism ($\epsilon_{prism} = 2.25$). Also plotted are the vacuum and prism light lines (dashed lines) and the corresponding surface plasmon frequencies (dotted lines). The dashed portion of SPP at the metal-air interface, lying to the right of the vacuum light line while inside the prism light cone, is accessible. This excited SPP localizes at the metal-air interface and leaks energy into the prism. The metal used for plots is silver with $\omega_p = 11.9989 \times 10^{15} \text{ s}^{-1}$ and a thickness of 30 nm. Note: this figure is modified from Fig. 4 in Ref. [50].

In all above mentioned prism coupling geometries, the excited SPPs, with wave vectors lying within the prism light cone (Fig. 2.15), are inherently leaky waves. The light is coupled into the SPP mode through the prism, and at the same time light from the SPP mode is also coupled out through the prism. Therefore, in addition to the inherent metal energy dissipation, the leaky waves also lose their energy by leakage of radiation into the prism. The minimum reflected beam intensity is resulted from the destructive interference between the SPP leaky radiation and the reflected part of the excitation beam.

(ii) Near Field Excitation

In contrast to the macroscopic SPPs excitation schemes such as prism or grating coupling, near-field optical microscopy acts as a point source to provide local excitation of SPPs over an subwavelength area [55]. In the typical near-field SPPs excitation configuration sketched in Fig. 2.14(d), the illumination light from a small probe tip of aperture size a ($a \lesssim \lambda_{spp} \lesssim \lambda_0$) has wave vectors $k \gtrsim k_{spp} \gtrsim k_0$, thus allowing a near-field coupling of the phase-matched subwavelength aperture diffracted light into SPPs. Using such probes in NSOM, SPPs at different positions of the metal surface can be locally excited.

(iii) Grating Coupling

Grating coupling, formed by patterning the metal surface with periodic grooves or holes, uses the diffraction effects to overcome the phase-mismatching problem in SPP

excitation. For the simple 1D grating of grooves depicted in Fig. 2.15 (e), the diffracted light components satisfying the phase-matching condition

$$k_{spp} = k_0 n_c \sin\theta \pm m\Lambda \quad (2.23)$$

will be coupled to SPPs, while at the same time the reverse out-coupling process also occurs: the propagating SPPs along a surface with grating modulation couple back to light and then radiate. In (2.23), k_0 is the vacuum wave number, n_c is the refractive index of the medium through which the metal film is illuminated, θ is the illumination beam incidence angle with respect to the normal direction, $m = 1, 2, 3 \dots$, $\Lambda = 2\pi/b$ is the reciprocal vector of the grating, and b is the grating period. Similar to prism coupling, the excitation of SPP is also associated with a minimum reflected light intensity.

(iv) Excitation Using Surface Features Diffraction

On a randomly rough surface, in the near-field region the diffracted light components possess all wave vectors and thus SPPs can be excited by conventional illumination without any special arrangements. Unlike using the diffraction grating, this is a non-resonant excitation. Similarly, SPPs can also be optically excited through light diffraction from surface features (Fig. 2.14 (f)) [56].

(v) Excitation Using Highly Focused Optical Beams

Figure 2.14 (g) sketches a typical setup of using highly focused optical beams for SPP excitation [57] in a similar manner to the Kretschmann configuration. Instead of using prism to satisfy the TIR and SPP resonance condition, a high-numerical index-matched oil-immersion microscope objective is brought into contact with the glass

substrate, on which deposited a thin metal film. Owing to the high numerical aperture of the lens, the broad angular spread of the focused illumination beam is large enough to have the resonance wave vector for SPP excitation at the metal-air interface. The highly focused illumination beam provides localized SPPs excitation over a diffraction-limited area.

References

- [1] R. Janaswamy, "Asymptotic evaluation methods," class notes for ECE 69700, Department of Electrical and Computer Engineering, University of Massachusetts.
- [2] A. Ishimaru, *Electromagnetic Wave propagation, Radiation, and Scattering*, Prentice Hall, New Jersey (1991).
- [3] J. Chilwell and I. Hodgkinson, "Thin-films field-transfer matrix theory of planar multilayer waveguides and reflection from prism-loaded waveguides," *J. Opt. Soc. Am. A*, **1**, 742 (1984).
- [4] R. E. Smith and S. N. Houde-Walter, "Leaky guiding in nontransparent waveguides," *J. Opt. Soc. Am. A* **12**, 715 (1994).
- [5] T. Tamir ed., *Guided-wave Optoelectronics*, Springer Verlag, Berlin, (1990).
- [6] D. Marcuse, *Theory of Dielectric Optical Waveguides*, Academic Press, New York, (1974).
- [7] R. E. Collin, *Field Theory of Guided Waves*, McGraw-Hill, New York, (1960).
- [8] M. Miyagi and G. L. Yip, "Design theory of high-Q optical ring resonator with asymmetric three-layered dielectrics," *Opt. Quantum Electron.* **10**, 425 (1978).
- [9] K. Ogusu, M. Miyagi, and S. Nishida, "Leaky TE modes on an asymmetric three-layered slab waveguide," *J. Opt. Soc. Am.* **70**, 48 (1980).
- [10] C. W. Hsue and T. Tamir, "Evolution of transverse-electric surface and leaky waves guided by an asymmetric layer configuration," *J. Opt. Soc. Am. A* **1**, 923 (1984).
- [11] M. Mongiardo and T. Rozzi, "Continuous spectrum, characteristic modes, and leaky waves of open waveguides," *IEEE Trans. Microwave Theory Tech.* **41**, 132 (1993).
- [12] A. S. Snyder, "Leaky-ray theory of optical waveguides of circular cross section," *Appl. Phys.* **4**, 273 (1974).
- [13] R. Sammut and A. W. Snyder, "Leaky modes on a dielectric waveguide: Orthogonality and excitation," *Appl. Opt.* **15**, 1040 (1976).

- [14] V. V. Shevchenko, "The expansion of the fields in open waveguides in proper and improper modes," *Radio Phys. Quantum Electron.* **14**, 972 (1974).
- [15] T. Tamir and F. Y. Kou, "Varieties of leaky waves and their excitation along multilayered structures," *IEEE J. Quantum Electron.* **22**, 544 (1986).
- [16] L. Tomer, F. Canal, and J. Hernandez-Marco, "Leaky modes in multilayer uniaxial optical waveguides," *Appl. Opt.* **29**, 2805 (1990).
- [17] S. L. Lee, Y. Chung, L. A. Coldren, and N. Dagli, "On leaky mode approximations for modal expansion in multilayer open waveguides," *IEEE J. Quantum Electron.* **31**, 1790 (1995).
- [18] A. W. Snyder and J. D. Love, *Optical Waveguide Theory*, London, Chapman and Hall, (1983).
- [19] C. Vassallo, *Optical Waveguide Concepts*, Elsevier, (1991).
- [20] P. Benech and D. Khalil, "Rigorous spectral analysis of leaky structures: Application to the prism coupling problem," *Opt. Commun.* **118**, 220 (1995).
- [21] V. V. Shevchenko, *Continuous Transitions in Open Waveguides*, Boulder, Golem Press, (1971).
- [22] A. K. Ghatak and K. Thyagarajan, *Optical Electronics*, Cambridge Univ. Press, London, (1989).
- [23] G. W. Hanson and A. B. Yakovlev, "Investigation of mode interaction on planar dielectric waveguides with loss and gain," *Radio Sci.* **34**, 1349 (1999).
- [24] T. Tamir, "Wave-number symmetries for guided complex waves," *Electron. Lett.* **3**, 180 (1967).
- [25] B. Yakovlev and G. W. Hanson, "Analysis of mode coupling on printed transmission lines using morse critical points," *IEEE Trans. Microwave Theory Tech.* **46**, 966 (1998).
- [26] M. Golubitsky and D. G. Schaeffer, *Singularities and Groups in Bifurcation Theory*, Vol. 1, Springer-Verlag, New York, (1985).
- [27] R. Seydel, *Practical Bifurcation and Stability Analysis*, 2nd Ed., New York: Springer-Verlag, (1994).

- [28] A. B. Yakovlev and G. W. Hanson, "On the nature of critical points in leakage regimes of a conductor-backed coplanar strip line," *IEEE Trans. Microwave Theory Tech.* **45**, 87 (1997).
- [29] G. W. Hanson and A. B. Yakovlev, "An analysis of leaky-wave dispersion phenomena in the vicinity of cutoff using complex frequency plane singularities," *Radio Sci.* **33**, 803 (1998).
- [30] H. A. Lorentz, *The Theory of Electrons*, New York, Dover, (1952).
- [31] P. B. Johnson and R. W. Christy, "Optical constants of the noble metals," *Phys. Rev. B* **6**, 4370 (1972).
- [32] E. Palik, *Handbook of Optical Constants of Solids*, Academic Press, New York, (1985).
- [33] M. A. Ordal, L. L. Long, R. J. Bell, S. E. Bell, R. R. Bell, R. W. Alexander, Jr., and C. A. Ward, "Optical properties of the metals Al, Co, Cu, Au, Fe, Pb, Ni, Pd, Pt, Ag, Ti, and W in the infrared and far infrared," *Appl. Opt.* **22**, 1099 (1983).
- [34] J. A. Dionne, L. A. Sweatlock, H. A. Atwater, and A. Polman, "Planar metal plasmon waveguides: frequency-dependent dispersion, propagation, localization, and loss beyond the free electron model," *Phys. Rev. B* **72**, 075405 (2005).
- [35] B. Dold and R. Mecke, "Optische Eigenschaften von Edelmetallen, Übergangsmetallen und deren Legierungen im Infrarot (1. Teil)," *Optik (Stuttgart)* **22**, 435 (1965).
- [36] P. Winsemius, H. P. Langkeek, and F. F. van Kampen, "Structure dependence of the optical properties of Cu, Ag and Au," *Physica B* **79**, 529 (1975).
- [37] G. Leveque, C. G. Olson, and D. W. Lynch, "Reflectance spectra and dielectric functions of Ag in the region of interband transitions," *Phys. Rev. B* **27**, 4654 (1983).
- [38] A. D. Rakić, A. B. Djurišić, J. M. Elazar, and M. L. Majewski, "Optical properties of metallic films for vertical-cavity optoelectronic devices," *Appl. Opt.* **37**, 5271 (1998).
- [39] W. L. Barnes, A. Dereux, and T. W. Ebbesen, "Surface plasmon subwavelength optics," *Nature* **424**, 824 (1988).
- [40] H. Raether, *Surface Plasmons on Smooth and Rough Surfaces and on Gratings*, Springer-Verlag, Berlin, (1988).

- [41] J. A. Dionne, L. A. Sweatlock, A. Polman, and H. A. Atwater, "Planar metal plasmon waveguides: frequency-dependent dispersion, propagation, localization, and loss beyond the free electron model," *Phys. Rev. B* **72**, 075405 (2005).
- [42] S. A. Maier, *Plasmonics: Fundamentals and Applications*, Springer, (2007).
- [43] J. J. Burke, G. I. Stegeman, and T. Tamir, "Surface-polariton-like waves guided by thin, lossy metal films," *Phys. Rev. B* **33**, 5186 (1986).
- [44] D. Sarid, "Long-range surface-plasma waves on very thin metal films," *Phys. Rev. Lett.* **47**, 1927 (1981).
- [45] R. Zia, M. D. Selker, P. B. Catrysse, and M. L. Brongersma, "Geometries and materials for subwavelength surface plasmon modes," *J. Opt. Soc. Amer. A* **21**, 2442 (2004).
- [46] G. Veronis and S. Fan, "Bends and splitters in metal–dielectric–metal subwavelength plasmonic waveguides," *Appl. Phys. Lett.* **87**, 131102 (2005).
- [47] J. A. Dionne, L. A. Sweatlock, and H. A. Atwater, "Plasmon slot waveguides: Towards chip-scale propagation with subwavelength-scale localization," *Phys. Rev. B* **73**, 035407 (2006).
- [48] B. Prade, J. Y. Vinet, and A. Mysyrowicz, "Guided optical waves in planar heterostructures with negative dielectric constant," *Phys. Rev. B* **44**, 13556 (1991).
- [49] F. Villa, T. Lopez-Rios, and L. E. Regalado, "Electromagnetic modes in metal-insulator-metal structures," *Phys. Rev. B* **63**, 165103 (2001).
- [50] A. V. Zayats, I. I. Smolyaninov, and A. A. Maradudin, "Nano-optics of surface plasmon polaritons," *Physics Reports-Review Section of Physics Letters* **408**, 131 (2005).
- [51] A. Bouhelier and G. P. Wiederrecht, "Excitation of broadband surface plasmon polaritons: Plasmonic continuum spectroscopy," *Phys. Rev. B* **71**, 195406 (2005).
- [52] E. Kretschmann and H. Raether, "Radiative decay of non-radiative surface plasmons excited by light," *Z. Naturforsch. A* **23**, 2135(1968).
- [53] A. Otto, "Excitation of nonradiative surface plasma waves in silver by the method of frustrated total reflection," *Z. Physik* **216**, 398 (1968).
- [54] J. C. Quail, J. G. Rako, H. J. Simon, and R. T. Deck, "Optical second-harmonic generation with long-range surface plasmons," *Phys. Rev. Lett.* **50**, 1987 (1983).

- [55] B. Hecht, H. Bielefeldt, L. Novotny, Y. Inouye, and D. W. Pohl, "Local excitation, scattering, and interference of surface plasmons," *Phys. Rev. Lett.* **77**, 1889 (1996).

- [56] L. Salomon, G. Bassou, H. Aourag, J. P. Dufour, F. de Fornel, F. Carcenac, and A. V. Zayats, "Local excitation of surface plasmon polaritons at discontinuities of a metal film: Theoretical analysis and optical near-field measurements," *Phys. Rev. B* **65**, 125409 (2002).

- [57] A. Bouhelier and G. P. Wiederrecht, "Excitation of broadband surface plasmon polaritons: Plasmonic continuum spectroscopy," *Phys. Rev. B* **71**, 195406 (2005).

Chapter 3 Bound and Leaky Modes of Planar Finite Metal-Insulator-Metal Plasmonic Waveguides

3.1 Numerical Method

The complex propagation constants as solutions of multilayer planar waveguide eigenvalue equation cannot be solved analytically. The TM modal solutions of finite planar MIM geometry are obtained numerically by using the standard thin film transfer matrix formalism (See Appendix C) with Newton-Raphson root searching algorithm (See Appendix D) in the complex wave vector plane.

3.2 Code Validation

Implementation of the above mentioned numerical method, combining the transfer matrix formalism with Newton-Raphson root searching algorithm, has been validated to an accuracy of 10^{-9} against previously published results for lossless and lossy bound and leaky waveguides as well as plasmonic waveguides [1-6]. In addition, its validation for planar waveguides with incorporation of active medium will be presented in Chapter 5.

3.3 SPPs in Finite Planar MIM Plasmonic Waveguides

The basics of SPPs sustained at a single interface between semi-infinite metal and dielectric media, and in IMI and infinite MIM waveguides, have been reviewed in Chapter 2.5. In terms of subwavelength confinement and creating highly integrated

plasmonic structures, MIM geometry has been proposed as an alternative to the low-confined IMI structure. However, previous studies on MIM structures examined either the MIM gap mode in the presence of semi-infinite metal half-spaces [5], a subset of the modes of the finite MIM structure [7, 8] or dealt with full dispersion relation for multiple-film geometries only under the assumption of free-electron metals [9]. Four SP modes exist for the finite thickness MIM structure due to splitting of the coupled plasmon modes for two interacting thin metal films. The complete SP mode set for finite planar MIM waveguides with real metals will be presented in this chapter, revealing both bound and leaky modes. For the leaky mode, a spectral gap forms at the light line and the mode becomes an “antenna” mode in the radiation region. This antenna mode allows angle-dependent free-space interaction with plasmonic devices and suggests steerable input and output coupling functions. The trade-offs posed by propagation lengths and confinement factors and their optimization for three bound SP modes are also described.

Due to the nature of SP modes excited on planar metal-insulator structures, only TM modes are discussed here. As described in Chapter 2.5, the modal symmetry properties (either symmetric-S or antisymmetric- A) used to label the modes are defined by the symmetry of the tangential magnetic field with respect to the waveguide median plane.

3.3.1 Dispersion and Spatial Mode Profiles

For simplicity, the symmetric MIM Ag-air-Ag waveguide embedded in free space was numerically analyzed. The waveguide is centered at $x = 0$ with the x -axis normal to

the interfaces and wave propagation is in the positive z direction. The dielectric constant of silver is fit to experimental data over a wide spectral range (0.1 to 6 eV) by a Lorentz–Drude model, including both the intraband Drude free-electron effects and interband Lorentz bound-electron effects [10]. The details have been explicitly described in chapter 2.4. The wavelength range showing anomalous dispersion behavior, where $k(\omega)$ decreases with increasing frequency, will not be covered here. The real part of longitudinal propagation constants, $\text{Re}\{k_z\}$, and field profiles of supported modes in MIM structure with insulator air core thickness $d_I = 300$ nm and metal Ag thickness $d_M = 50$ nm are illustrated in Fig. 3.1. The corresponding modal loss (the imaginary part of the propagation constant) and propagation length will be discussed in chapter 3.3.2.

As reviewed in chapter 2.5.2, the dispersion relation for thin metal film surface plasmons has an antisymmetric (A) low-energy (L) branch and a symmetric (S) high-energy (H) branch. When two identical metal films interact in the MIM structure, the thin metal film SP modes undergo mode splitting, lifting their degeneracy. Therefore, two mode pairs giving a total of four non-degenerate SP modes should be observed for two interacting metal films separated by a thin insulator layer.

As shown in Fig. 3.1(A), transition modes with negative phase velocities [11] exist between 3.55 - 3.84 eV and above that the radiative-coupled plasmon modes are observed. The transition modes originate from deviations in the metal from free-electron dielectric functions and will not be discussed further.

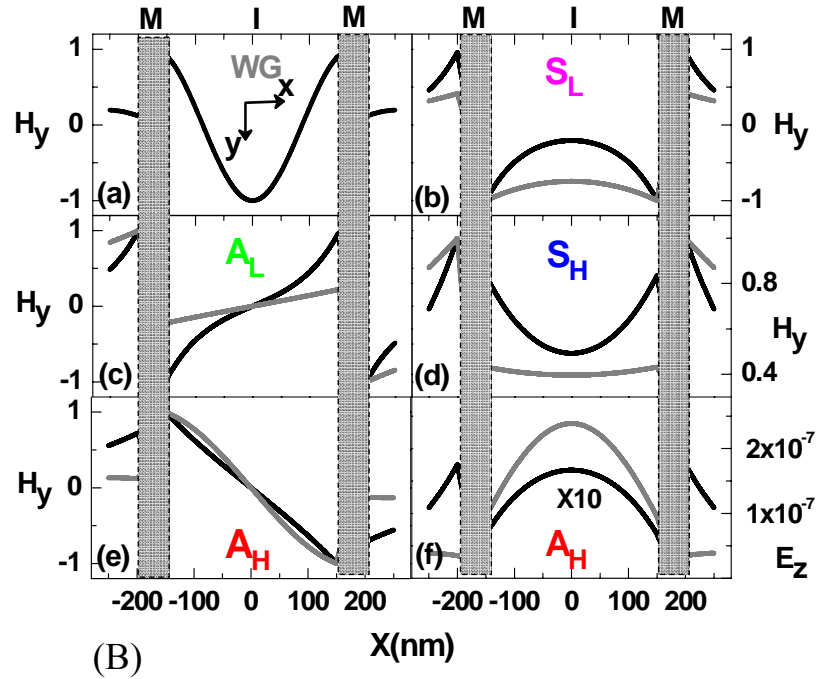
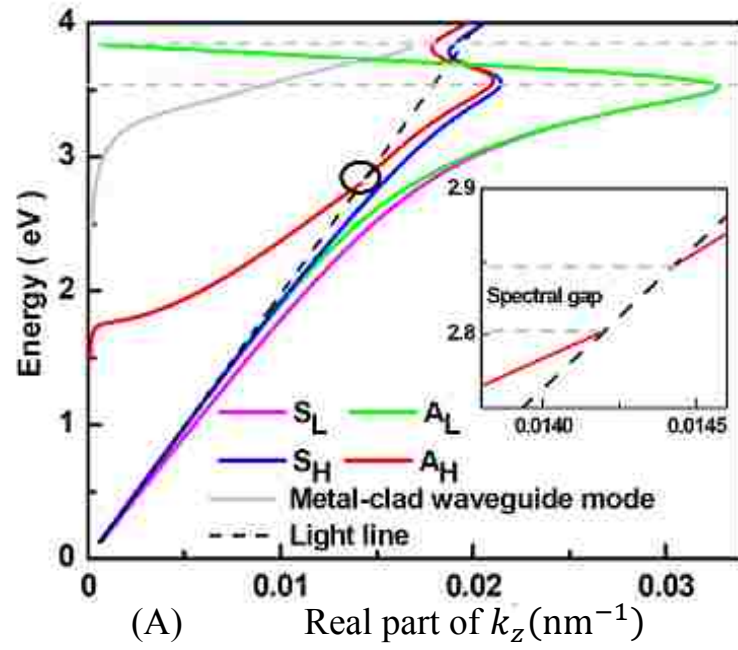


Fig. 3.1 TM dispersion relations (A) and characteristic tangential field profiles (B) for a symmetric Ag-air-Ag planar MIM structure bounded by free space with insulator thickness $d_I = 300$ nm and metal thickness $d_M = 50$ nm. (B) illustrates fields at vacuum wavelengths of 400 nm (black) and 600 nm (gray). Panels (a)-(e) plot the tangential magnetic field (H_y) for the conventional metal-clad waveguide mode, and modes S_L , A_L , S_H , and A_H respectively. Panel (f) shows the tangential electric fields (E_z) of mode A_H .

Along with conventional metal-clad waveguide mode(s) at higher frequencies, four SP modes are observed for finite MIM structures, and are labeled S_L , A_L , S_H and A_H according to their field profiles shown in panels (b) - (e) in Fig. 3.1(B). Labels S/A denote the symmetric/antisymmetric field distribution and subscript letter L/H associate the mode as originating from the low/high energy branch of the single metal film SPs.

The first conventional metal-clad waveguide mode (solid light gray in Fig. 3.1(A)) only exists above a cut-off energy around 2.45 eV (~ 500 nm), where the photon wavelength is shorter than the round-trip optical path inside MIM structure. In each SP mode pair, the symmetric mode always has lower energy comparing to the antisymmetric mode with the same wave vector. The three lowest energy modes (S_L , A_L and S_H) always lie to the right side of the light line and remain nonradiative SP modes throughout the whole wavelength range below 3.55 eV. The highest energy mode A_H is of particular interest since its dispersion relation crosses the light line and a significant portion at longer wavelengths lies above the free space light line, which normally separates nonradiative (bound) and radiative (leaky) regions. Consequently, the MIM waveguide will interact with free space without prism and grating via A_H mode leaky waves. Detailed properties of the A_H mode leaky wave as well as the spectral gap [12] (Fig. 3.1(a) inset) that exists between the bound and leaky regions will be presented in Chapter 3.3.3.

The magnitude of the fields inside the insulator is of interest for possible nonlinear applications of MIM SP waveguides. It is observed that the lowest (S_L) and highest (A_H) energy mode both have field maxima associated with the largest amount of charge located on the *internal* interface pair while in contrast, the A_L and S_H modes have

the most charge localized on the two *external* interfaces. Furthermore, panel (f) of Fig. 3.1(B) shows the peak localization of the E_z longitudinal electric field component associated with the collective electron oscillations transitioning from the external interfaces to the insulator as the A_H mode transitions from bound to leaky. For all modes, field amplitudes inside the metal films exponentially decay away from interfacial maximums, with more rapid decay in metal field values occurring at longer wavelengths owing to shorter skin depths. Consequently, the field strength inside the insulator decreases with increasing wavelength for the A_L and S_H modes where the field peaks are localized on the external metal-insulator interfaces.

Derived from Maxwell's equations, the transverse electric field E_x , given by $k_z H_y$, has the same symmetry as that of H_y , while in contrast the longitudinal electric field E_z , given by $\partial H_y / \partial x$, has the opposite symmetry to that of H_y . The E_x component is the dominant electric field. Thus the transverse electric field E_x inside the insulator is of particular interest if nonlinear optical effects are to occur in the MIM waveguides. The surface charge at the metal surfaces has the following symmetry properties as E_x . The charge distribution of the MIM coupled SP modes are sketched in Fig. 3.2. For the low-frequency mode pair S_L and A_L , the individual metal films have the same signed charge on their inner and outer interfaces while the high-frequency mode pair S_H and A_H have oppositely signed charges. The symmetric mode pair S_L and S_H have oppositely signed charges on their internal interfaces while for modes A_L and A_H , the reverse occurs. The largest amount of oppositely signed charge on the internal interfaces and hence the largest internal insulator fields, occurs for mode S_L , making it the best candidate for nonlinear applications.

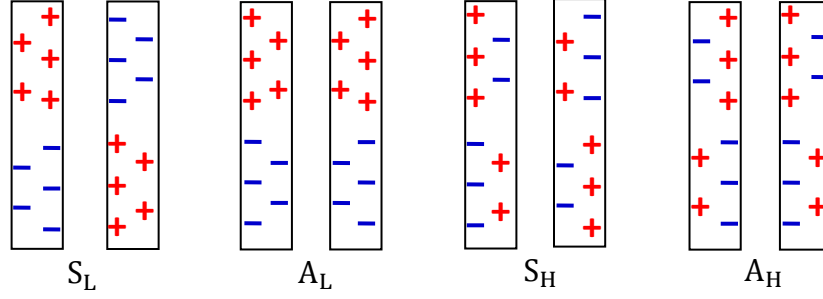


Fig. 3.2 Surface charge distributions associated with the four coupled SP modes in a finite planar MIM waveguide.

Figure 3.3 shows the dispersion behavior for MIM structures as a function of insulator thickness (Fig. 3.3(a)) and metal film thickness (Fig. 3.3(b)). The separation between the symmetric and antisymmetric modes for both the low energy and high energy mode pair increases with decreasing spacing between the two metal films. The S_H and S_L modes flatten away from the limiting IMI ($d_M=50$ nm) S_H and A_L modes, respectively as the insulator thickness is reduced, in contrast to the stiffening of the A_L mode. As the metal thickness decreases, the S_L and A_L modes flatten away from the limiting case semi-infinite MIM ($d_I=300$ nm) S_L and A_H modes, respectively, while the S_H mode stiffens with respect to the limiting case semi-infinite MIM S_L mode. The A_H mode exhibits more complicated variation with metal and insulator thickness that depends on considering the bound and leaky regions. The spectral gap, which will be discussed in Chapter 3.3.3, decreases with increasing metal and insulator thicknesses. The leaky regions move to lower energy with increasing insulator thickness.

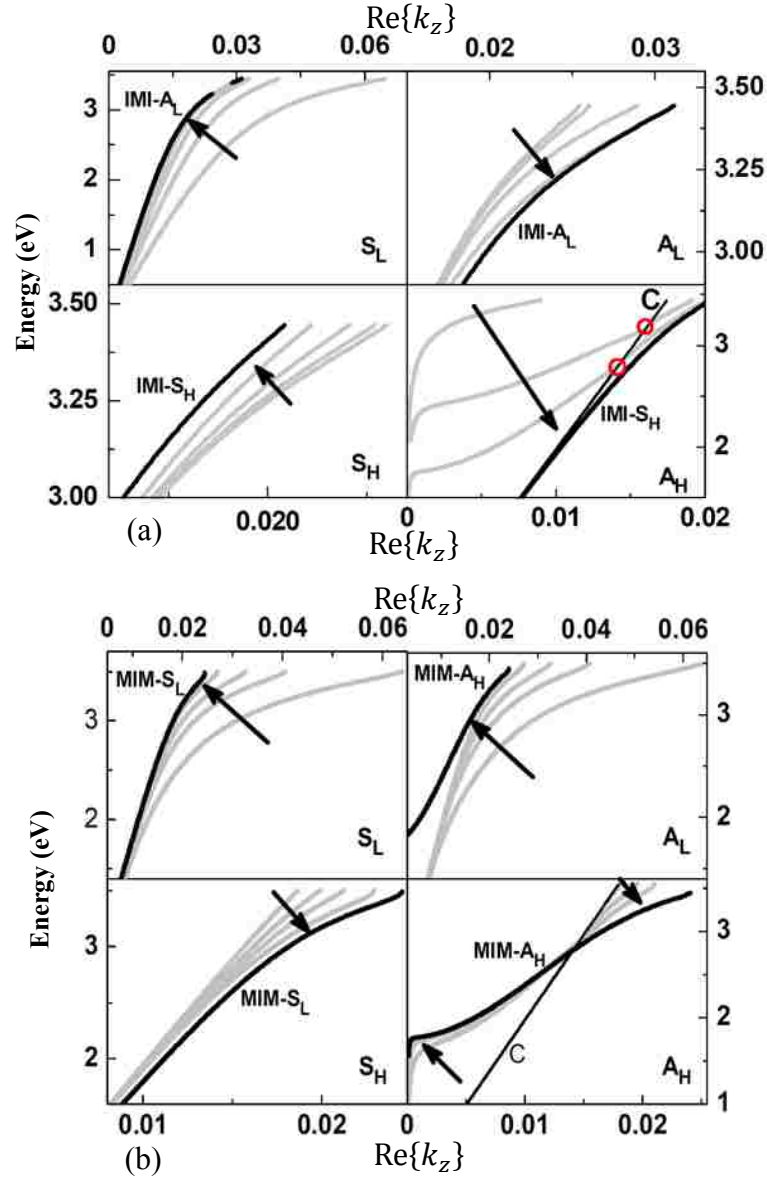


Fig. 3.3 MIM dispersion as a function of insulator thickness (a) and metal film thickness (b). The arrow indicates increasing thickness. (a): MIM geometry with metal thickness $d_M=50$ nm and insulator thickness $d_I=20, 50, 100$ and 200 nm (for modes S_L, A_L and S_H) and $d_I=100, 200$ and 300 nm (for mode A_H). Dispersion relations for air-Ag (50 nm)-air IMI waveguide, low energy antisymmetric modes (top two panels) and high energy symmetric modes (bottom two panels), are plotted in solid black lines as reference. (b): MIM geometry with insulator thickness $d_I=300$ nm and metal thickness $d_M=20, 35,$ and 50 nm. Dispersion relations for semi-infinite MIM waveguide, low energy symmetric modes (left two panels) and high energy antisymmetric modes (right two panels) are also plotted in solid black lines as reference.

3.3.2 Propagation and Confinement Factor

The propagation length L and the confinement factor Γ are two important parameters describing waveguide performance. The propagation length is governed by the modal loss and is defined as the distance where the traveling wave power magnitude decays by $1/e$. It is given by $L = 1/[2\text{Im}\{k_z\}]$, where k_z is the longitudinal propagation constant. Following the definition of confinement factor in dielectric waveguides, the confinement factor Γ represents the ratio of power propagating in the central insulator layer to the total power in the MIM waveguide [13] and is defined as follows:

$$\Gamma = \frac{\int_{\text{Insulator Layer}} \text{Re}(\mathbf{E}_x \times \mathbf{H}_y^*) dx}{\int_{-\infty}^{\infty} \text{Re}(\mathbf{E}_x \times \mathbf{H}_y^*) dx} \quad (3.1)$$

The wavelength-dependent propagation length and confinement factor of the MIM waveguide SP modes plotted in Fig. 3.1 are shown in Fig. 3.4. For the bound modes, longer propagation lengths occur at longer wavelengths where the dispersion is close to linear. Mode S_H possesses the longest and mode S_L the shortest propagation length. The long propagation length of modes A_L and S_H come at the expense of a low confinement factor. For modes A_L and S_H , the confinement factor decreases at longer wavelengths in contrast to mode S_L . Figure 3.1(B) shows the reason for this as at longer wavelengths, the fields of these two modes are localized on external interfaces and exponentially decay more rapidly inside the metal film owing to shorter skin depths, giving lower modal loss but also smaller fields inside the insulator. Since the confinement factors for the A_L and S_H modes are so low, the S_L mode, with both moderate propagation lengths and large confinement factors, becomes attractive for applications at long wavelength. Not shown in Fig. 3.4 are the characteristics of the 1st dielectric-core,

metallic-cladding waveguide mode with relatively lower modal loss than the S_L/A_L SP mode pair but with a high-energy mode cut-off and high modal dispersion. For mode A_H , the leaky portion has a shorter propagation length compared to any of the bound modes due to radiation loss and the material losses inside the metal. Upon closer scrutiny, the sharp decrease in propagation length occurring around 700 nm, is a transition from the shorter wavelength, antenna region to the longer wavelength, reactive region, and will be discussed in Chapter 3.3.3.

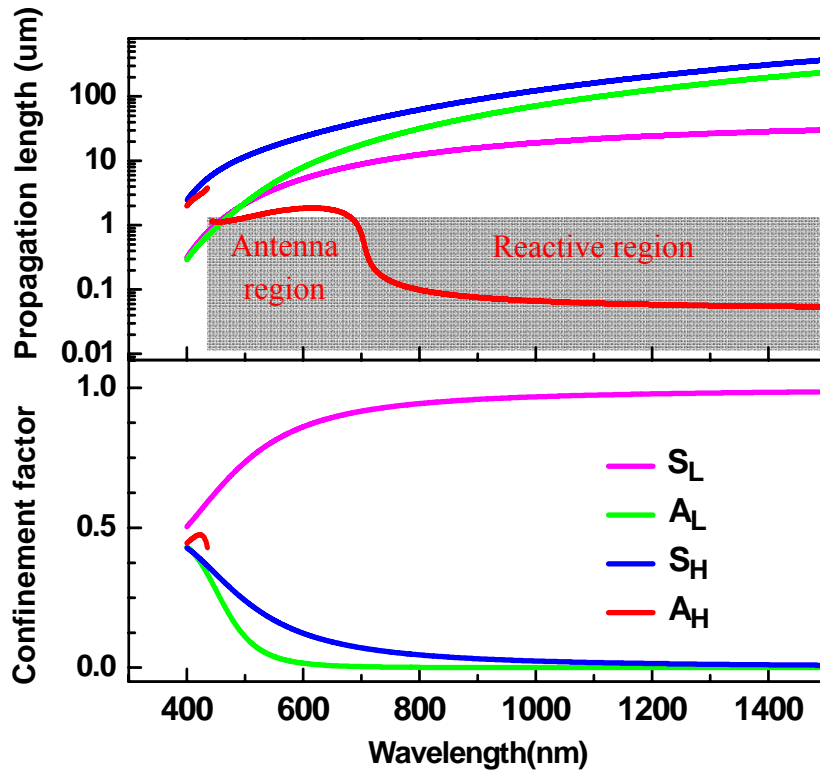
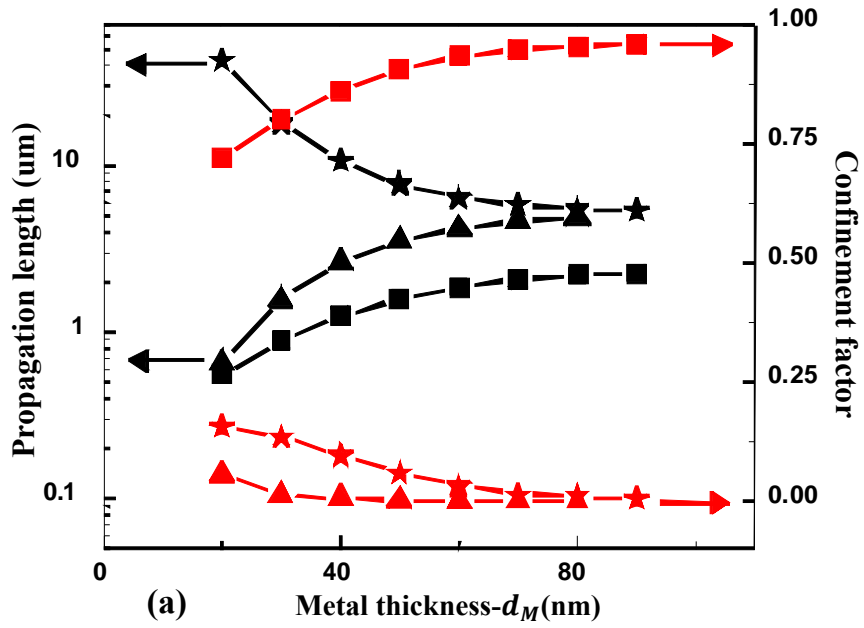


Fig. 3.4 Wavelength-dependent propagation length and confinement factor for a MIM structure of $d_I = 300$ nm and $d_M = 50$ nm. It has the same waveguide structure and mode color assignment as that in Fig. 3.1.



■ S_L
 ▲ A_L
 ★ S_H

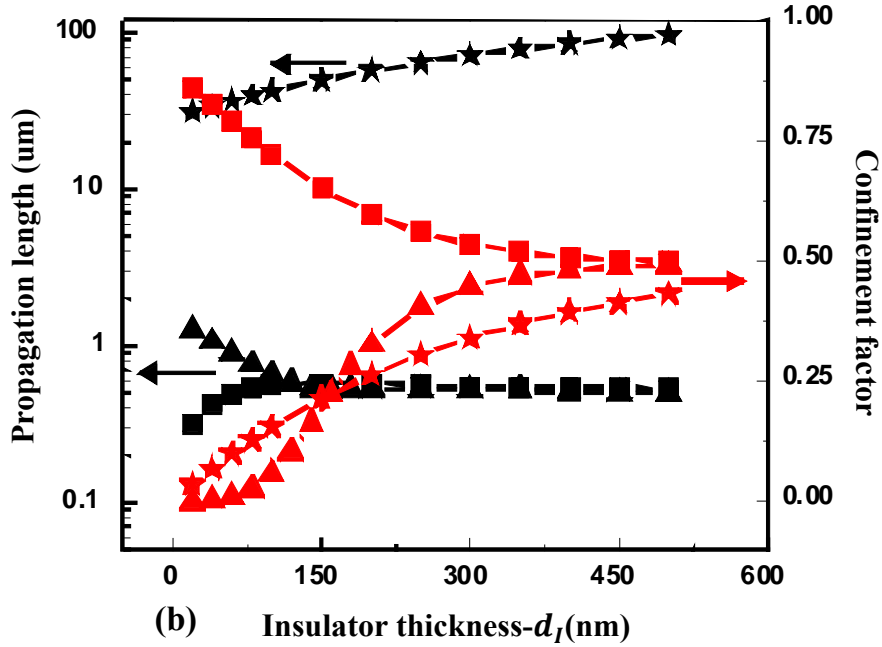


Fig. 3.5 Propagation length L (black lines and symbols) and confinement factor Γ (gray lines and symbols) for the MIM plasmonic waveguide at a free-space wavelength of 500 nm as a function of (a) metal ((b) insulator) thickness with fixed (a) insulator thickness $d_I=100$ nm ((b) metal thickness, $d_M=20$ nm).

The behaviors of L and Γ in MIM plasmonic waveguides as a function of metal and insulator thickness are summarized in Fig. 3.5. Thicker metal-insulator layers favor the S_L/S_H modes, respectively, with longer propagation distances as well as higher confinement factors. Maximum sub-wavelength confinement, far beyond that achievable in an IMI structure, is obtained in mode S_L at the cost of moderately higher loss. Mode S_H is characterized by longer propagation distances but only moderate confinement factors. It is also observed that the L and Γ of the MIM configuration asymptotically approaches that of the limiting IMI/semi-infinite MIM structure with increasing insulator-metal thickness, respectively, as expected.

Compared with the A_L and S_L mode pair, the S_H mode deviates from IMI characteristics over a larger range of insulator thicknesses. This reflects the fact that in the IMI high-energy mode branch, the SP field penetrates further into the adjacent dielectric. Waveguide mode A_L has extremely small confinement factors for MIM structures with metals thicker than about 50 nm and hence is probably not suitable in any application requiring confinement.

3.3.3 Leaky Wave Analysis

Figure 3.1 reveals that the highest energy MIM SP mode A_H consists of non-radiative (bound) and radiative (leaky) portions separated by a spectral gap at the light line. Detailed properties of the A_H mode leaky wave as well as the spectral gap (See Fig. 3.1(a) inset) will be discussed in this section.

The eigenmodes of 1D planar waveguide were discussed in Chapter 2.3.1 and their properties are summarized in Table 2.2. It is shown that the discrete leaky modes, possessing exponentially increasing fields (referred to as *improper* field profiles) in one or both of the bounding media (as opposed to bound modes with exponentially decaying *proper* field profiles away from the structure), are mathematically valid but “improper” solutions of the same eigenvalue problem used to find the guided modes. However improper solutions may be physically and experimentally real since we can describe leaky modes as a linear combination of radiation modes over a finite space adjacent to the waveguide and the leaky wave propagation constant can replace a continuous spectrum of radiation mode propagation constants [14-18].

As discussed in Chapter 2.3.2, the character of the eigenmode changes between *proper* and *improper* to make every “mode” analytically continuous in the complex frequency plane with every other “mode” [12]. Whether a *proper/improper* solution is physically real is determined by the requirement that the real part of effective modal index is greater/less than the index of outmost bounding media. Spectral gaps in the dispersion curve occur when a mode changes from bound to leaky upon crossing the light line.

The above mentioned dispersion behavior of *proper* and *improper* solutions and the occurrence of spectral gap were clearly shown in Fig. 2.6 and explained in Chapter 2.3.2.

Similarly, the MIM A_H mode crosses the light line thus changing in character from proper bound mode to improper leaky mode and the transition at the light line is characterized by a spectral gap. The occurrence of the spectral gap is explained as

follows: In the MIM structure, there are mathematically two complex solutions for the A_H mode – one proper and one improper. Individually, these complex solutions are continuously upon crossing the light line. While the bound mode (proper solution) becomes unphysical above the light line because the modal index is less than the outermost media index, and the leaky mode (improper solution) becomes unphysical below the light line because the modal index is greater than that of the outermost media. Consequently, there exists a spectral gap in the dispersion curve as the mode changes from bound to leaky upon crossing the light line.

(i) Leaky Mode Regimes: Antenna and Reactive

For MIM A_H mode, there is a significant portion at longer wavelengths lying above the light line. Above the light line, the mode is a physically leaky mode composed of two distinct regions: an antenna mode region defined by $\text{Re}\{k_z\} > \text{Im}\{k_z\}$, and characterized by the propagation of mode energy out of the waveguide, and a reactive mode region defined by $\text{Re}\{k_z\} < \text{Im}\{k_z\}$ [19]. The imaginary part of the transverse wave vector results in field growth outside the waveguide, but because the propagation constant is predominantly imaginary, radiation loss is limited.

(ii) Leaky Wave Radiation Pattern

Following the analysis of radiative modes in thin metal films presented in Ref. [6], the schematic of a radiative MIM SP wave, which decays along the propagation direction $+z$ axis with an exponentially increasing field in a plane normal to the surface, is shown in Fig. 3.6. For any plane $x < 0$ where leakage occurs, the leaky wave radiates

at angle θ into the outermost medium and the field amplitude in the outermost media grows exponentially for only a finite distance x , which is a function of z and θ [6]. The leaky wave may be interpreted to have the characteristics of spatial transients [20]. This interpretation requires the wave-front tilt, θ , away from parallel to the MIM structure satisfying the following condition [6]

$$\tan(\theta) = \text{Re}\{k_x\} \text{Im}\{k_x\} = \text{Re}\{k_z\} \text{Im}\{k_z\} \quad (3.2)$$

where $k_z = k'_z + ik''_z$ is the longitudinal propagation constant, $k_x = \sqrt{k_z^2 - n^2 k_0^2} = k'_x + ik''_x$ is the complex transverse propagation constant in the outermost media, n denotes the refractive index of the outermost media where the leaky wave exists (for current case $n=1$), and k_0 is the free space wave number.

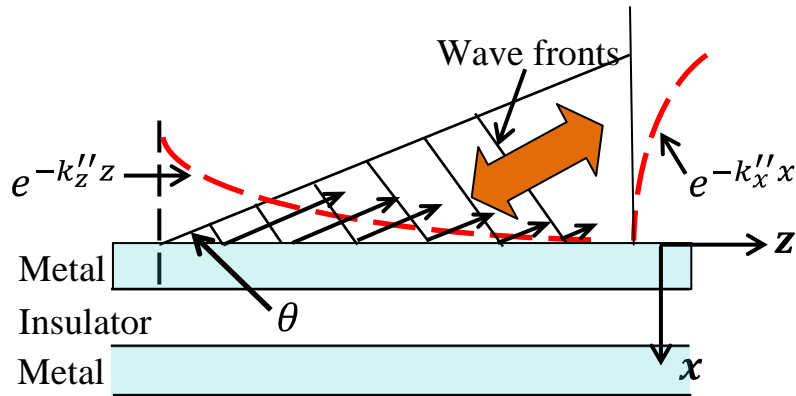


Fig. 3.6 Schematic of a radiative MIM SP wave which exponentially decays along the $+z$ axis with an exponentially growing field along the $-x$ axis. Only one side radiation in $x < 0$ is shown here.

To find the radiated power, the exponentially increasing local field is replaced by an effective appropriately phased equivalent current sheet [6]. The angular dependence of the radiated power is expressed as:

$$|P(\theta)|^2 = \frac{\sin^2(\theta)}{(k'_z - nk_0 \cos(\theta))^2 + (k''_z)^2} \quad (3.3)$$

For this mode, there is a well-defined peak in $|P(\theta)|^2$ at $\theta = \cos^{-1}(k'_z/nk_0)$, with an angular spread proportional to k''_z . The actual radiation pattern as a function of insulator and metal thickness are plotted in Fig. 3.7(b).

As shown in Fig. 3.7(a), the radiation angle increases with increasing wavelength until becoming perpendicular to the waveguide interface. The antenna region, always occurring at shorter wavelengths relative to the reactive region, shifts to longer wavelength with smaller peak radiation tilt as insulator thickness increases. Both the insulator and metal thickness have an influence on the antenna mode's well-defined radiation pattern, but practical considerations suggest that better control over the radiation pattern is achieved by varying insulator thickness. Narrower radiation lobes are found for thicker metal films. This variation of radiation angle with wavelength and insulator thickness can be understood in terms of the real part of the propagation constant (k'_z) and the imaginary part of the transverse wave vector (k''_z) in the free space regions bounding the waveguide. Increasing wavelength and decreasing insulator thickness both result in a decrease in k'_z , implying an increase of k''_z and leading to an increase in radiation angle.

Numerical modeling of one-sided Au-SiO₂-Au (30 nm/190 nm/semi-infinite) MIM leaky structures shows the presence of the antenna mode in the near-infrared at about 750 to 825 nm.

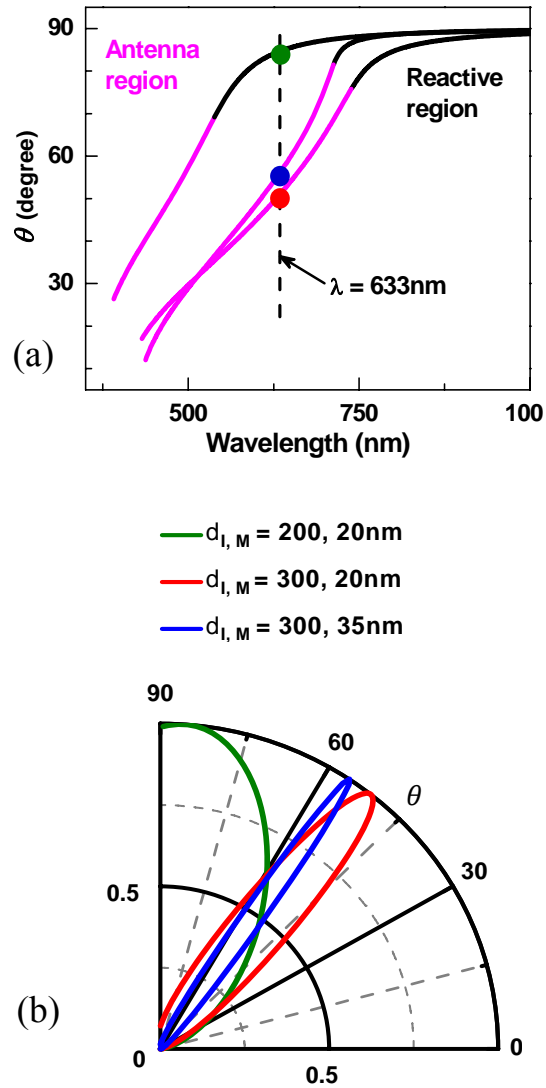


Fig. 3.7 MIM leaky wave-front tilt θ (a) and radiation free-space coupling pattern at a free-space wavelength of 633nm (b) as a function of insulator and metal thickness ($d_{I,M}$). In (a), the transition from purple to black in the plot curves occurs at the wavelength where the MIM waveguide modal propagation constant has equal real and imaginary values.

3.4 Spatial Dispersion Effects on MIM SPPs

As is known in solid state physics, the dielectric permittivity is not only a function of frequency, but also a function of wave-vector. Spatial dispersion, also known as non-local permittivity, is the dependence of the dielectric permittivity tensor on the wave-vector. Until now, all former results for SPPs, derived either for single metal-dielectric interface, IMI waveguide, or an infinite or finite MIM waveguide structures, are derived using local, bulk dielectric functions which only possess temporal dispersion and neglecting any effects of spatial dispersion. In principle, only an infinitely extended (“bulk”) medium is spatially homogeneous. When optical wave-vectors are comparable to optical media characteristic lengths (e.g., lattice spacing, electron mean-free path, and Debye radius, etc), non-local effects such as spatial dispersion, surface scattering and anomalous skin effect need to be considered. These nonlocal effects cause decreases in propagation length and wave vector for infinite MIM structure [21]. Spatial dispersion results in a suppression of the bend-back branch above ω_{sp} (i.e. the transition mode in Fig. 2.9(b)) [22].

In the case of finite MIM structures, as is shown in Chapter 3.3.1, the S_L mode possesses the largest wave-vector among four MIM SPP modes and increases with decreasing insulator-metal thickness. When it becomes so large that the plasmonic wavelength reduces to comparable or below the mean free path or layer geometric sizes, the above mentioned non-local effects will affect its propagation characteristics.

In this section, a bulk metal dielectric function $\varepsilon(\omega, \mathbf{k})$, possessing both the temporal and spatial dispersion, is used for deriving the MIM dispersion relations. Other non-local effects are not included. In the following numerical simulation, the spatial

dispersion effects on dispersion, propagation loss and confinement factor of the S_L mode of MIM structure with a thin core layer at large wave vectors are examined.

For simplicity, a Ag-air-Ag MIM in vacuum is considered. The two metal layers are both 20 nm thick. Following equation (E.37) (See Appendix E.4.3), the dielectric permittivity of Ag taking account of spatial dispersion effect is given by

$$\varepsilon(\omega, k) = \varepsilon_\infty - \frac{\omega_p^2}{\omega(\omega + i\gamma) - 3k^2 v_F^2/5} \quad (3.4)$$

where $\varepsilon_\infty = 5$, $\omega_p = 2\pi \cdot 2.175 \times 10^{15}$ Hz, $\gamma = 4.35 \times 10^{12}$ Hz [23], and $v_F = 1.40 \times 10^6$ m/s [24].

When spatial dispersion is taken into account, finding the mode solution turns out to be a self-consistent problem. The self-consistent results are once again obtained with Newton-Ralphson method.

The comparison of TM dispersion relation, propagation loss and confinement factor for S_L mode between using dielectric constant without (dashed lines) and with (solid lines) spatial dispersion are illustrated in Fig. 3.8. The results are simulated for core layer thickness of 2 nm (blue lines) and 5 nm (red lines).

It is observed that the spatial dispersion effect yields a reduced wave-vector in dispersion curve, an increased propagation loss and confinement factor comparing to those using bulk dielectric permittivity without wave-vector dependence. The increase of confinement factor is almost negligible. Beyond wavelength 500 nm, the differences in dispersion and propagation loss are also negligible.

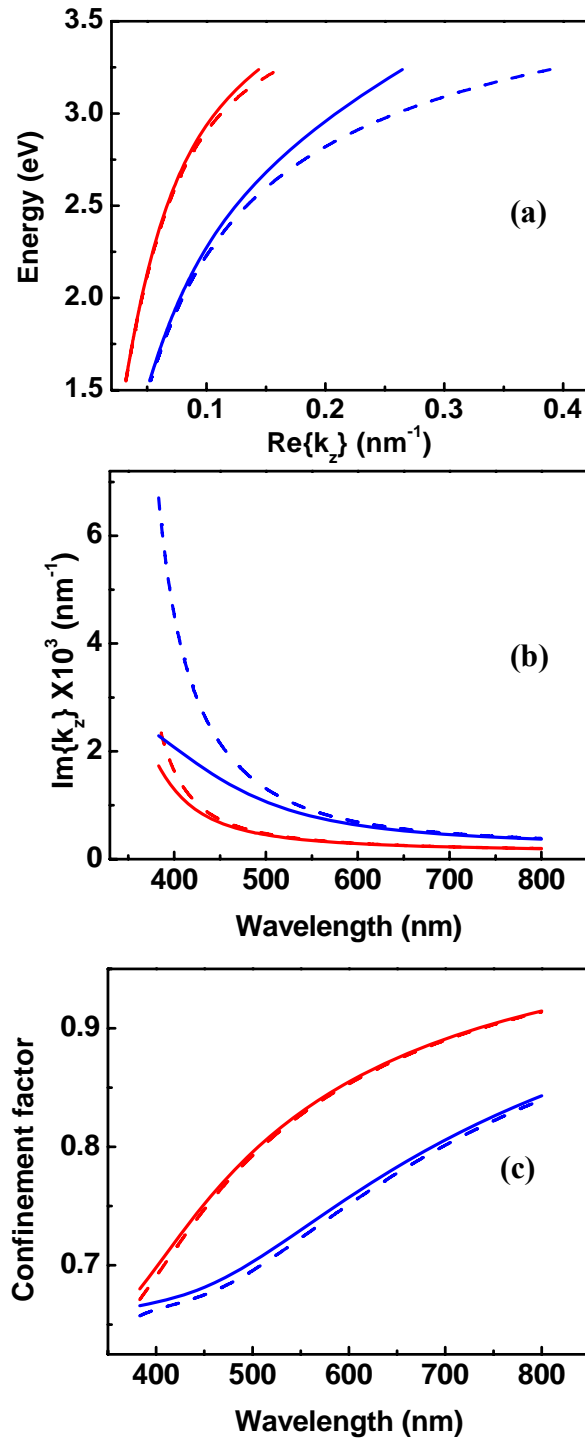


Fig. 3.8 TM dispersion relation (a), propagation loss (b) and confinement factor (c) for S_L mode by using dielectric constant without (dashed lines) and with (solid lines) spatial dispersion. The simulated Ag-air-Ag MIM structures in free space have the metal thickness of 20 nm and core layer thickness of 2 nm (blue lines) and 5 nm (red lines).

References

- [1] J. Chilwell and I. Hodgkinson, "Thin-films field-transfer matrix theory of planar multilayer waveguides and reflection from prism-loaded waveguides," *J. Opt. Soc. Am. A* **1**, 742 (1984).
- [2] E. Anemogiannis and E. N. Glytsis, "Multilayer waveguides: Efficient numerical analysis of general structures", *J. Light. Tech.* **10**, 1344 (1992).
- [3] E. Anemogiannis, E. N. Glytsis and T. K. Gaylord, "Determination of guided and leaky modes in lossless and lossy planar multilayer optical waveguides: Reflection pole method and wavevector density method," *J. Light. Tech.* **17**, 929 (1999).
- [4] J. Petráček and K. Singh, "Determination of leaky modes in planar multilayer waveguides," *IEEE Photon. Tech. Lett.* **14**, 810 (2002).
- [5] J. A. Dionne, L. A. Sweatlock, and H. A. Atwater, "Plasmon slot waveguides: Towards chip-scale propagation with subwavelength-scale localization," *Phys. Rev. B* **73**, 035407 (2006).
- [6] J. J. Burke and G. I. Stegeman, "Surface-polariton-like waves guided by thin, lossy metal films," *Phys. Rev. B* **33**, 5186 (1986).
- [7] R. Zia, M. D. Selker, P. B. Catrysse, and M. L. Brongersma, "Geometries and materials for subwavelength surface plasmon modes," *J. Opt. Soc. Am. A.* **21**, 2442 (2004).
- [8] F. Villa, T. Lopez-Rios, and L. E. Regalado, "Electromagnetic modes in metal-insulator-metal structures," *Phys. Rev. B* **63**, 165103 (2001).
- [9] E. N. Economou, "Surface plasmons in thin films," *Phys. Rev.* **182**, 539 (1969).
- [10] A. D. Rakić, A. B. Djurišić, J. M. Elazar, and M. L. Majewski, "Optical properties of metallic films for vertical-cavity optoelectronic devices," *Appl. Opt.* **37**, 5271 (1998).
- [11] J. A. Dionne, L. A. Sweatlock, H. A. Atwater, and A. Polman, "Planar metal plasmon waveguides: frequency-dependent dispersion, propagation, localization, and loss beyond the free electron model," *Phys. Rev. B* **72**, 075405 (2005).
- [12] G. W. Hanson and A. B. Yakovlev, "Investigation of mode interaction on planar dielectric waveguides with loss and gain," *Radio Sci.* **34**, 1349 (1999).

- [13] P. Berini, “Plasmon-polariton waves guided by thin lossy metal films of finite width: bound modes of asymmetric structures,” *Phys. Rev. B* **63**, 125417 (2001).
- [14] D. Marcuse, *Theory of Dielectric Optical Waveguides*, Academic Press, New York, (1974).
- [15] S. L. Lee, Y. Chung, L. A. Coldren, and N. Dagli, “On leaky mode approximations for modal expansion in multilayer open waveguides,” *IEEE J. Quantum Electron.* **31**, 1790 (1995).
- [16] A. W. Snyder and J. D. Love, *Optical Waveguide Theory*, London, Chapman and Hall, (1983).
- [17] C. Vassallo, *Optical Waveguide Concepts*, Elsevier, (1991).
- [18] P. Benech and D. Khalil, “Rigorous spectral analysis of leaky structures: Application to the prism coupling problem,” *Opt. Commun.* **118**, 220 (1995).
- [19] Y. D. Lin and J. W. Sheen, “Mode distinction and radiation-efficiency analysis of planar leaky-wave line source,” *IEEE Trans. Microwave Theory Tech.* **45**, 1672 (1997).
- [20] J. J. Burke and N. S. Kapany, *Optical Waveguides*, Academic, New York, (1972).
- [21] J. Conway dissertation, “Efficient Optical Coupling to the Nanoscale,” Electrical Engineering Department, University of California, Los Angeles (2006).
- [22] A. D. Boardman and P. Egan, “The influence of collisional damping on surface plasmon-polariton dispersion,” *J. Phys. Colloque* **45**, C5-179 (1984).
- [23] I. El-Kady, M. M. Sigalas, R. Biswas, K. M. Ho, and C. M. Soukoulis, “Metallic photonic crystals at optical wavelengths,” *Phys. Rev. B* **62**, 15299 (2000).
- [24] N. W. Ashcroft and N. D. Mermin, *Solid State Physics*, Saunders, (1976).

Chapter 4 Leaky Modes in Finite Planar Metal-Insulator-Metal

Plasmonic Waveguides

Surface plasmons may be either non-radiative (bound) or radiative (leaky). Non-radiative SPs possess larger wave momentum than that of light at the same frequency, prohibiting direct coupling to free-space. Radiative SPs have smaller wave momentum than that of light, allowing free-space coupling without use of a prism, grating coupler or scattering center.

Previous works on leaky SPs primarily focused on metallic slab and strip waveguides [1-5]. There is a growing interest in the radiative SPs of MIM structures [6-10]. In finite planar MIM structures, the TM dispersion relations, as shown in Fig. 3.1, are characterized by two mode pairs each labeled with L/H respectively. Labels L/H reflect the origin of the mode from the low/high energy branch of the single metal film SP. Due to mode splitting, a total of four non-degenerate SP modes are observed for two interacting metal films separated by a thin insulator layer[10]. In this section, finite MIM radiative (leaky) waves, i.e. the dispersion region of the highest energy MIM SP mode (labeled as A_H in Fig. 3.1) lying above the light line, are investigated theoretically and experimentally. Theoretically, the TM modal solutions of the planar MIM geometry are obtained numerically by using the transfer matrix formalism. Details have been described in Chapter 3.1. Experimentally, in Chapter 4.1 and 4.2, finite planar MIM waveguide leaky waves are investigated using the ATR Kretschmann configuration and free space coupling, respectively. For the ATR Kretschmann configuration, both single- and double-sided leaky waves are analyzed. The leaky wave dispersion relation and its antenna mode

radiation pattern are determined through both angle- and wavelength-dependent reflectance of free space incident light.

Two MIM structures, Au-MgF₂-Au (sample A, with thicknesses 32 nm-190 nm-32 nm, respectively) and Au-Al₂O₃-Au (sample B, with thicknesses 40 nm-190 nm-140 nm, respectively), were fabricated for ATR and free-space coupling experiments, respectively. For both samples, a thoroughly cleaned microscope glass slide substrate is first coated with a 0.5 nm thick chromium layer as an adhesive layer, followed by the required MIM layer material deposited sequentially by high vacuum ($<10^{-6}$ Torr) electron beam evaporation (Al₂O₃ needs extra O₂ gas during evaporation). The evaporation rate is controlled at $< 0.1 \text{ nm s}^{-1}$. The thickness and refractive indices of these two insulators were measured on a control sample by ellipsometry at 633 nm.

4.1 ATR Kretschmann Coupling

The ATR geometry in the Kretschmann configuration [See Fig. 2.14(a)] is widely used for the excitation of SPPs. It couples evanescent incident light to SPs by satisfying the surface plasmon resonance (SPR) condition via momentum matching. As shown in Fig. 2.15, this configuration allows excitation of leaky SPs modes (i.e. those between the air and prism light lines) [2] while can never excite purely bound modes (i.e. those to the right of the prism light line). The excited leaky SPs modes lose their energy through the metal inherent absorption as well as leakage radiation into the prism.

In the ATR Kretschmann configuration, the experiments may be performed in two distinct variations. One is to fix the excitation frequency and scan the angle of incidence; this is called the angular (or θ) scan. The other way is to scan excitation frequency with a

fixed angle of incidence; this is the frequency (or ω) scan. Here, the first one, scanning angle SPR was used. The excitation of SPs results in a sharp dip in the ATR angular reflectance curve which is caused by destructive interference between the leakage radiation and the reflected part of the excitation beam.

Sample A was mounted to a BK7 prism by index matching fluid. Symmetric (glass-Au-MgF₂-Au-glass) and asymmetric (air-Au-MgF₂-Au-glass) MIM geometries were formed by mounting the top Au surface (as shown in Fig. 4.1 (a)) or the glass substrate (as shown in Fig. 4.1 (b)) to the ATR prism, respectively. The reflectance was measured with a TM-polarized laser beam at 633 nm.

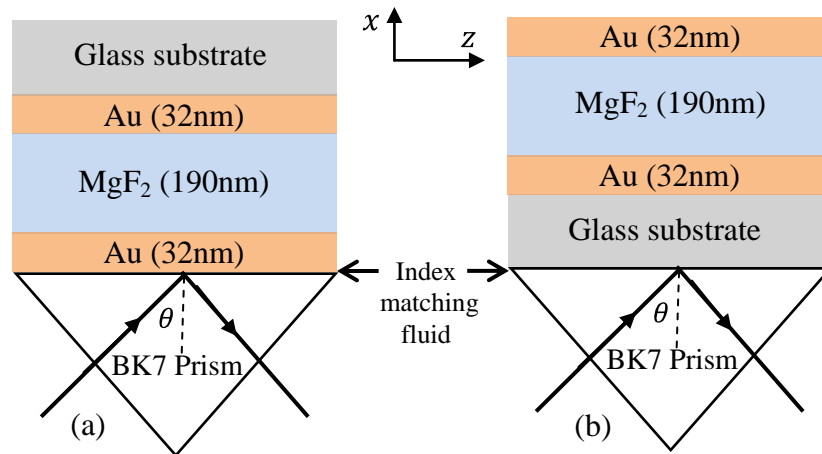


Fig. 4.1 Symmetric (a) and asymmetric (b) MIM ATR Kretschmann configurations.

The experimental and calculated angle-dependent ATR SPR curves for the symmetric and asymmetric MIM structures are plotted in Fig.4.2. The incidence angle associated with the minimum ATR reflectance is denoted as θ_0 . The calculated normalized Poynting vector fields (defined as Poynting vector \mathbf{S} divided by incident parallel energy flux- $S_{i//}$) are illustrated in Fig.4.3. The modeled results were calculated

with dielectric constants of $\epsilon_{Au} = -10.9824 + 1.3280i$, $\epsilon_{MgF_2} = 1.891$, and $\epsilon_{BK7} = 2.295$ at 633nm.

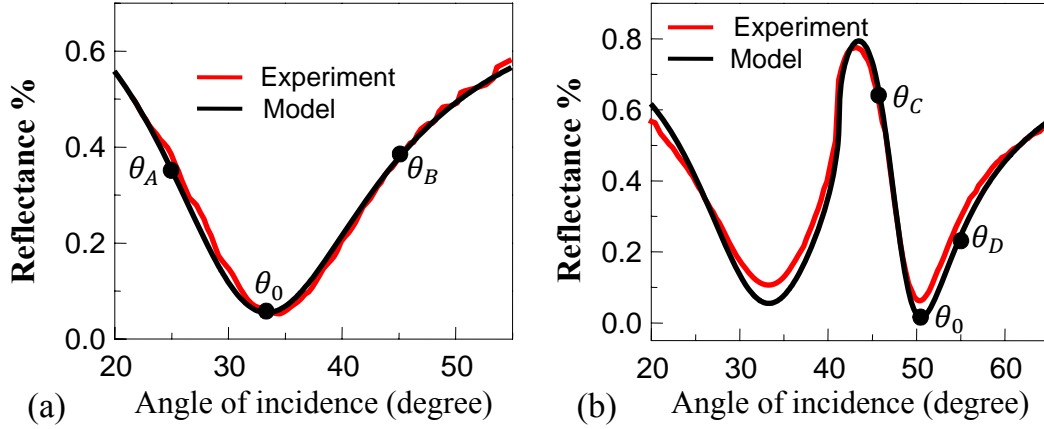


Fig. 4.2 ATR reflectance curves at 633nm for (a) symmetric glass-Au-MgF₂-Au-glass and (b) asymmetric air-Au-MgF₂-Au-glass MIM geometries. See the text for discussion of θ_0 , θ_A , θ_B , θ_C and θ_D .

Figure 4.2(a) shows the symmetric MIM structure has one resonance dip with $\theta_0 = 33.4^\circ$. This resonance condition corresponds to excitation of a double-sided leaky (DSL) mode in the MIM waveguide having an effective modal index smaller than that of glass. As plotted in Fig. 4.3(a), the incident power is coupled through the bottom prism-Au interface into the DSL mode and most of the internal energy flux is located at the interior Au-MgF₂ interfaces. A small amount of energy leaks out of the MIM structure through the top Au-glass substrate interface. The internal energy flux distribution is nearly symmetric at θ_0 . The energy flux localization shifts from the incident interior metal-insulator interface to the exiting interior metal-insulator interface with increasing angle of incidence.

Figure 4.2(b) shows the asymmetric MIM geometry has two resonance dips at $\theta_0 = 33.3^\circ$ and 50.5° . Modeling reveals that a DSL mode is excited at 33.3° . Its characteristics are similar to that of symmetric MIM DSL mode. The resonance condition at the larger incidence angle around 50.5° denotes the excitation of a single-sided leaky (SSL) SP mode with effective mode index larger than that of air but smaller than that of glass. Figure 4.3(b), as expected, shows this single (glass)-sided leaky SP mode has no energy flowing out of the waveguide through the top Au-Air interface. The peak energy flux localization shifts from the exiting exterior air-Au interface to the incident Au-MgF₂ interface with increasing angle of incidence. The amount of energy flux propagated on the incident Au-MgF₂ interface is larger than that on the exiting Au-MgF₂ interface throughout the resonance condition. The spatial uncertainty principle is expressed as

$$\Delta z \Delta P_z \geq \hbar/2 \quad (4.1)$$

We also get

$$\Delta P_z = \hbar \Delta k_z = \hbar \Delta(n_{BK7} k_0 \sin(\theta)) = \hbar n_{BK7} k_0 \cos(\theta) \Delta \theta \quad (4.2)$$

$$\Delta z = \frac{1}{2 \text{Im}\{k_z\}} \quad (4.3)$$

Combining (4.1), (4.2) and (4.3), the resonance full width of half maximum (FWHM) is given as

$$\Delta \theta_{FWHM} \geq 2 \text{Im}\{k_z\} / \{n_{BK7} k_0 \cos(\theta)\} \quad (4.4)$$

In above equations, k_z is the SPs mode longitudinal propagation constant, n_{BK7} is the refractive index of the prism, and k_0 is the vacuum wave vector. Therefore, the narrower resonance observed for the SSL mode compared to excitation of a DSL mode indicates smaller amount of loss.

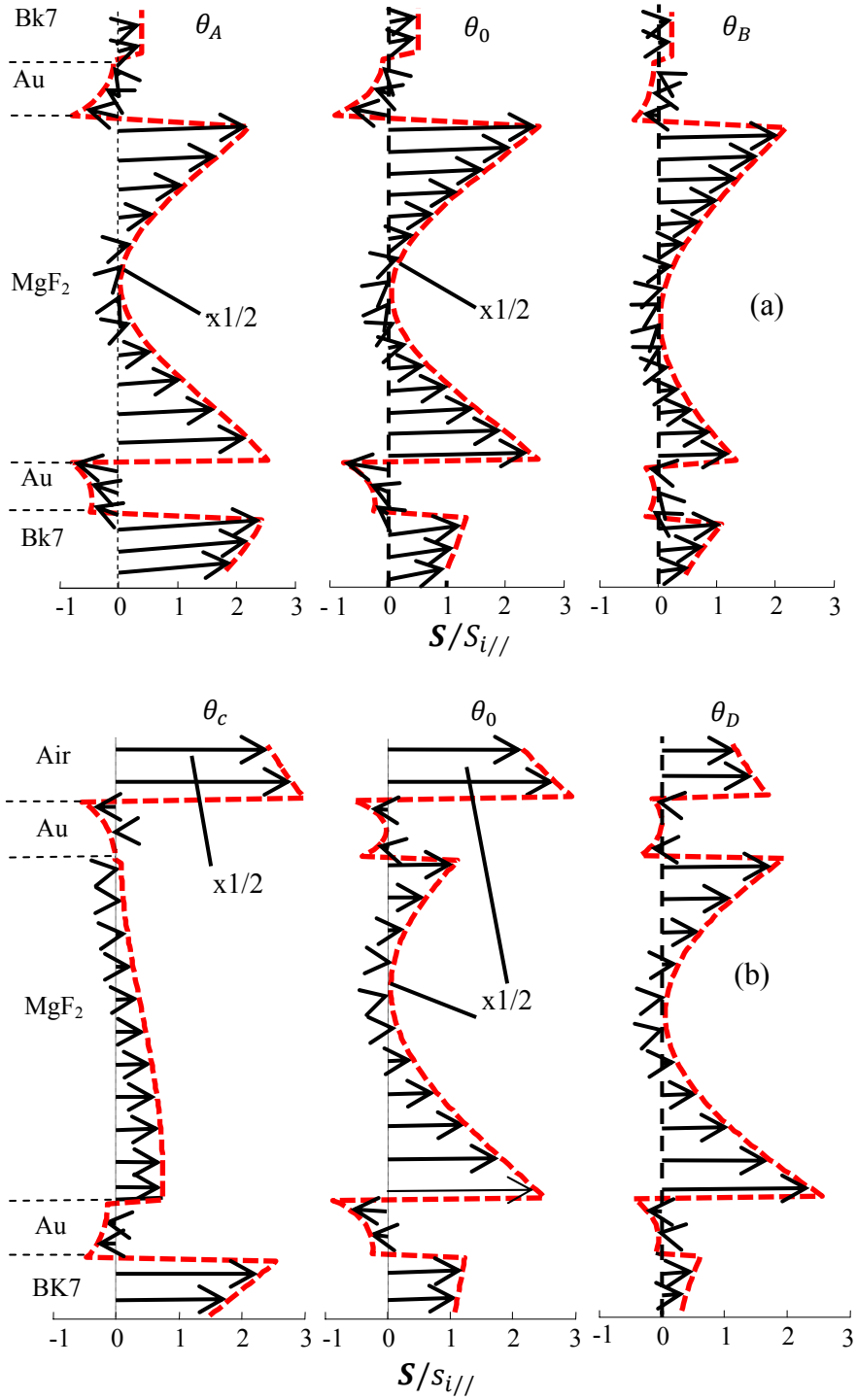


Fig. 4.3 Normalized Poynting vector fields of (a) symmetric and (b) asymmetric MIM geometries when on or off resonance. The angles θ_0 , θ_A , θ_B , θ_c and θ_D are the same as those shown in Fig. 4.2.

Note that for both symmetric and asymmetric DSL modes as well as for the asymmetric SSL mode, enhancement of the incident energy flux occurs at the interior metal-insulator interfaces when on resonance.

A closer examination of mode coupling reveal distinct differences between the experimental minimum, θ_0 , the plasmon phase matching condition defined by the dispersion curve of Fig. 3.1, θ_p , and the angle where maximum energy flux is carried in the insulator layer, θ_R . The ATR angle θ_0 occurs for maximal loss, which is composed of metal material absorption loss and leakage radiation loss. Careful numerical evaluation reveals that θ_0 , θ_p and θ_R of MIM structure are slightly different. For the examples studied here, the symmetric and asymmetric DSL modes have $\theta_R < \theta_0 < \theta_p$, ($32^\circ < 33.4^\circ < 34.9^\circ$) while the asymmetric SSL mode has $\theta_p < \theta_R < \theta_0$, ($48.3^\circ < 50^\circ < 50.5^\circ$). Therefore, the incidence angle needs to be carefully determined to optimize mode coupling.

4.2 Free Space Coupling

External incident light can also directly couple to the MIM leaky-mode SPs. The angle-dependent reflectance of a TM-polarized free-space incidence beam on top surface of sample B is shown in Fig. 4.4(a). The reflectance was recorded with a Fourier-transform infrared (FTIR) spectrometer with respect to a gold mirror. For sample B, the leaky wave only exists on top side owing to the optically thick bottom gold film. The calculated and experimental dispersion relations $\omega(k_{//})$ are plotted in Fig. 4.4(b). The experimental results, derived from the position of the reflectance minima at each incident angle, agree with the dispersion curve calculated using the transfer matrix method, reported dispersive Au dielectric constant [11] and a dielectric constant for Al_2O_3 of 2.56

as measured by ellipsometry. Coupling from free space in the energy range of 1.6 to 1.8 eV has been observed for this MIM structure.

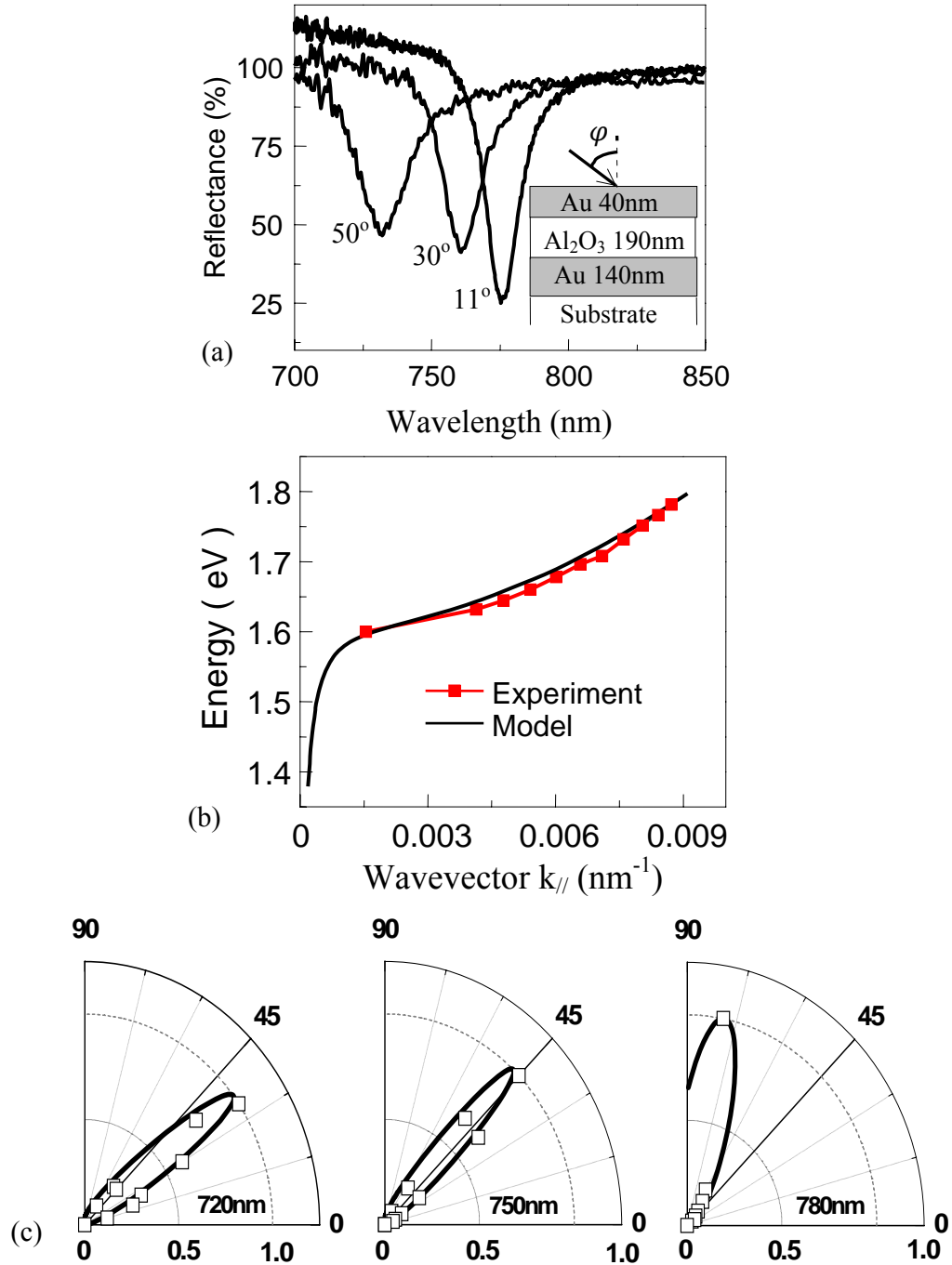


Fig. 4.4 (a) Experimental TM reflectance for the Au-Al₂O₃-Au MIM structure. (b) The dispersion curves for the radiative SPs of sample B. (c) Radiation patterns (left to right) of the radiative SP at 720, 750 and 780nm.

The radiation pattern for the radiated or coupled leaky wave power in sample B is illustrated in Fig. 4.4(c) at wavelengths 720 nm, 750 nm and 780 nm. The theoretical calculation follows the relation [3]

$$|P(\theta)|^2 = \frac{\sin^2 \theta}{(k'_z - nk_0 \cos \theta)^2 + (k''_z)^2} \quad (4.5)$$

where $k_z = k'_z + ik''_z$ is the longitudinal complex propagation constant, k_0 is the free space wave vector, n denotes refractive index of the outermost media where the leaky wave exists, and $\theta = 90^\circ - \varphi$ is the leaky wave-front tilt relative to the surface and defined as

$$\tan \theta = k''_x / k'_z = k''_z / k'_x \quad (4.6)$$

with the complex transverse propagation constant in the media where leaky wave exists

$k_x = \sqrt{k_z^2 - n^2 k_0^2} = k'_x + ik''_x$. A well-defined radiation peak is observed at tilt angle at $\theta = \cos^{-1}(k'_z / nk_0)$ with an angular breadth proportional to k''_z .

For leaky modes, any light energy coupled into SPs is re-radiated. The experimental radiation patterns are derived from FTIR reflectance spectra by measuring the angle-dependence of the resonance dip. The maximum value is normalized to one.

Adopting concepts from microwave technology, leaky waves can be divided into two distinct regions: an antenna mode region defined by $k'_z > k''_z$ and characterized by the propagation of mode energy out of the waveguide, and a reactive mode region defined by $k'_z < k''_z$ [10, 12]. Modal analysis of sample B predicts the transition where $k'_z = k''_z$ to occur around 774 nm.

As shown in Fig.4.4(c), the antenna region occurring at shorter wavelengths than the reactive region, has a smaller peak radiation angle relative to the surface. The

radiation angle increases with increasing wavelength due to a monochromatically decreasing k_z' and increasing k_z'' .

The transition from antenna to reactive leaky modes is experimentally associated with an end to the shift of the resonance dip, since as the reactive mode dominates, coupling from free space is significantly reduced. The result is that the near normal incidence reflectance shows a dip associated with the strong coupling of the residual antenna mode radiation pattern instead of the reactive mode suggested by the dispersion curve. Modeled normal incidence reflectance predicts a resonance dip around 775 nm, while the dispersion relation shows the mode for zero k_z considerably longer than 850 nm. This is indicative of the weak free-space coupling in the leaky wave reactive region.

The antenna leaky mode radiation angle is steerable by varying the insulator and metal thicknesses [10]. This suggests that MIM plasmonic waveguides with active insulator layers have potential applications in beam steering devices.

References

- [1] R. Vincent and J. Silcox, "Dispersion of radiative surface plasmons in aluminum films by electron scattering," *Phys. Rev. Lett.* **31**, 1487 (1973).
- [2] W. P. Chen, G. Ritchie, and E. Burstein, "Excitation of surface electromagnetic waves in attenuated total-reflection prism configurations," *Phys. Rev. Lett.* **37**, 993 (1976).
- [3] J. J. Burke and G. I. Stegeman, "Surface-polariton-like waves guided by thin, lossy metal films," *Phys. Rev. B* **33**, 5186 (1986).
- [4] R. Zia, M. D. Selker, and M. L. Brongersma, "Leaky and bound modes of surface plasmon waveguides," *Phys. Rev. B* **71**, 165431 (2005).
- [5] R. Zia, J. A. Schuller, and M. L. Brongersma, "Near-field characterization of guided polariton propagation and cutoff in surface plasmon waveguides," *Phys. Rev. B* **74**, 165415 (2006).
- [6] G. J. Kovacs and G. D. Scott, "Optical excitation of surface plasma waves in layered media," *Phys. Rev. B* **16**, 1297 (1977).
- [7] H. Shin, M. F. Yanik, S. Fan, R. Zia, and M. L. Brongersma, "Omnidirectional resonance in a metal-dielectric-metal geometry," *Appl. Phys. Lett.* **84**, 4421 (2004).
- [8] J. S. Q. Liu and M. L. Brongersma, "Omnidirectional light emission via surface plasmon polaritons," *Appl. Phys. Lett.* **90**, 091116 (2007).
- [9] J. Feng, T. Okamoto, J. Simonen, and S. Kawata, "Color-tunable electroluminescence from white organic light-emitting devices through coupling surface plasmons," *Appl. Phys. Lett.* **90**, 081106 (2007).
- [10] J. Chen, G. A. Smolyakov, S. R. J. Brueck, and K. J. Malloy, "Surface plasmon modes of finite, planar, metal-insulator-metal plasmonic waveguides," *Opt. Express* **16**, 14902 (2008).
- [11] L. G. Shulz, "The optical constants of silver, gold, copper, and aluminum. I. the absorption coefficient k ," *J. Opt. Soc. Am.* **44**, 357 (1954).
- [12] Y. D. Lin and J. W. Sheen, "Mode distinction and radiation-efficiency analysis of planar leaky-wave line source," *IEEE Trans. Microwave Theory Tech.* **45**, 1672 (1997).

Chapter 5 Gain-Assisted Propagation of SPPs in Finite MIM Plasmonic Waveguides

Surface plasmons have been widely exploited in photonic and optoelectronic devices. However many applications of surface plasmons suffer from the losses resulting from energy damping in metals. For example, the metal energy dissipation process limits SPPs typical effective propagation lengths to values in the micrometer to millimeter range. Active plasmonics, which describes the interaction between an active or gain medium and surface plasmons, could be one way of eliminating losses in plasmonic devices to enable their numerous potential applications [1-22]. Compensating losses by inclusion of gain could be achieved by spin coating a solution of laser dye molecules or π -conjugated polymers on top of the structures, or applying semiconductor nanocrystals, all for use as a gain material.

Influence of a gain medium on SPPs has been receiving recent attention. At early stage, gain-assisted propagation of SPPs on planar metal waveguides has been investigated using Fresnel reflection coefficients. Enhanced TIR structure consisting of a gain medium in contact with a thin silver film is resulted from the increased effective gain of the amplifying medium mediated by the excited surface plasmon on metal surface [23]. It is shown that for any value of gain above threshold there exists a metal thickness for which a reflection singularity exists. This work has been extended to study surface EM waves propagation on the interface between a metal and gain medium for transversally bound and unbound excitation laser beams. The possibility of creating a surface plasmon based laser has been pointed out [24]. Recent studies have focused extensively on transferring energy from gain material to propagating SPPs [25-31] and to

localized SPPs in metal nanostructures [32-34] by using stimulated emission. The gain media surrounding the metal, including quantum cascade (QC) active material [25, 26], quantum well heterostructures [27, 30], quantum dot [32] and dye molecules [29, 31, 34], provide the energy to compensate for the SPP loss.

In this section, the inclusion of a dye-doped polymer into realistic finite MIM structures is modeled.

5.1 Numerical Method and Validation with Gain Inclusion

Throughout the dissertation, the phase factor is assumed in the form of $\exp[-i\omega t + ik_z z]$ with $k_z = k'_z + ik''_z$ (here we take the wave propagates along the +z axis), thus loss and gain in media is handled by setting the imaginary part of the dielectric constant to be positive and negative, respectively.

By introducing negative imaginary part of dielectric constant, the transfer matrix formalism with a Newton-Raphson root searching algorithm in the complex wavevector plane are used to obtain the TM modal solutions of the finite planar MIM geometry in the presence of gain. The details of this numerical method have been described in Chapter 3.1 and appendix C and D. The classical Fresnel formalism for reflection is used to investigate gain-assisted propagation of SPPs in MIM waveguides in the ATR configuration. The incorporation of finite thick gain medium is treated as above by setting dielectric constant imaginary part to be negative. However, using this formalism in the presence of an infinitely thick gain material requires additional attention when incident angles are beyond the critical angle. It will be explained in the following part.

Let us start with a simple case considering reflection of a plane wave at a planar interface between two half-spaced isotropic media. The geometry and coordinates are shown in Fig. 5.1. These two media have relative permittivities ϵ_1 and $\epsilon_2 = \epsilon_2' + i\epsilon_2''$, respectively, and $\epsilon_1 > \epsilon_2'$.

The medium 2, labeled with dielectric constant ϵ_2 , can be either lossless ($\epsilon_2'' = 0$), lossy ($\epsilon_2'' > 0$) or active ($\epsilon_2'' < 0$). Its complex refractive index is expressed as $n_2 = n_2' + in_2''$, then we get $\epsilon_2 = \epsilon_2' + i\epsilon_2'' = (n_2' + in_2'')^2 = (n_2')^2 - (n_2'')^2 + i2n_2'n_2''$. Since the power of the EM field propagating along the z-direction is proportion to $\exp[i2(n_2' + in_2'')k_0z]$, where k_0 is the free-space wave vector, thus the real part of the exponent defines the wave attenuation or growth, therefore, the absorption (gain) coefficient is defined as

$$\gamma = 2n_2''k_0 = \frac{\epsilon_2''k_0}{n_2'} \quad (5.1)$$

with $n_2'' = \epsilon_2''/2n_2'$. In the numerical results presented later, gain coefficient, instead of dielectric constant imaginary part, is used.

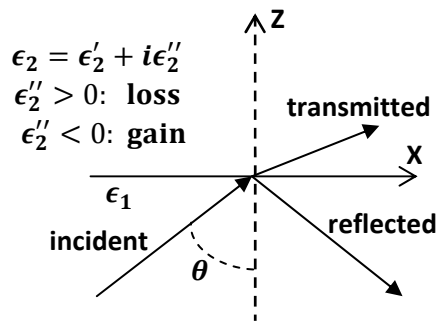


Fig. 5.1 The geometry and coordinates of the reflection of a plane wave on a planar interface between two different media.

When light is incident from a medium of higher refractive index onto a medium of lower refractive index, the TIR occurs at incident angles θ greater than or equal to the critical angle θ_c . When TIR occurs, for lossless media case the incident beam is completely reflected with no attenuation. The reflection of a incident light beam by a lower-index medium, either active (any isotropic optically active gain medium, such as optically pumped dye solutions or inverted atomic systems, and etc.) or absorptive (any isotropic loss medium), has been studied often owing to its interesting physics as well as wide applications[23, 31, 35-47]. At incident angles below the critical angle ($\theta < \theta_c$), there is a real propagating electromagnetic field inside the lower-index media with either gain or loss, and the energy flux across the interface for a plane wave incident on an active medium is the same as that of a plane wave incident on a conjugate absorptive media [47]. At incident angles beyond the critical angle ($\theta > \theta_c$), attenuated total internal reflection (ATIR), where the reflectivity is less than unity and the transmitted beam propagates inhomogeneously with attenuation [48], occurs with a lower-index absorptive medium, and in contrast, enhanced total internal reflection effect (ETIR), where the reflected beam is more intense compared to the incident beam, occurs with a lower-index active medium [47]. ETIR is caused by the fact that the electromagnetic field excited in the active medium has to propagate back toward the interface with gain to be a physical wave.

Our implementation of Fresnel formalism with either finite or infinite thick gain medium incorporation has been validated against previously published results [23, 24, 47]. The duplicated results from Ref. [23] are plotted in Fig. 5.2. The gain parameter α is

defined as $\alpha = (\epsilon_3''/\epsilon_2'')(\epsilon_2'/\epsilon_3')^2$, where ϵ_i'' ($i = 1, 2, 3$) is the imaginary part of the material dielectric constant.

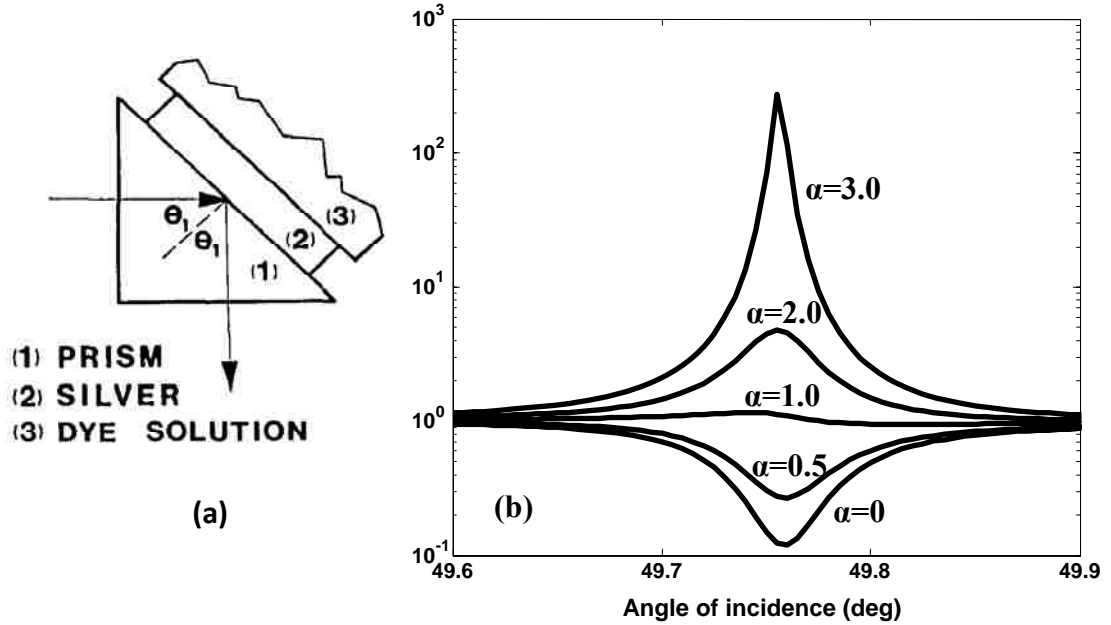


Fig. 5.2 (a): Geometry for enhanced reflectance using SP excitation. Thickness of gain medium is assumed to be infinite. (b): Reflectance vs angle of incidence near surface plasmon angle for several values of the gain parameter α .

5.2 Mode Analysis of Gain-Assisted Symmetric Finite MIM Plasmonic

Waveguides

The influence of the gain medium on the four SP modes within finite MIM waveguides is discussed here. This section will examine the feasibility of realistic lossless propagation of SPPs in MIM geometry with active medium incorporation and also provide optimum MIM design for gain-assisted MIM SPPs propagation in the ATR geometry.

For simplicity, only the symmetric finite planar MIM plasmonic waveguide with a core material exhibiting optical gain is considered. Two metals, silver and gold, are commonly used in plasmonic applications. Silver has a smaller absorption loss and gold has more stable optical and chemical properties. For the symmetric MIM structure, the lower the refraction index of the dielectric, the lower the waveguide modal loss. Therefore, an MIM structure, which is composed of silver with low-index passive and active dielectric materials constructed with a silver-compatible fabrication process steps is preferred. Given these considerations, a proposed realistic symmetric MIM structure depicted in Fig. 5.3.

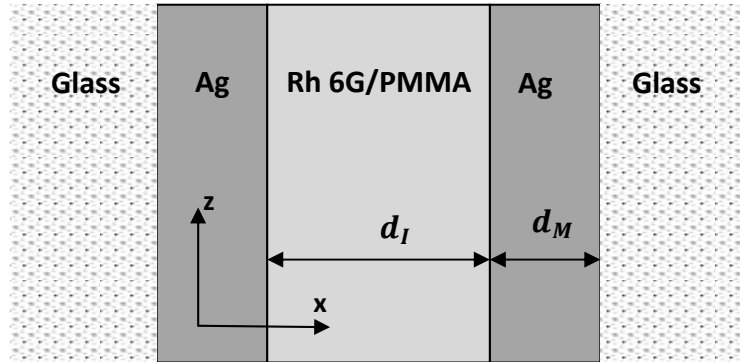


Fig. 5.3 Schematic of a symmetric glass-silver-Rh6G/PMMA-silver-glass planar MIM structure. The silver and Rh6G/PMMA thickness are labeled as d_M , d_I , respectively.

The active layer, Rhodamine 590 (Rhodamine 6G, or Rh6G in short) doped Polymethyl- methacrylate (PMMA), is sandwiched between two thin silver films and this MIM structure is embedded in glasses. Rhodamine 6G, one of the best known laser dyes, has been frequently used in solid-state dye lasers. PMMA, the most frequently used

polymer host for dye molecule, has refractive index ~ 1.5 which is close to that of silica glass, and shows the best optical transparency in the visible spectral range.

The dielectric constant of silver follows the empirical data fitted Lorentz-Drude model described in Chapter 2.3. The active core Rh6G/PMMA layer, formed from Rhodamine 6G doped PMMA anisole solution, has refractive index about 1.46 [49], which is close that of glass. It exhibits optical gain at wavelength $\lambda = 594\text{nm}$.

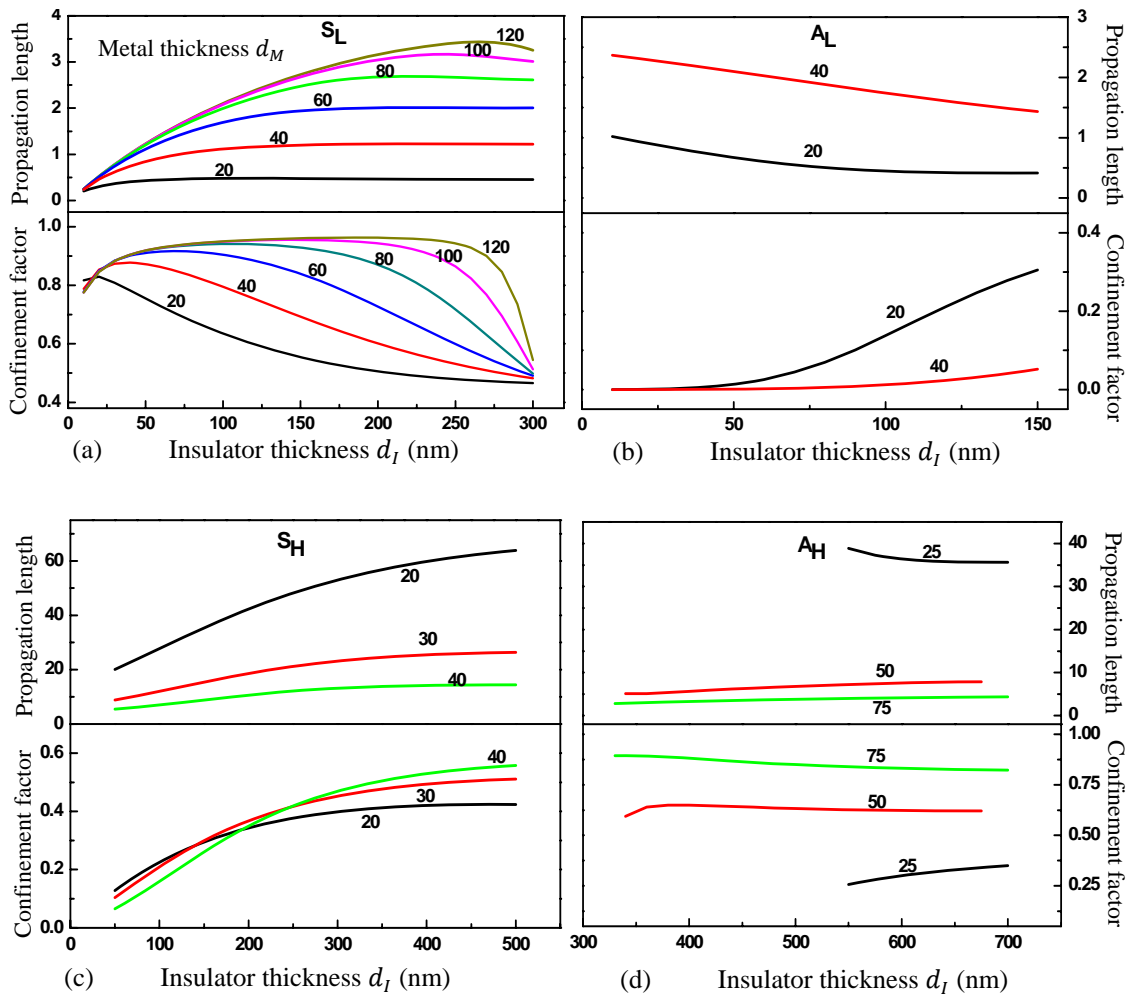


Fig. 5.4 Propagation length and confinement factor of SP modes in a symmetric glass-silver-Rh6G/PMMA-silver-glass planar MIM structure at free-space wavelength 594 nm as a function of metal (d_M) and insulator (d_I) thickness.

Figure 5.4 illustrates the evolution of the propagation length L and confinement factor Γ of the coupled SP modes of the MIM waveguide, depicted in Fig. 5.3, as a function of metal and insulator thickness. The subplot (d) is plotted for the bound portion of A_H mode. The behaviors of L and Γ of the SP modes in this realistic symmetric MIM waveguides as a function of metal and insulator thickness are similar to that summarized in Fig. 3.5, and will not be discussed further. It is observed, as expected, that mode S_H (A_L) offers the best (worst) opportunity for using the gain materials to fully compensate for the MIM waveguide losses.

For each of the four MIM SP modes, there exists an optimized structure design to minimize its modal loss while at the same time maintain acceptable mode confinement, and thus consequently minimize the required gain value to enable a reduced-loss or even lossless MIM plasmonic waveguides. The respective optimum MIM structures for S_L , S_H and A_H modes are determined from Fig. 5.4 and listed in Table 5.1. These optimum MIM structures will be investigated to figure out whether the minimum required gain value for MIM lossless propagation lying in the realistic gain range of Rh6G/PMMA.

Table 5.1 Optimum symmetric glass-Ag-Rh6G/PMMA-Ag-glass MIM structure

MIM SP modes	Ag-Rh6G/PMMA-Ag thickness (nm)
S_L	120 - 250 - 120
S_H	20 - 500 - 20
A_H	25 - 600 - 25

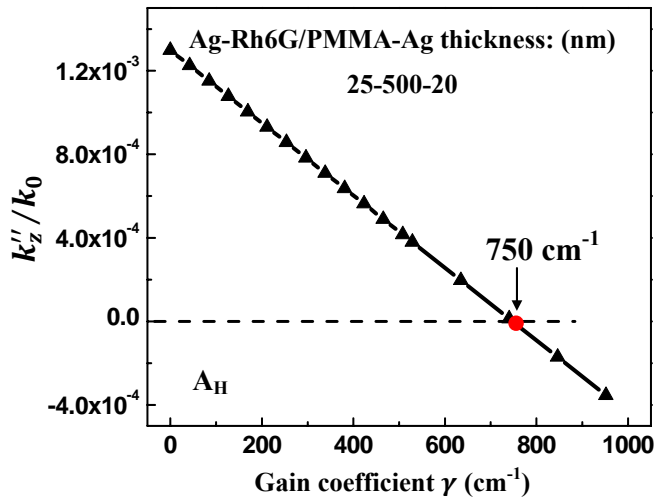
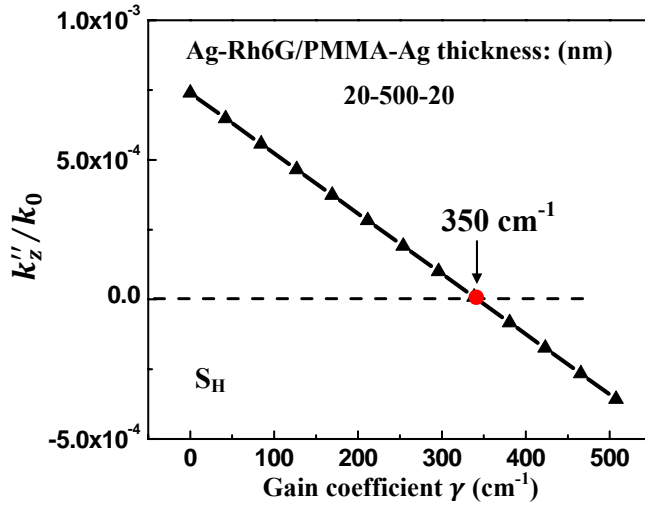
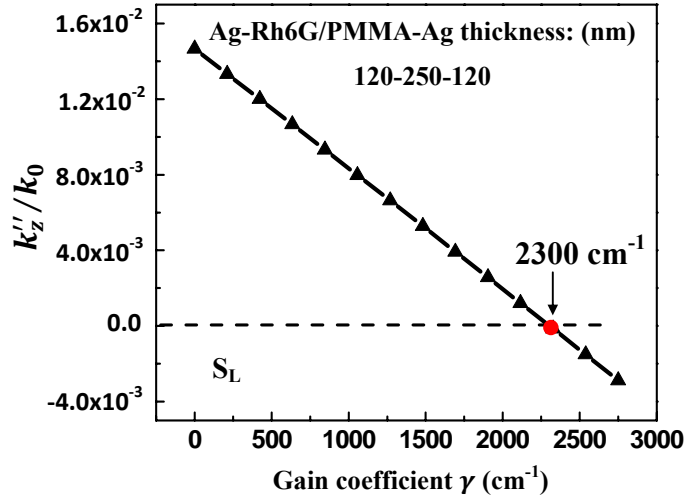


Fig. 5.5 The normalized propagation constant imaginary part v.s. Rh6G/PMMA gain coefficient. The red dots label gain coefficient value where $k_z'' = 0$.

Figure 5.5 shows the evolution of the imaginary part of the normalized propagation constant, k_z''/k_0 (k_0 is free-space wave number), as a function of the active core, Rh6G/PMMA, gain coefficient. The gain coefficient is defined in equation (5.1). The red dots label the critical gain coefficient values that make $k_z'' = 0$, corresponding to the lossless propagation. Given the optimum MIM structures listed in Table 5.1, the lossless propagation of MIM SP mode S_L , S_H and A_H are achieved with core gain coefficient γ around 2300 cm^{-1} , 350 cm^{-1} and 750 cm^{-1} , respectively. The critical gain coefficient of 350 cm^{-1} for lossless propagation of mode S_H is below the literature available gain coefficient of 420 cm^{-1} for Rh6G/PMMA [31]. For mode S_H in the optimized glass-MIM-glass structure, i.e. Ag-Rh6G/PMMA-Ag with thickness of 20 nm-500 nm - 20 nm, respectively, when the core gain coefficient $\gamma > 350 \text{ cm}^{-1}$, the amplitude of the propagating S_H mode will keep increasing (corresponding to negative k_z'') till reaching the limitation posed by gain saturation.

Numerical results (data not shown) show that the influence of reasonable gain coefficients γ in the active core material on both the real part of the propagation constant k_z' and the confinement factor are negligible. Note that for each MIM SP mode, the effect of gain-induced loss compensation effect depends on the location of the active medium. Numerical results (data not shown) also verify that more effective loss compensation occurs when the gain media are co-located with field maxima. Therefore, for the symmetric MIM structure, an active core layer is preferred for compensating propagation loss in the S_L and A_H modes while placing the gain in the bounding media is more effective for the S_H and A_L modes.

The propagation lengths of MIM S_H mode without gain (black dash lines) and with reported Rh6G/PMMA gain coefficient of 420cm^{-1} (red solid lines) are plotted in Fig 5.6. For mode S_H , as core thickness increase, the modal loss decreases and thus the critical gain for lossless propagation decreases. The sharp increase in propagation length of mode S_H is observed for MIM structure with thickness $20\text{nm}-320\text{nm}-20\text{nm}$ where the critical gain value for lossless propagation is reduced to approach 420 cm^{-1} . Given a realistic Rh6G/PMMA gain coefficient of 420 cm^{-1} , the amplitude of the propagating S_H mode for MIM structure with Ag films both 20nm thick and core material Rh6G/PMMA thicker than 320nm will keep increasing (corresponding to negative k_z'') till reaching the limitation posed by gain saturation. With the literature reported Rh6G/PMMA gain coefficient of 420 cm^{-1} , the maximum attainable propagation length for mode A_H is around $100\mu\text{m}$ and for mode S_L and A_L less than $10\mu\text{m}$.

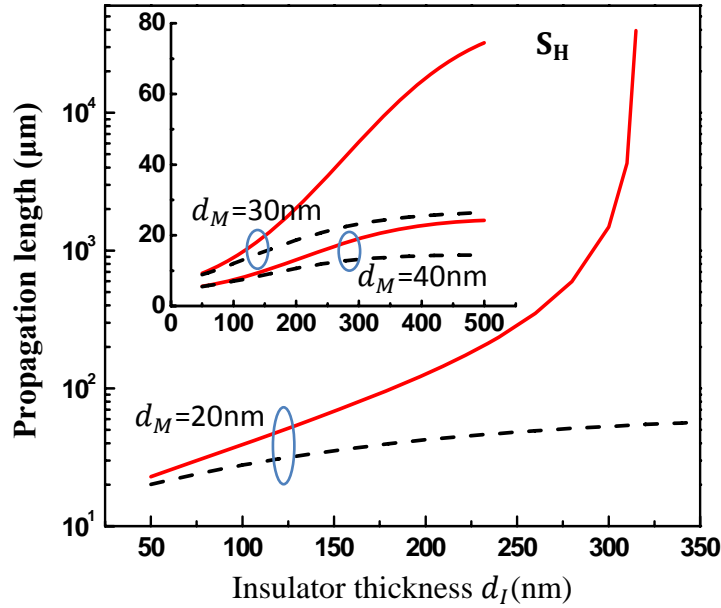


Fig. 5.6 Propagation length of S_H mode versus metal (d_M) and insulator (d_I) thickness at free-space wavelength 594 nm for a symmetric glass-silver-Rh6G/PMMA-silver-glass planar MIM structure with zero core gain (black dash lines) and core gain coefficient $\gamma = 420 \text{ cm}^{-1}$ (red solid lines).

5.3 Gain-Assisted Finite MIM SPPs Propagation in ATR Geometry

In this section, SPPs propagating in MIM waveguides with adjacent gain media in the ATR geometry, as sketched in Fig. 5.7, is studied. The MIM waveguide consists of Ag-PMMA-Ag with thickness of 20nm-500nm-20nm, respectively. An extra 300 nm-thick MgF_2 layer is sandwiched between the prism and the MIM structure to reduce the index asymmetry caused by high-indexed SF11 prism. On the other side of this MIM structure is several microns of Rh6G/PMMA. Compared to structures without the MgF_2

layer, this structure has relative lower modal loss owing to its less deviation from the symmetric MIM geometry. In the following numerical calculation, we adopt the experiment design given in Ref [31]: The Rh6G/PMMA is around $10\mu\text{m}$ thick and exhibits optical gain at wavelength $\lambda = 594\text{nm}$ with an achievable gain coefficient of 420 cm^{-1} . The gain medium is assumed to be infinite thick since its thickness is far beyond the penetration of SPP field. The reflectance R was probed with p polarized He-Ne laser beam at $\lambda = 594\text{ nm}$.

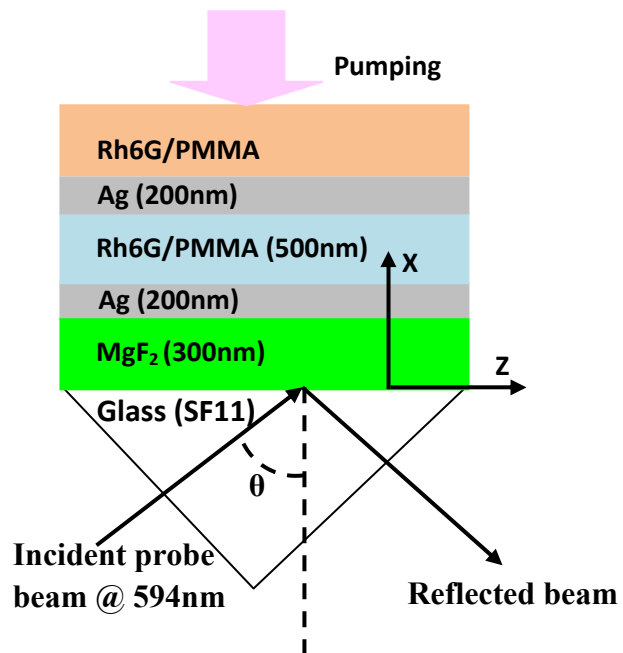


Fig. 5.7 Schematic of SPP excitation in an ATR geometry.

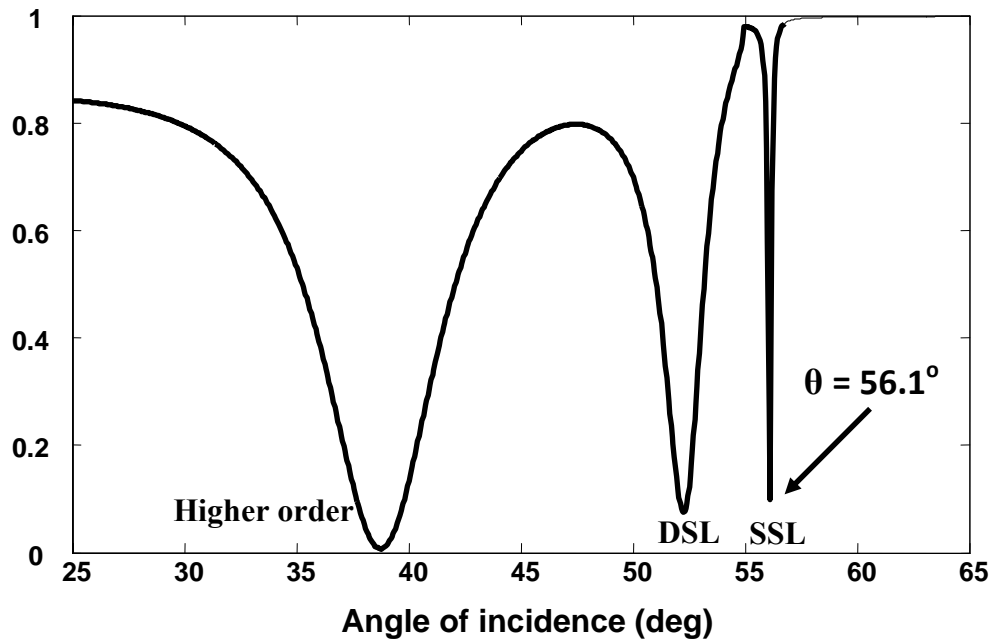


Fig. 5.8 ATR reflectance curve at 594nm for SF₁₁ prism-MgF₂-Ag-PMMA-Ag-Rh6G/PMMA geometry, sketched in Fig. 5.7, as a function of incidence angle θ with zero Rh6G gain.

Figure 5.8 shows that the prism(SF11)-MgF₂-Ag-PMMA-Ag-Rh6G/PMMA structure in the ATR geometry, as sketched in Fig. 5.7, has three resonance dips at $\theta = 56.1^\circ$, 52.3° and 38.75° . These three resonance conditions respectively correspond to excitation of a SSL, DSL and higher order SP modes in the MIM waveguide. As discussed in Chapter 4.1, narrower resonance indicates smaller amount of loss, therefore, the SSL mode with narrowest resonance width is considered.

The calculated reflectance on a logarithmic scale versus incidence angles around 56.1° with various gain values are plotted in Fig. 5.9. The labeled gain values are given in terms of $n''_{\text{Rh6G/PMMA}}$ i.e. the imaginary part of refractive index of Rh6G/PMMA. At wavelength $\lambda = 594 \text{ nm}$, $n''_{\text{Rh6G/PMMA}} = 0, 1.0 \times 10^{-3}, 1.5 \times 10^{-3}$ and 2.0×10^{-3} correspond to

gain coefficients $\gamma = 0, 212, 317$ and 420 cm^{-1} , respectively. For the red curve labeled double gain layer, the central PMMA layer is replaced by Rh6G/PMMA, which is also pumped to act as an active media having the same gain coefficient as external one. Experimentally, strong emission signal from Rh6G/PMMA film, which is blocked by 40nm thick silver, has been observed [31]. Therefore, the central Rh6G/PMMA layer covered by top 20nm thick Ag film can be fully pumped and exhibiting gain, thus the double gain layer case is feasible.

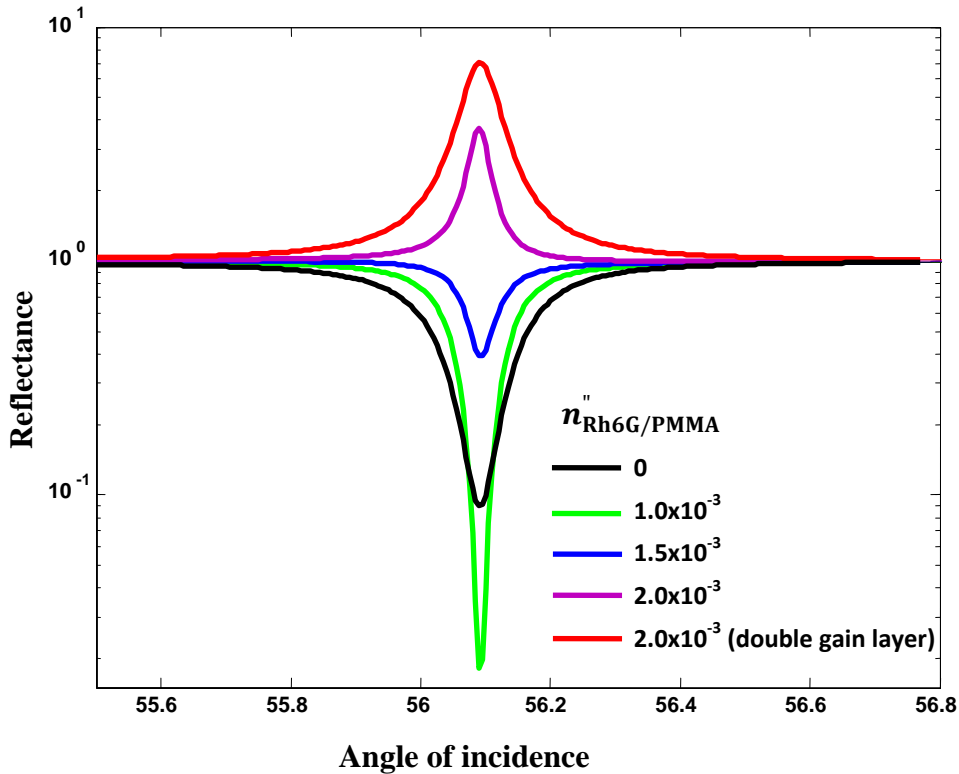


Fig. 5.9 Reflectance of the MIM structure in ATR geometry (depicted in Fig.5.7) as a function of incidence angle θ for various gain values. The gain values are given by $n''_{\text{Rh6G/PMMA}}$ the imaginary part of refractive index of Rh6G/PMMA. For the red curve labeled double gain layer, the central PMMA layer is replaced by Rh6G/PMMA.

Figure 5.9 shows that the minimal reflectance initially reduced at small gain values till passing the zero reflectance, and then increased at larger gain values. Without gain inclusion, the normal ATR resonance dip (black curve) associated with the excitation of SPPs is observed. In the curve for $n''_{\text{Rh6G/PMMA}} = 1.0 \times 10^{-3}$ (or $\gamma = 212 \text{ cm}^{-1}$), we see a narrower and deeper resonance dip. In the curve for $n''_{\text{Rh6G/PMMA}} = 1.5 \times 10^{-3}$ (or $\gamma = 317 \text{ cm}^{-1}$), we see a reduced ATR, which means the gain is still not sufficient to completely compensate the loss. Between these two values, there exists one gain value that lets ATR reflectance equal 0. Enhanced reflectance with value larger than 1 around the SPR angle is observed in the curves (purple and red) for $n''_{\text{Rh6G/PMMA}} = 2.0 \times 10^{-3}$ (or $\gamma = 420 \text{ cm}^{-1}$), indicating the effective gain effect exceeding the metal absorption [23].

In addition to the angular reflectance versus gain, the corresponding normalized Poynting vector fields (defined as Poynting vector \mathbf{S} divided by incident parallel energy flux - S_{iz}) at SPR angle 56.1° are illustrated in Fig. 5.10. Figure 5.10(A), corresponding to the excitation of a single (prism)-sided leaky SP mode in the MIM waveguide without gain, shows no energy flowing into or out of the waveguide through the top Au-Rh6G/PMMA interface. The incident power is coupled through the bottom prism-MgF₂ interface into the SSL mode and the peak energy flux, about 80 times incident parallel energy flux is localized on the exiting Ag interfaces. This normalized peak energy flux magnitude is about 3 times bigger than that of a single metal layer waveguide, investigated in Ref. [31]. When $n''_{\text{Rh6G/PMMA}} = 1.0 \times 10^{-3}$, 1.5×10^{-3} and 2.0×10^{-3} (external gain only), the peak energy flux remains localized on the exiting Ag interfaces and the respective normalized magnitude is around 220, 460 and 1500. The tilted energy flux, flowing from the gain medium into the waveguide to compensate the waveguide loss also

increases with increasing gain values. Figure 5.10(D) inset (c) and Fig. 5.10(E) reveal net energy flux out of the MIM waveguide through the bottom MgF_2 -prism interface into the prism. This indicates the reflected wave possessing larger energy flow comparing with incident wave, thus confirming the occurrence of enhanced reflectance. Comparing subplots (D) and (E), it is interesting to note that the normalized peak energy flux localized on exiting Ag interfaces is reduced from 1500 (when only external gain applies) to around 400 (when double gain layer applies). The additional central gain layer actually reduces the peak energy magnitude.

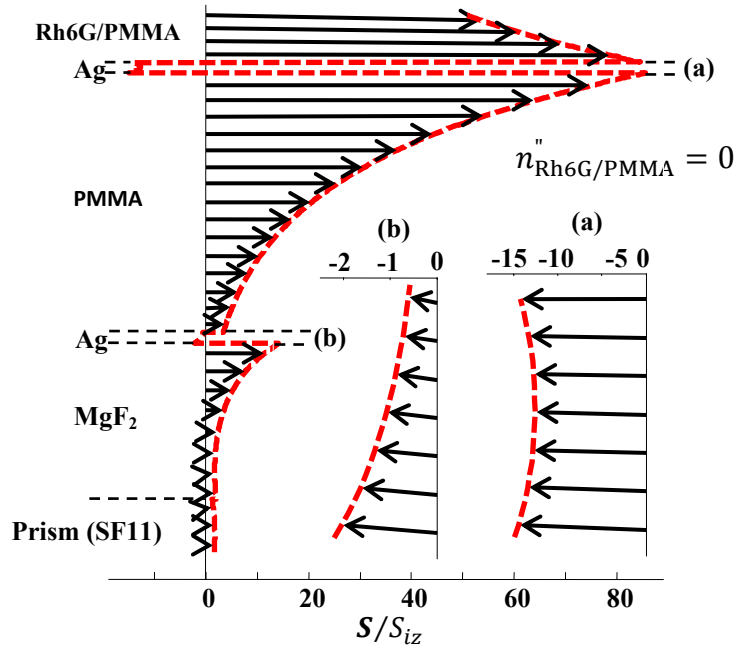


Fig. 5.10 (A)

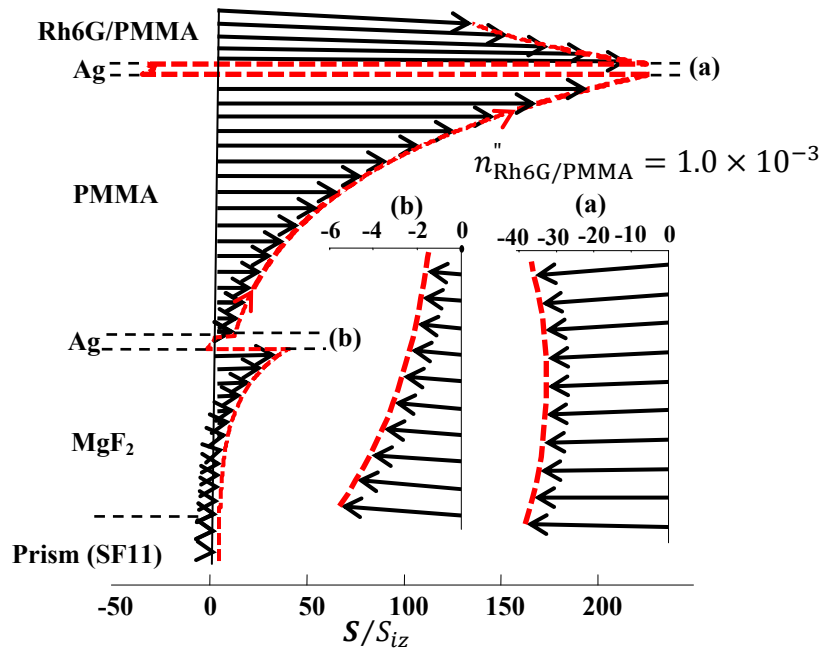


Fig. 5.10 (B)

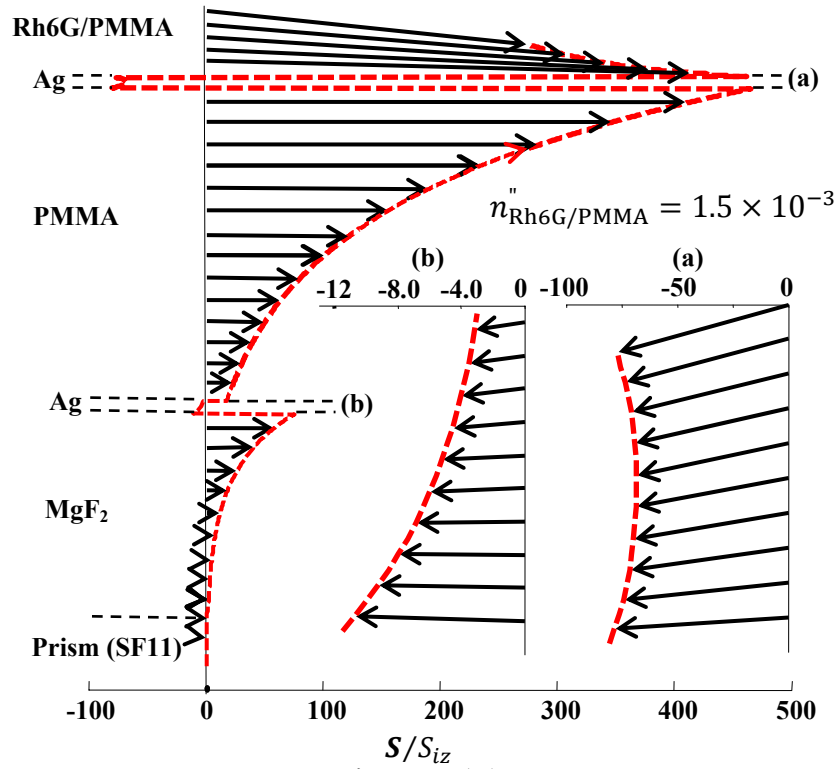


Fig. 5.10 (C)

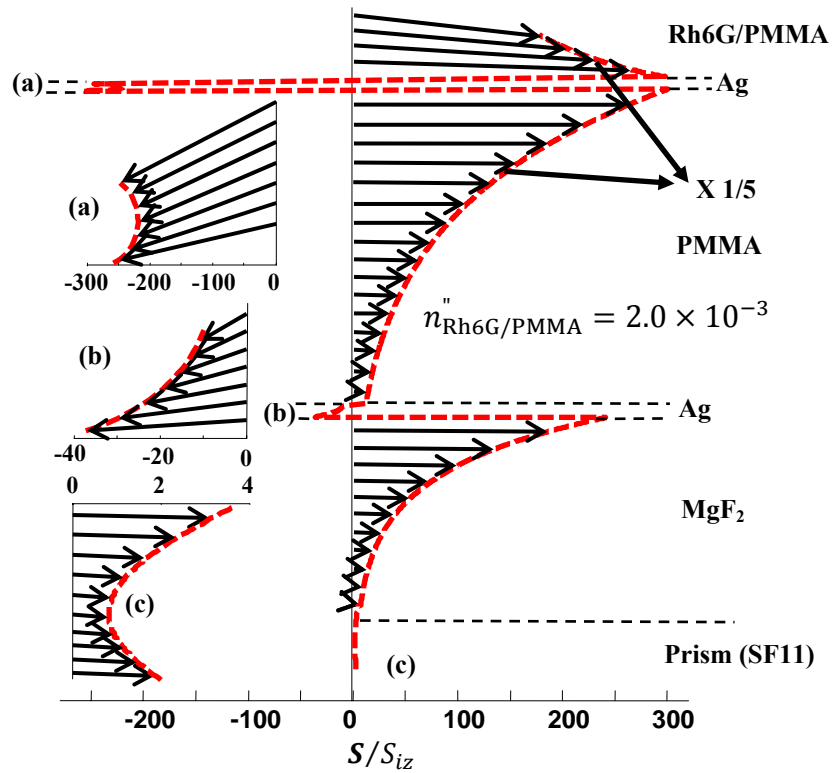


Fig. 5.10 (D)

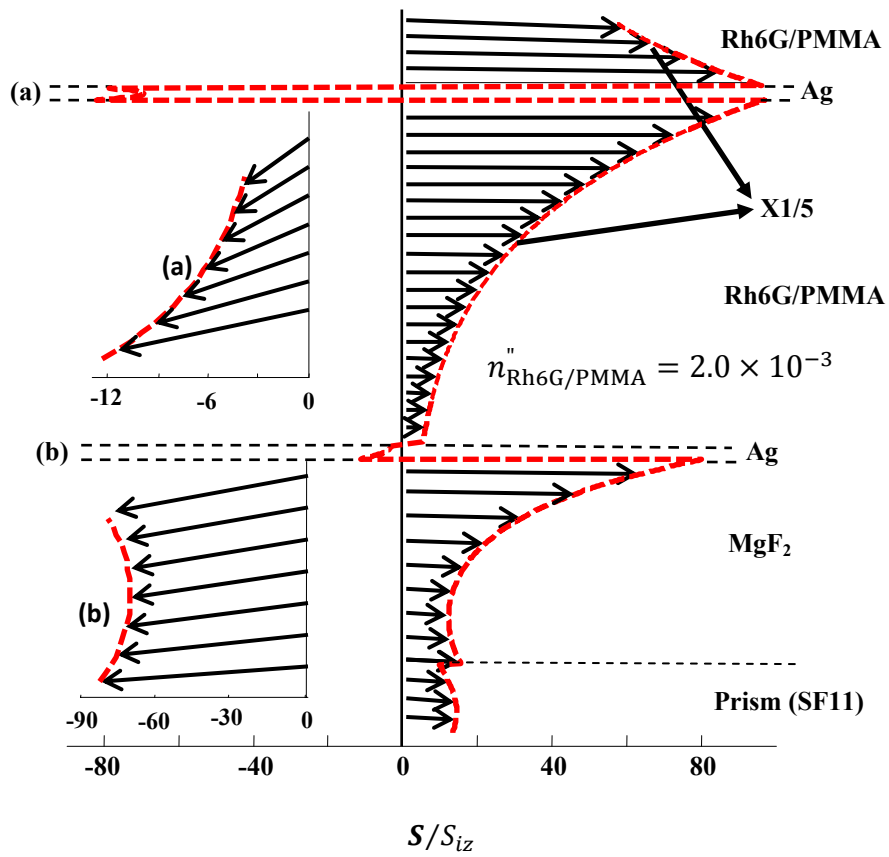


Fig. 5.10 Normalized Poynting vector fields versus gain value at the incidence angle of 56.1° . The gain values are given in terms of the imaginary part of refractive index of Rh6G/PMMA ($n''_{\text{Rh6G/PMMA}}$). Subplots (A) - (D) correspond to gain values of 0 , 1.0×10^{-3} , 1.5×10^{-3} and 2.0×10^{-3} , respectively. Subplot (E) corresponds to the double gain layer case with both gain values of 2.0×10^{-3} .

References

- [1] W. L. Barnes, A. Dereux and T. W. Ebbesen, "Surface plasmon subwavelength optics," *Nature* **424**, 824 (2003).
- [2] E. Ozbay, "Plasmonics: Merging photonics and electronics at nanoscale dimensions," *Science* **311**, 189 (2006).
- [3] V. M. Shalaev, "Optical negative-index metamaterials," *Nat. Photon.* **1**, 41 (2007).
- [4] K. Kneipp, Y. Wang, H. Kneipp, L. T. Perelman, I. Itzkan, R. R. Dasari, and M. S. Feld, "Single molecule detection using surface-enhanced raman scattering (SERS)," *Phys. Rev. Lett.* **78**, 1667 (1997).
- [5] S. Nie and S. R. Emory, "Probing single molecules and single nanoparticles by surface-enhanced raman scattering," *Science* **275**, 1102 (1997).
- [6] S. Lal, S. Link, and N. J. Halas, "Nano-optics from sensing to waveguiding," *Nat. Photonics* **1**, 641 (2007).
- [7] J. N. Anker, W. P. Hall, O. Lyandres, N. C. Shah, J. Zhao, and R. P Van Duyne, "Biosensing with plasmonic nanosensors," *Nat. Mater.* **7**, 442 (2008).
- [8] D. E. Chang, A. S. Sørensen, P. R. Hemmer, and M. D. Lukin, "Quantum optics with surface plasmons," *Phys. Rev. Lett.* **97**, 053002 (2006).
- [9] J. J. Ju, S. Park, M. Kim, J. T. Kim, S. K. Park, Y. J. Park, and M. Lee, "40 Gbit/s light signal transmission in long-range surface plasmon waveguides," *Appl. Phys. Lett.* **91**, 171117 (2007).
- [10] A. Neogi, C. W. Lee, H. Everitt, T. Kuroda, A. Tackeuchi, and E. Yablanovich, "Enhancement of spontaneous recombination rate in a quantum well by resonant surface plasmon coupling," *Phys. Rev. B* **66**, 153305 (2002).
- [11] I. Pockrand, A. Brillante, and D. Moebius, "Exciton-surface plasmon coupling: an experimental investigation," *J. Chem. Phys.* **77**, 6289 (1982).
- [12] J. Bellessa, C. Bonnand, J. C. Plenat, and J. Mugnier, "Strong coupling between surface plasmons and excitons in an organic semiconductor," *Phys. Rev. Lett.* **93**, 036404 (2004).

- [13] A. Boltasseva and S. I. Bozhevolnyi, "Directional couplers using long-range surface plasmon polariton waveguides," *J. Sel. Top. Quantum Electron.* **12**, 1233 (2006).
- [14] I. E. Protsenko, A. V. Uskov, O. A. Zaimidoroga, V. N. Samoilo, and E. P. O'Reilly, "Dipole nanolaser," *Phys. Rev. A* **71**, 063812 (2005).
- [15] I. Gontijo, M. Boroditsky, E. Yablonovitch, S. Keller, U. K. Mishra, and S. P. DenBaars, "Coupling of InGaN quantum-well photoluminescence to silver surface plasmons," *Phys. Rev. B* **60**, 11564 (1999).
- [16] N. E. Hecker, R. A. Höpfel, N. Sawaki, T. Maier, and G. Strasser, "Surface plasmon-enhanced photoluminescence from a single quantum well," *Appl. Phys. Lett.* **75**, 1577 (1999).
- [17] J. Vuckovic, M. Loncar, and A. Scherer, "Surface plasmon enhanced light-emitting diode," *IEEE J. Quantum Electron.* **36**, 1131 (2000).
- [18] K. Okamoto, I. Niki, A. Shvartser, Y. Narukawa, T. Mukai, and A. Scherer, "Surface-plasmon-enhanced light emitters based on InGaN quantum wells," *Nat. Mater.* **3**, 601 (2004).
- [19] P. A. Hobson, S. Wedge, J. A. E. Wasey, I. Sage, and W. L. Barnes, "Surface plasmon mediated emission from organic light-emitting diodes," *Advanced Materials* **14**, 1393 (2002).
- [20] T. D. Neal, K. Okamoto and A. Scherer, "Surface plasmon enhanced emission from dye doped polymer layers," *Opt. Express* **13**, 5522 (2005).
- [21] Z. Yu, G. Veronis, S. Fan, and M. L. Brongersma, "Gain-induced switching in metal-dielectric-metal plasmonic waveguides," *Appl. Phys. Lett.* **92**, 041117 (2008).
- [22] M. Ambati, S. H. Nam, E. Ulin-Avila, D. A. Genov, G. Bartal, and X. Zhang, "Observation of stimulated emission of surface plasmon polaritons," *Nano letters* **8**, 3998 (2008).
- [23] G. A. Plotz, H. J. Simon, and J. M. Tucciarone, "Enhanced total reflection with surface plasmons," *J. Opt. Soc. Am.* **69**, 419 (1979).
- [24] A. N. Sudarkin and P. A. Demkovich, "Excitation of surface electromagnetic waves on the boundary of a metal with an amplifying medium," *Sov. Phys. Tech. Phys.* **34**, 764 (1989).

- [25] C. Sirtori, C. Gmachl, F. Capasso, J. Faist, D. L. Sivco, A. L. Hutchinson, and A. Y. Cho, "Long-wavelength ($\lambda \approx 8\text{--}11.5\mu\text{m}$) semiconductor lasers with waveguides based on surface plasmons," *Opt. Lett.* **23**, 1366 (1998).
- [26] A. Tredicucci, C. Gmachl, F. Capasso, A. L. Hutchinson, D. L. Sivco, and A. Y. Cho, "Single-mode surface-plasmon laser," *Appl. Phys. Lett.* **76**, 2164 (2000).
- [27] M. P. Nezhad, K. Tetz, and Y. Fainman, "Gain assisted propagation of surface plasmon polaritons on planar metallic waveguides," *Opt. Express* **12**, 4072 (2004).
- [28] I. Avrutsky, "Surface plasmons at nanoscale relief gratings between a metal and a dielectric medium with optical gain," *Phys. Rev. B* **70**, 155416 (2004).
- [29] J. Seidel, S. Grafström, and L. Eng, "Stimulated emission of surface plasmons at the interface between a silver film and an optically pumped dye solution," *Phys. Rev. Lett.* **94**, 177401 (2005).
- [30] M. Z. Alam, J. Meier, J. S. Aitchison, and M. Mojahedi, "Gain assisted surface plasmon polariton in quantum wells structures," *Opt. Express* **15**, 176 (2007).
- [31] M. A. Noginov, V. A. Podolskiy, G. Zhu, M. Mayy, M. Bahoura, J. A. Adegoke, B. A. Ritzo, and K. Reynolds, "Compensation of loss in propagating surface plasmon polariton by gain in adjacent dielectric medium," *Opt. Express* **16**, 1385 (2008).
- [32] D. J. Bergman and M. I. Stockman, "Surface plasmon amplification by stimulated emission of radiation: Quantum generation of coherent surface plasmons in nanosystems," *Phys. Rev. Lett.* **90**, 027402 (2003).
- [33] N. M. Lawandy, "Localized surface plasmon singularities in amplifying media," *Appl. Phys. Lett.* **85**, 5040 (2004).
- [34] M. A. Noginov, G. Zhu, M. Bahoura, J. Adegoke, C. E. Small, B. A. Ritzo, V. P. Drachev, and V. M. Shalaev, "Enhancement of surface plasmons in an Ag aggregate by optical gain in a dielectric medium," *Opt. Lett.* **31**, 3022 (2006).
- [35] E. P. Ippen and C. V. Shank, "Evanescent-field-pumped dye laser," *Appl. Phys. Lett.* **21**, 301 (1972).
- [36] K. O. Hill, A. Watanabe, and J. G. Chambers, "Evanescent-wave interactions in an optical wave-guiding structures," *Appl. Opt.* **11**, 1952 (1972).
- [37] W. Y. Liu and O. M. Stafsudd, "Optical amplification of a multimode evanescently active planar optical waveguide," *Appl. Opt.* **29**, 3114 (1990).

- [38] B. Ya. Kogan, V. M. Volkov, and S. A. Lebedev, "Superluminescence and generation of stimulated radiation under internal-reflection conditions," JETP Lett. **16**, 100 (1972).
- [39] G. N. Romanov and S. S. Shakhidzhanov, "Amplification of electromagnetic field in total internal reflection from a region of inverted population," JETP Lett. **16**, 209 (1972).
- [40] S. A. Lebedev, V. M. Volkov, and B. Ya. Kogan, "Value of the gain for light internally reflected from a medium with inverted population," Opt. Spectrosc. **35**, 565 (1973).
- [41] P. R. Callary and C. K. Carniglia, "Internal reflection from an amplifying layer," J. Opt. Soc. Am. **66**, 775 (1976).
- [42] W. Lukosz and P. P. Herrmann, "Amplification by reflection from an active medium," Optics Comm. **17**, 192 (1976).
- [43] R. F. Cybulski, Jr. and C. K. Carniglia, "Internal reflection from an exponential amplifying region," J. Opt. Soc. Am. **67**, 1620 (1977).
- [44] S. A. Lebedev and B. Ya. Kogan, "Light amplification by internal reflection from an inverted medium," Opt. Spectrosc. **48**, 564 (1980).
- [45] R. F. Cybulski and M. P. Silverman, "Investigation of light amplification by enhanced internal reflection. I. Theoretical reflectance and transmittance of an exponentially nonuniform gain region," J. Opt. Soc. Am. **73**, 1732 (1983).
- [46] M. P. Silverman and R. F. Cybulski, "Investigation of light amplification by enhanced internal reflection. II. Experimental determination of the single-pass reflectance of an optically pumped gain region," J. Opt. Soc. Am. **73**, 1739 (1983).
- [47] J. Fan, A. Dogariu, and L. J. Wang, "Amplified total internal reflection," Opt. Express **11**, 299 (2003).
- [48] M. Born and E. Wolf, *Principles of Optics*, 6th edition, Cambridge (1997).
- [49] H. J. Moon, S. P. Sun, J. H. Lee, and K. An, "Guided mode lasing in a double-layered square microcavity," Appl. Phys. Lett. **83**, 2521 (2003).

Chapter 6 MIM Plasmonic Waveguides in Terahertz

Quantum Cascade Laser

6.1 Introduction

The terahertz (THz) frequency range, as shown in Fig. 6.1, is defined as the frequencies from 300GHz to 10 THz ($1 \text{ GHz} = 10^9 \text{ Hz}$, $1 \text{ THz} = 10^{12} \text{ Hz}$), or the wavelengths from $30 \mu\text{m}$ to $1000 \mu\text{m}$. However, the THz region has remained one of the least developed spectral regions largely due to a relative lack of compact and convenient radiation sources, detectors and transmission technology. This underexplored terahertz portion of the electromagnetic spectrum is sometimes called as the “terahertz gap”.

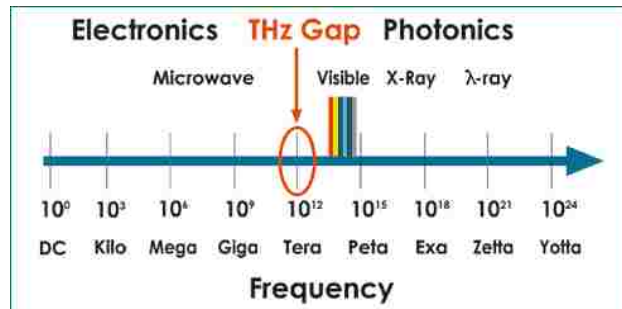


Fig. 6.1 Road map of electromagnetic spectrum [1].

Terahertz waves have wide potential applications including but not limited to: astrophysics and atmospheric science, the chemical and biological materials identification, biomedical imaging, security screening, non-destructive evaluation, communications and ultrafast spectroscopy. These wide-ranging terahertz waves proposed applications generally required a compact, coherent, high-power, continuous wave (c.w.) solid-state source. However, the high frequency power generated by solid-

state electronic devices, such as transistors, Gunn oscillators and Schottky diode multipliers, is limited by power rolling off phenomena owing to both transit-time and resistance–capacitance effects [2, 3], and the best available power generated above 1THz is well below the milliwatt level [4]. Direct THz generation through photonic approaches is limited by the lack of appropriate interband materials with sufficiently small bandgaps. Despite various photonic techniques have been developed to generate radiation above 1THz, these techniques (for example, nonlinear or photoconductive effects induced down-conversion from the visible regime, or multiplication up from the millimeter-wave regime, or direct generation with optically pumped molecular gas lasers or free-electron lasers) are either mainly limited by output power or extensive cryogenic cooling requirement, or by pulsed operation, or by their size, cost or complexity. Extensive reviews on terahertz sources can be found in Refs (1, 5-6).

Given successful and ubiquitous implementation of semiconductor laser throughout the visible and near-infrared frequency range, the semiconductor THz laser is an appealing device. Conventional semiconductor lasers, bipolar type lasers, working by radiative recombination of conduction band electrons with valence band holes, are limited to radiation frequency range inherently determined by the bandgaps of the constituent active materials. The lack of appropriate interband materials, large free-carrier absorption losses and practical limitations on the thickness of epilayer growth make conventional laser waveguides unsuitable for the THz range.

A new class of laser known as quantum cascade laser (QCL) is based on a fundamentally different principle from conventional semiconductor lasers. QCLs are unipolar lasers using only one type of charge carrier (usually electrons). The molecular-

beam epitaxy grown multiple-quantum-well (MQW) active region based on the GaAs/Al_xGa_{1-x}As material system is the core of any QC laser. Typically 100–200 repetitions of the MQW module are grown to form active regions between the bottom contact and top metal layer. The repeated MQW module (also known as a stage) is formed by alternating layers of GaAs and Al_xGa_{1-x}As with each layer just a few nanometers thick. Each module is consisted of injector and superlattice active region. Injector/collector structures connect these superlattice active regions, allowing electrical transport through injection of carriers into the upper laser level and extraction of carriers from the lower laser level. The conduction band across each identical repeat stage is split into a series of discrete energy levels called subbands [7] owing to the quantization of electron motion perpendicular to the layers.

By applying a voltage bias across the QCL device, the electron energy drops in successive stages to form potential staircase. When an electron in the higher energy subband drops to a lower energy level within that stage, it can be ‘recycled’ to the higher energy subband of the successive stage. This “recycling” process is repeated in identical successive stages, causing the electrons to cascade down a series of identical energy steps like an electronic waterfall, emitting a photon at each step and consequently emitting many photons on its way. This is in contrast to diode lasers which emit only single photon over the similar cycle. A revolutionary aspect of QCL is that in principle QCL can operate at arbitrarily long wavelengths over an extremely wide range by precisely engineering the MQW active region band structures using the same material combination. Therefore, the QC scheme has long been the preferred choice in fabricating a THz semiconductor laser.

QCL was invented and first demonstrated at wavelength of 4 μm (75 THz) in 1994 [7]. Since then, QC lasers have successfully spanned the mid-infrared frequency range 3~24 μm [8-11] and become the dominant mid-infrared semiconductor laser sources. Many QCLs have been demonstrated working at room-temperature and c.w. operation with hundreds of milliwatts power from 3.8–10.6 μm [12, 13]. In 2001, the first QC laser with a photon energy less than the semiconductor optical phonon energy ($\sim 8\text{THz}$) was demonstrated at 4.4 THz (equivalent to a wavelength of 67 μm). This THz QC laser employed a chirped superlattice active region combined with a semi-insulating surface-plasmon (SI-SP) waveguide [14]. Recent developments have demonstrated QCL spectral coverage over 0.84 – 5.0 THz [15-17] and c.w. operation at 117K [18], and 130 mW C.W output power [19]. Therefore THz QCLs are the most promising candidates for bridging the “terahertz gap”.

6.2 Basics of Quantum Cascade Laser

6.2.1 Quantum Casecade Laser Active Region

The heart of QC laser, i.e. the MQW active region is usually grown by using MBE in the GaAs/ $\text{Al}_x\text{Ga}_{1-x}\text{As}$ material system. There exits four major design classes of QCL active regions: the chirped superlattice, bound-to-continuum, resonant-phonon and hybrid ‘interlaced’ design combining the bound-to-continuum design with phonon-assisted depopulation [20, 21]. These four major QCL active region design schemes have been excellently reviewed in Ref. [22].

6.2.2 Quantum Cascade Laser Waveguides

When extending QCLs from the mid-infrared regime to longer wavelengths, QCLs waveguide design becomes a very important aspect due to two reasons:

(i) Conventional laser dielectric waveguides are unsuitable for the THz range due to the difficulty in scaling their dimensions up with increasing wavelength. This is caused by the practical epitaxy layer thickness limitation ($\sim 10\mu\text{m}$) of the MBE growth.

(ii) Free carrier absorption (α_{fc}) increases strongly at longer wavelengths ($\alpha_{fc} \propto \lambda^2$). Therefore, unique waveguides are needed to have minimum free-carrier loss in the cladding layers by minimizing the mode overlap with any doped cladding layers.

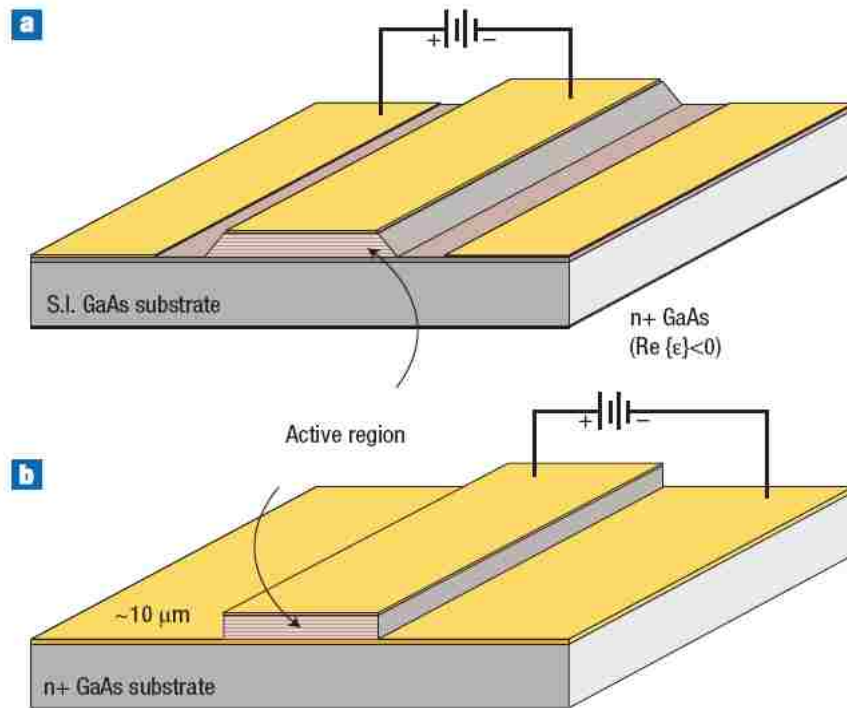


Fig. 6.2 Schematic diagrams of THz QC-laser waveguides for (a) SI-SP and (b) MM waveguides. n^+ indicates heavily doped semiconductor and $\text{Re}\{\epsilon\} < 0$ indicates the real part of the dielectric permittivity is less than zero [22].

SP modes at one interface has been exploited in the mid-infrared QCLs to achieve tight optical confinement as well as low absorption losses [11, 23]. However, at THz frequencies, double-SP structures have to be applied since the simple single-SP waveguides only have a small overlap of the optical mode with the active region of reasonable thickness. To date, two types of waveguides, as shown in Fig. 6.2, have been used for THz QC lasers: the semi-insulating surface-plasmon (SI-SP) waveguide and the metal-metal (MM) waveguide. They both use the double-sided SP as the confinement mechanism. Instead of using two metal layers in MM waveguide, SI-SP replaces one metal layer with a plasma layer formed by a heavily doped semiconductor layer. Currently, MM waveguides tend to have the best high-temperature performance, and SI-SP waveguides have higher output powers and better beam patterns (More details can be found in Ref. [22]). They both have similar lasing thresholds.

(i) Semi-insulating Surface Plasmon Waveguide

The SI-SP waveguide, as depicted in Fig. 6.2 (a), consists of an active region sandwiched between an upper thin GaAs contact layer with Au contact on top, and a bottom thin (0.2–0.8 μm thick) heavily n-doped (n^+) GaAs layer, which is on top of a semi-insulating GaAs substrate [8, 14, 24, 25]. This bottom n^+ layer is called plasma layer since its dielectric constant can be made negative by appropriate high doping level and acts as a “metal” ($\text{Re}\{\epsilon\} < 0$). The free-electron plasmas in heavily doped GaAs layer is used to create a low loss TM mode bounded to that layer. Consequently a coupled SP mode is bound to the top metal contact and the lower plasma layer. This lower plasma

layer also serves as an electrical path between the side metal contacts and the active region.

Even with the largest attainable doping level ($\sim 5 \times 10^{18} \text{ cm}^{-3}$ in GaAs), the mode extends substantially into the substrate. However, the overlap with doped regions is small so that the free-carrier loss is small. The confinement factor Γ of SI-SP waveguide is far below unity and typically lies in the range of 0.1–0.5 for reported lasers. Γ will become even smaller at longer wavelengths ($> 100 \mu\text{m}$) because of the inherent reduced geometric overlap at longer wavelengths, and because as frequency ω approaches the active region plasma frequency (ω_p), the dielectric constant in lightly doped active region is reduced by a factor of $(1 - \omega_p^2/\omega^2)$ compared to the dielectric constant in the SI substrate. The relative loosely confined mode in SI-SP waveguide, on one hand, enables employing relative wide ridges without supporting multiple lateral modes, while on the other hand, it limits the minimum device area owing to the tendency of squeezing mode into the substrate with narrow ridges ($< \sim 100 \mu\text{m}$) [22, 29].

(ii) Metal-Metal Double Surface Plasmon Waveguide

As an alternative to the SI-SP waveguide, the MM waveguide consists of an active region sandwiched between a thin metal contact and a metal substrate, as depicted in Fig. 6.2(b). It utilizes SPs at both metal surfaces to obtain a guided mode which is almost completely contained between two metal cladding layers [18, 26 - 28, 30, 31].

MM waveguide is an appealing solution due to two reasons – the metal–semiconductor–metal geometry is compatible with the TM polarization of intersubband transitions; and a relatively low loss and a high confinement factor (nearly unity), owing

to shallow skin depth in metals, have been achieved. However, compared with the SI-SP waveguide, the MM waveguide involves more complicated fabrication process, including metallic wafer-bonding and substrate removal with polishing and selective etching [27]. As the doped contact layers are very thin, the MM waveguide losses are primarily caused from the metal dissipation and the usually non-negligible active region re-absorption.

6.3 Electromagnetic Modeling of THz QCL Waveguides

There are three important parameters to characterize a laser waveguide: waveguide loss coefficient α_w , accounting for scattering and absorption inside the waveguide, confinement factor Γ , describing the overlap of the mode with the active region, and mirror loss coefficient α_m , indicating facet reflectivity induced optical coupling losses. These three parameters, α_w , α_m and Γ , which are associated only with the passive waveguide structure, determine the threshold material gain g_{th} (threshold gain in short hereafter). The threshold gain is the required minimum gain to reach the lasing threshold, where the modal gain (Γg_{th}) equals the total losses ($\alpha = \alpha_w + \alpha_m$). Therefore, the threshold gain g_{th} is expressed as

$$g_{th} = \alpha/\Gamma = (\alpha_w + \alpha_m)/\Gamma \quad (6.1)$$

Waveguide with minimized threshold gain results in reduced threshold current densities and increased operating temperatures. Therefore, in the following simulation, g_{th} is used as the criteria for judging waveguide performance.

The following numerical modeling presents a one-dimensional analysis of terahertz QCL waveguides. Propagation constant (k) and confinement factor (Γ) of both SI surface-plasmon and metal-metal waveguides are obtained by using the transfer matrix

formalism (see Appendix C) along with Newton-Raphson root searching algorithm (See Appendix D) in the complex wave vector plane. For SI-SP waveguide, the effects of the plasma layer doping level and thickness and the substrate thickness are analyzed. For metal-metal waveguides, the effects of active region thickness are analyzed.

Waveguide loss is given by $\alpha_w = 2\text{Im}\{k\}$. The major THz waveguide losses originate from two parts: (i) free-carrier absorption loss in the metal and doped semiconductors; (ii) phonon absorption in semiconductors which is only significant for frequencies near the *Reststrahlen* band ($\omega_{TO}/2\pi \approx 8\text{THz}$) in GaAs at elevated temperatures [29]. The former loss was taken into account by using an effective complex permittivity following the Drude-Lorentz model approximation, which has been described in Chapter 2.3. This model is rewritten here as:

$$\varepsilon(\omega) = \varepsilon_\infty(\omega) - \frac{Ne^2}{m^*} \cdot \frac{1}{\omega(\omega + i\omega\gamma)} \quad (6.2)$$

where N is the carrier density, m^* is the electron effective mass, ω is the angular frequency, and τ is the relaxation time (the damping rate is given by $\gamma = 1/\tau$) which is carrier density dependent. The latter phonon loss, for simplicity, is not included in the simulation over frequency range 2–7 THz where phonon losses are not prohibitively high for the operation of THz QCLs.

Mirror loss is calculated by using the effective index method (effective modal index $n_{eff} = k/k_0$, k_0 is the free space wave number), the same method widely used in optical and mid-infrared waveguide designs. This method has also been successfully used for mid-infrared QCL design [7] and over lower frequencies beyond mid-infrared [29]. Therefore, the mirror loss is expressed as $\alpha_m = -\ln R/L$, where L is the laser cavity length, and R is the facet reflectivity. The facet reflectivity R equals to square of the

Fresnel reflection coefficient, which is related with the effective material refractive index (i.e. n_{eff}) through $(n_{eff} - 1)/(n_{eff} + 1)$. Note that this effective index method is no longer valid in the microwave regime, where waveguides design follows the transmission line theory and the reflectivities are determined from the impedance mismatch theory.

For all following simulated structures, $\epsilon_{\infty}(\omega) = 12.96\epsilon_0$ (ϵ_0 is the vacuum permittivity) for GaAs without including phonon effects, GaAs electron effective mass $m^* = 0.0632m_0$ (m_0 is free-electron mass), the Drude relaxation time are 0.5ps for the lightly doped GaAs layers (active region), 0.1ps for the heavily doped GaAs layers (n^+ plasma layer) and 0.05 ps for the Au contacts [29]. The carrier density for the active region and metal layers are set at $2 \times 10^{15} \text{cm}^{-3}$ and $5.9 \times 10^{22} \text{cm}^{-3}$, respectively. In addition, for all calculations, the laser cavity length is 3 mm and the Au contacts are infinite thick.

6.3.1 Semi-infinite Surface Plasmon Waveguide Design

The SI-SP waveguide (Fig. 6.2(a)) consists of an active region layer sandwiched between a thin upper n^+ doped contact layer with a Au contact above it, and a thin n^+ doped GaAs layer (referred to as the plasma layer) with a semi-insulating GaAs substrate underneath. This structure results in coupled SP modes bound to the top metal contact and the lower plasma layer.

The parameters used in simulation for SI-SP waveguide performance are listed in Table 6.1.

Table 6.1 List of the parameters used for SI-SP waveguide simulation

Frequency f (THz)	2.0, 3.0, 4.0, 5.0, 7.0
Upper n^+ GaAs contact layer thickness	100 nm (fixed)
Upper n^+ GaAs contact layer doping	$5.0 \times 10^{18} \text{ cm}^{-3}$ (fixed)
Active region thickness	10 μm (fixed)
Active region doping	$2.0 \times 10^{15} \text{ cm}^{-3}$ (fixed)
Bottom n^+ GaAs plasma layer thickness (d_{pl})	300 – 800 nm
Bottom n^+ GaAs plasma layer doping (n_{pl})	$(1.0 - 5.0) \times 10^{18} \text{ cm}^{-3}$
SI-GaAs substrate thickness	25 – 250 μm

The influences of plasma layer doping on waveguide loss, confinement factor and g_{th} are illustrated in Fig. 6.3. Free-carrier absorption in active region decreases as frequency increases. Therefore, the increasing of waveguide loss α_w with increasing frequency at fixed plasma doping (or decreasing plasma doping at fixed frequency (except at 2 THz)), as shown in Fig. 6.3(a), is caused by increased free-carrier absorption in the plasma layer as the frequency approaches the bulk plasma frequency. The refractive index of active region (metal and plasma layer) increases (decreases) with increasing frequency and the refractive index of plasma layer increases with increasing plasma doping. Numerical results reveal that the effective modal index increases with both increasing frequency and plasma doping. However the changes of mirror loss caused by the changes of modal index are negligible, especially at lower frequencies.

Larger confinement factors are obtained at higher frequencies and lower plasma doping (See Fig. 6.3(b)). At frequencies lower than 2 THz where confinement factors are lower than 0.1, a thicker active region is required.

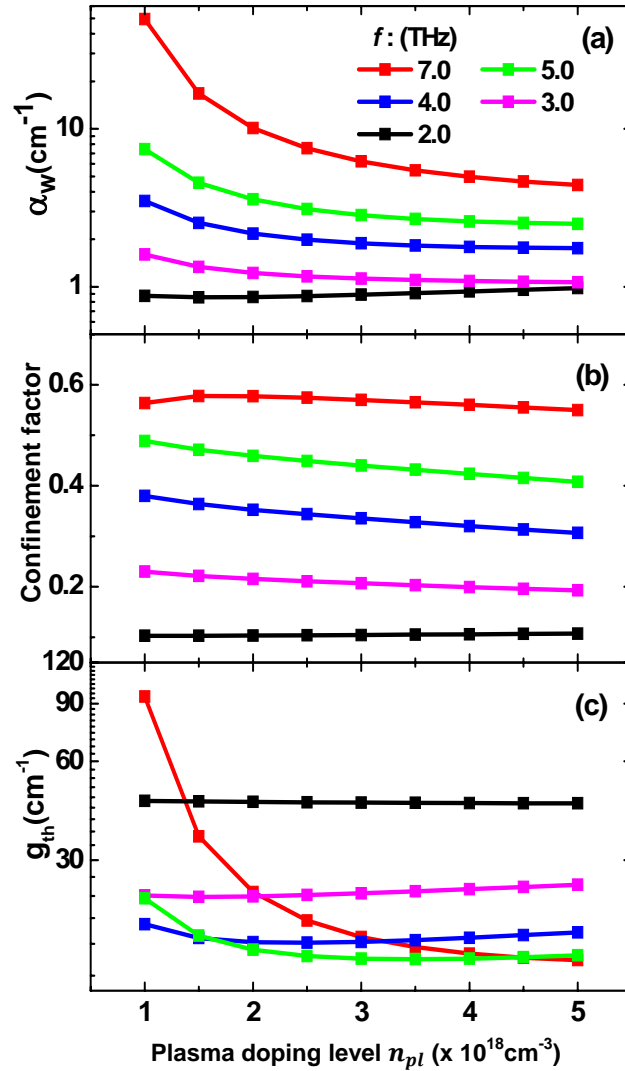


Fig. 6.3 SI-SP waveguide simulated results for (a) waveguide loss (α_w), (b) confinement factor (Γ), and (c) threshold gain (g_{th}) versus plasma doping (n_{pl}) for plasma layer thickness of 400 nm at frequencies 2.0, 3.0, 4.0, 5.0 and 7.0 THz.

As plotted in Fig. 6.3(c), at a fixed plasma doping level, as the lasing frequency increases to 5 THz, smaller g_{th} is observed owing to the increased confinement factor in spite of the increased waveguide loss. This indicates that g_{th} is more sensitive to any changes in Γ below 0.5 than the increases in α_w . At high frequencies and the lower end of plasma doping level, the lasing frequency is close to the bulk plasma frequency, thus the waveguide loss is reduced quite sensitively with increasing plasma doping, and g_{th} behaves similarly for similar reasons.

Figure 6.4 shows that the plasma layer thickness also influences the waveguide performance. As plotted in Fig. 6.4 (a), a thicker plasma layer with fixed doping results in a larger α_w as the mode overlaps more extensively with the lossy material. On the other hand, the mode is prevented from extending into the substrate, resulting in a higher confinement factor (see Fig. 6.4(b)). Using g_{th} as the criteria for judging waveguide performance, optimum plasma doping levels can be found from Fig. 6.4(c), where g_{th} versus plasma doping at various plasma layer thicknesses are plotted, and exhibiting a clear minima. Repeating this process at other frequencies, optimum plasma doping levels at different frequencies for various plasma layer thicknesses are summarized in Table 6.2.

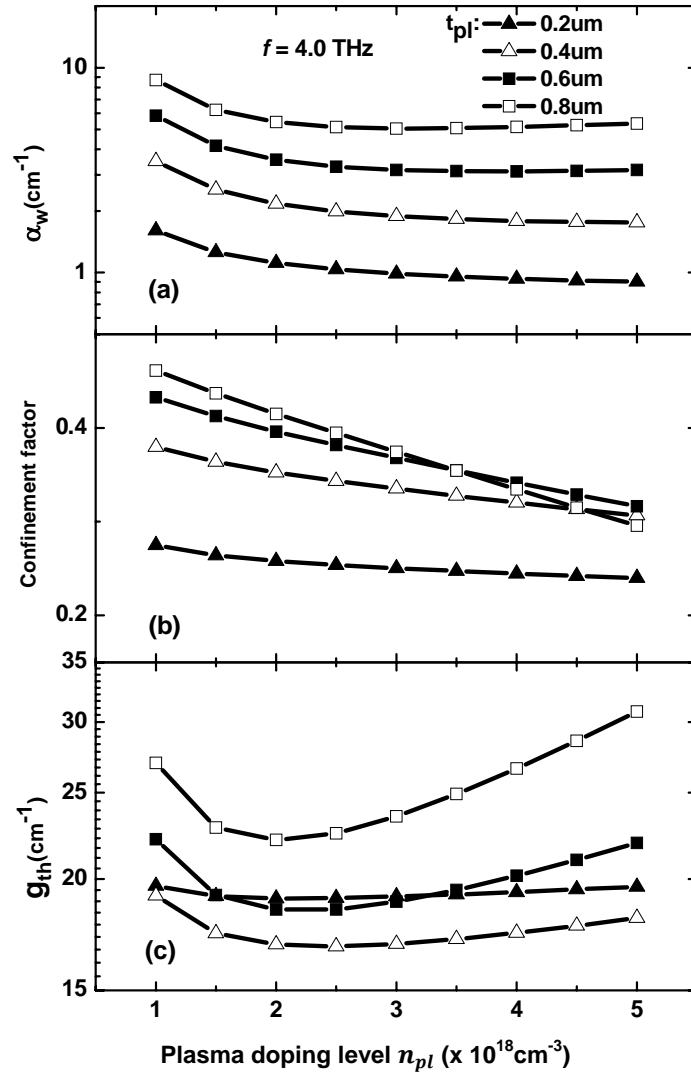


Fig. 6.4 SI-SP waveguide simulated results for (a) waveguide loss (α_w), (b) confinement factor (Γ), and (c) threshold gain (g_{th}) versus plasma doping for plasma layer thickness (t_{pl}) of 200, 400, 600 and 800 nm at 4 THz.

Table 6.2 Optimum plasma layer doping range ($\times 10^{18}\text{cm}^{-3}$) and respective $g_{th}(\text{cm}^{-1})$ *

$d_{pl}(\text{nm})$ $f(\text{THz})$	200	400	600	800
7.0	1.0-5.0 (~19)	4.0-5.0 (~15)	4.0-5.0(~22)	4.5-5.0(~32)
5.0	1.0-5.0(~14)	2.0-5.0 (~19)	2.0-5.0(~18)	2.0-4.0(~24)
4.0	1.0-5.0(~19)	1.0-5.0(~17)	1.5-4.0(~18)	1.5-3.0(~22)
3.0	1.0-5.0(~32)	1.0-5.0(~23)	1.0-3.5(~21)	1.0-2.5(~23)
2.0	1.0-5.0(~57)	1.0-5.0(~45)	1.0-4.0(~38)	1.0-2.5(~34)

*the number of respective g_{th} is written in italic inside“()”.

For the thinnest plasma layer modeled, 200 nm, changes in plasma doping do not affect g_{th} over the whole investigated frequency range. A similar case occurs for a 400 nm-thick plasma layer over frequencies 2-4 THz. Beyond this region where g_{th} is insensitive to any changes of plasma doping, the optimum doping range shrinks as the frequency and/or the plasma layer thickness increases, the higher frequency and/or the thicker plasma layer, the narrower optimum doping range. To minimize g_{th} , a thin plasma layer with high doping is preferred at $f \geq 5$ THz while thick layer with low doping at $f \leq 3$ THz. At frequencies around 4 THz, given optimum doping, the plasma layer thickness is not critical.

Figure 6.5 shows the influence of substrate thickness for various plasma doping at different frequencies. The variations in α_w , Γ and g_{th} with substrate thickness are not sensitive to the plasma doping level. At low frequencies, as shown in the left panel at 3.0 THz, Γ increases and g_{th} decreases with decreasing substrate thickness. At high frequencies, as shown in the right panel at 5.0 THz, the increase in Γ and decrease in g_{th} only occur for extremely thin substrates, when the wavelength in the semiconductor

comparable to the thickness of the substrate. Therefore, at low frequencies, the substrate should be thinned as much as possible to optimize the waveguide design by decreasing g_{th} and increasing the confinement factor.

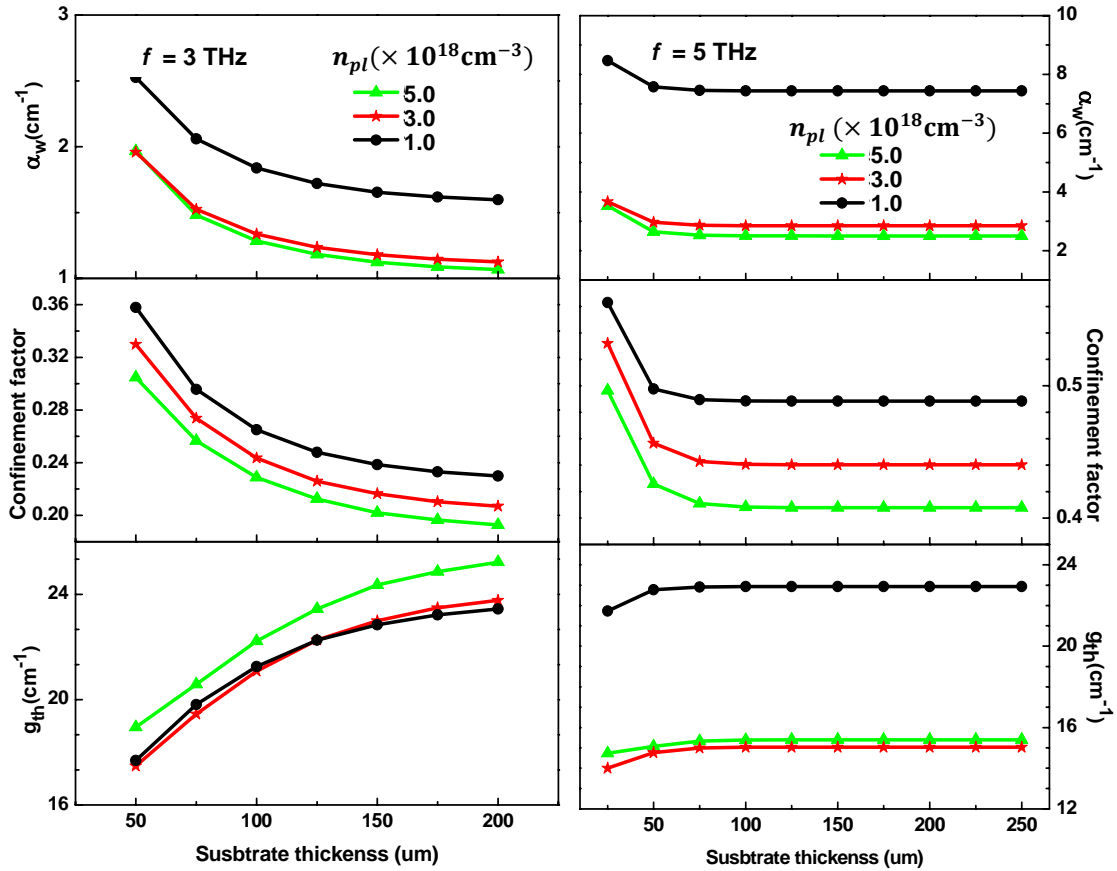


Fig. 6.5 SI-SP waveguide simulated results for waveguide loss (α_w), confinement factor (Γ), and threshold gain (g_{th}) versus substrate thickness at 3 THz (left) and 5 THz (right). The plasma layer is 400 nm thick at plasma doping (n_{pl}) of 1.0×10^{18} , 3.0×10^{18} and $5.0 \times 10^{18} \text{ cm}^{-3}$.

6.3.2 Metal-Metal Waveguide Design

Numerical results show that the modal indexes for MM waveguides are larger than those for SI-SP waveguides. Like the SI-SP waveguide, the MM waveguide modal

index also depends on the frequency and waveguide geometry. Larger modal index is obtained with increasing frequency and decreasing active region thickness. The changes of mirror loss induced by modal index variations are also negligible as that in SI-SP waveguide.

Figure 6.6 presents the effect of changing active region thickness at various frequencies for MM waveguides. The SI-SP waveguide results are included for comparison. For MM waveguides, the waveguide loss α_w decreases as the active region thickness increases, due to a decreasing relative modal overlap with the lossy materials including the metal and contact layers. At low frequencies, α_w increases and the sensitivity of α_w to the active region thickness decreases as frequency decreases, while at high frequencies α_w and its sensitivity both increase with increasing frequency. This can be explained in this way: At low frequencies, as the frequency approaches the bulk plasma frequency of the active region (0.443 THz), the metal contacts induced losses become less important and the waveguide loss is more dominated by the increased active region free-carrier absorption, which is not sensitive to the active region thickness; At high frequencies approaching the bulk plasma frequency of metal contact layer (22.17THz), waveguide loss is dominated by losses associated with the SPs at the metal contacts, which is more sensitive to the active region thickness. Comparing to SI-SP waveguide, larger waveguide loss in MM waveguide is observed due to the absorption loss in the additional metal layer.

The confinement factors for MM waveguide are nearly unity, which are far beyond that of SI-SP waveguide. For MM waveguides, the variations of g_{th} can be well

approximated by that of waveguide loss α_w , owing to the nearly unity confinement factors and negligible changes of mirror loss.

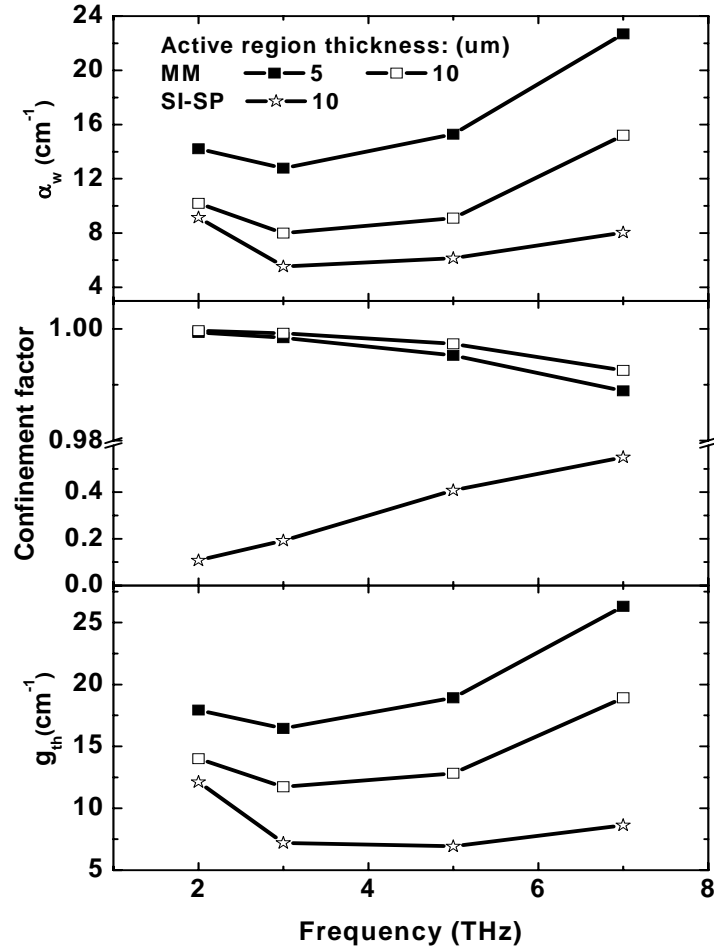


Fig. 6.6 Waveguide loss (α_w), confinement factor (Γ), and threshold gain (g_{th}) for MM waveguide with active region thicknesses of 5 and 10 μm at frequencies $f = 2.0$, 3.0, 5.0 and 7.0 THz. Between the top/bottom Au contacts, the active region is sandwiched between two contact layers (one is 100nm thick and another one is 400 nm thick) both doped at $5 \times 10^{18} \text{cm}^{-3}$. The results for a SI-SP waveguide with 10 μm thick active region are included as reference. Its upper contact layer (100 nm) and bottom plasma layer (400 nm) are both doped the same as that in MM waveguide.

6.3.3 THz QCL SP Leaky Waveguide Design

The MIM leaky mode can be applied in THz QCLs to extract their power out of the structures. But one metal layer within MIM has to be replaced by a plasma layer due to extra thin skin depth of metal at this frequency range. We still called it MIM waveguide because indeed it has similar underlying physics as MIM. This section presents simulated results for this purpose. The simulated waveguide structure, as sketched in Fig. 6.7, is the same as the MM waveguide except the top metal contact layer on the ridge. Instead of solid top metal contact layer used in the MM waveguide, patterned top metal contact has to be applied here. The leaky waves will come out through the parts without metal coverage. As shown in Fig. 6.7, the two n^+ GaAs layers sandwiching the active region are labeled as plasma layer and bottom contact layer, respectively. For the following numerical simulations, the bottom contact layer is 100 nm thick and doped at $5 \times 10^{18} \text{ cm}^{-3}$.

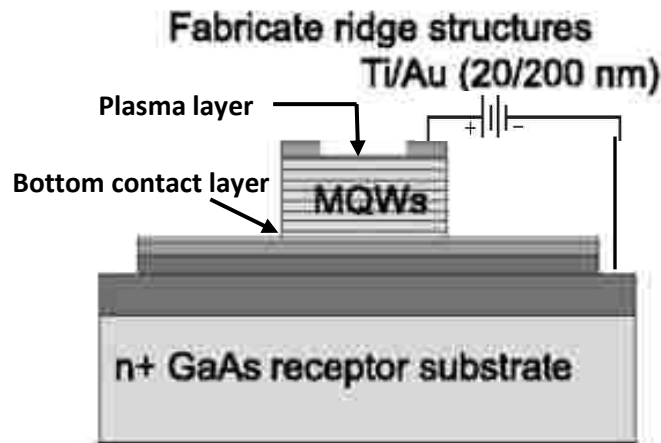


Fig. 6.7 Schematic for THz QCL MIM Leaky Waveguide

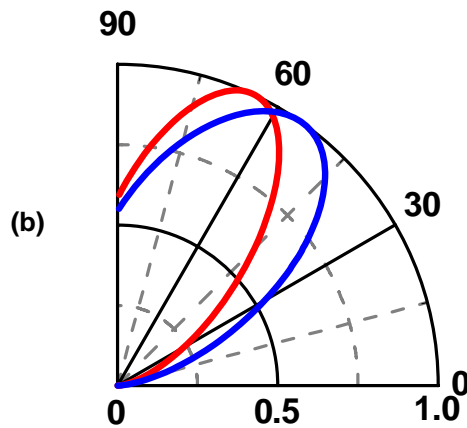
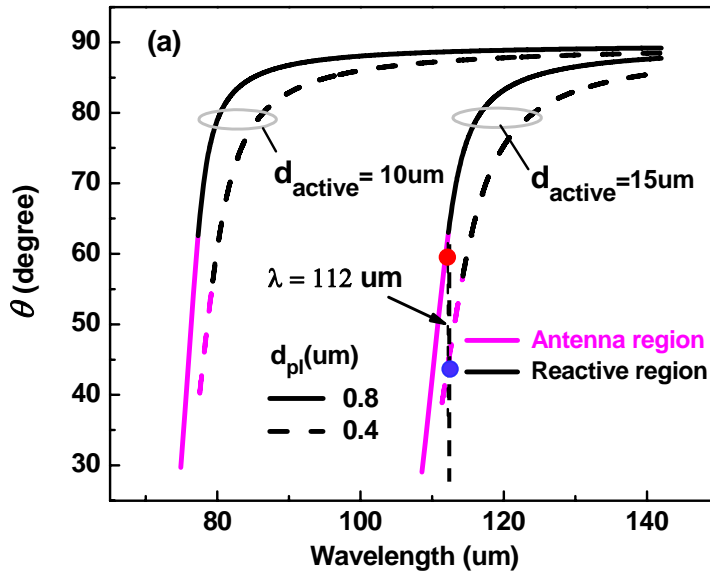


Fig. 6.8 Leaky wave-front tilt θ (a) for waveguides with active region thicknesses (d_{active}) of 10 and 15 μm and with plasma layer thicknesses (d_{pl}) of 400 and 800 nm; Radiation patterns at wavelength 112 μm (b) for waveguides with $d_{active} = 15 \mu\text{m}$ and $d_{pl} = 400 \text{ nm}, 800 \text{ nm}$. The plasma layer is doped at $5 \times 10^{18} \text{ cm}^{-3}$.

Repeating leaky wave analysis described in Chapter 3.3.3, the leaky wave-front tilt θ and radiation patterns are plotted in Fig. 6.8. The leaky wave-front tilt θ is defined as before, i.e. the angle relative to the surface. As active region thickness (d_{active})

increases, the leaky wave shifts to longer wavelength, however the leaky wave-front tilt and radiation pattern are not sensitive to this change. As plasma layer thickness (d_{pl}) increases, the antenna region shifts to longer wavelength with smaller peak radiation tilt. Narrower antenna spectra and radiation lobes are found for thicker plasma layer. Numerical results (data not shown) reveal that the plasma layer doping level doesn't significantly influence the leaky wave properties.

References

- [1] http://www.rpi.edu/terahertz/about_us.html.
- [2] P. H. Siegel, "Terahertz technology," *IEEE Trans. Microwave Theory Tech.* **50**, 910 (2002).
- [3] D. L. Woolard, E. R. Brown, M. Pepper, and M. Kemp, "Terahertz frequency sensing and imaging: A time of reckoning future applications?" *Proc. IEEE* **93**, 1722 (2005).
- [4] A. Maestrini, J. Ward, J. Gill, H. Javadi, E. Schlecht, G. Chattopadhyay, F. Maiwald, N. R. Erickson, and I. Mehdi, "A 1.7–1.9 THz local oscillator source," *IEEE Microwave Wireless Components Lett.* **14**, 253 (2004).
- [5] M. Tonouchi, "Cutting-edge terahertz technology," *Nature Photon.* **1**, 97 (2007).
- [6] B. Ferguson and X. C. Zhang, "Materials for terahertz science and technology," *Nature Mater.* **1**, 26 (2002).
- [7] J. Faist, F. Capasso, D. L. Sivco, C. Sirtori, A. L. Hutchinson, and A. Y. Cho, "Quantum cascade laser," *Science* **264**, 553 (1994).
- [8] B. S. Williams, H. Callebaut, S. Kumar, Q. Hu, and J. L. Reno, "3.4-THz quantum cascade laser based on LO-phonon scattering for depopulation," *Appl. Phys. Lett.* **82**, 1015 (2003).
- [9] D. G. Revin, J. W. Cockburn, M. J. Steer, R. J. Airey, M. Hopkinson, A. B. Krysa, L. R. Wilson, and S. Menzel, "InGaAs/AlAsSb/InP quantum cascade lasers operating at wavelengths close to 3 μm ," *Appl. Phys. Lett.* **90**, 021108 (2007).
- [10] M. P. Semtsiv, M. Wienold, S. Dressler, and W. T. Masselink, "Short-wavelength ($\lambda \approx 3.05 \mu\text{m}$) InP-based strain-compensated quantum-cascade laser," *Appl. Phys. Lett.* **90**, 051111 (2007).
- [11] R. Colombelli, F. Capasso, C. Gmachl, A. L. Hutchinson, D. L. Sivco, A. Tredicucci, M. C. Wanke, A. M. Sergent, and A. Y. Cho, "Far-infrared surface-plasmon quantum-cascade lasers at 21.5 μm and 24 μm wavelengths," *Appl. Phys. Lett.* **78**, 2620 (2001).
- [12] J. S. Yu, A. Evans, S. Slivken, S. R. Darvish and M. Razeghi, "Temperature dependent characteristics of $\lambda \sim 3.8\mu\text{m}$ room-temperature continuous-wave quantum-cascade lasers," *Appl. Phys. Lett.* **88**, 251118 (2006).

- [13] S. Slivken, A. Evans, W. Zhang, and M. Razeghi, “High-power, continuous-operation intersubband laser for wavelengths greater than 10 μm ,” *Appl. Phys. Lett.* **90**, 151115 (2007).
- [14] R. Köhler, A. Tredicucci, F. Beltram, H. E. Beere, E. H. Linfield, A. G. Davies, D. A. Ritchie, R. C. Iotti, and F. Rossi, “Terahertz semiconductor-heterostructure laser,” *Nature* **417**, 156 (2002).
- [15] J. Faist, G. Scalari, C. Walther and M. Fischer, “Progress in long wavelength terahertz quantum cascade lasers”, 2007 Materials Research Society (MRS) Spring Meeting, San Fransisco, California, April 2007 CC7.2 (2007).
- [16] G. Scalari, C. Walther, J. Faist, H. Beere, and D. Ritchie, “Electrically switchable, two-color quantum cascade laser emitting at 1.39 and 2.3 THz,” *Appl. Phys. Lett.* **88**, 141102 (2006).
- [17] A. W. M. Lee, Q. Qin, S. Kumar, B. S. Williams, Q. Hu, and J. L. Reno, “Real-time terahertz imaging over a standoff distance (> 25 meters),” *Appl. Phys. Lett.* **89**, 141125 (2006).
- [18] B. S. Williams, S. Kumar, Q. Hu, and J. L. Reno, “Operation of terahertz quantum-cascade lasers at 164 K in pulsed mode and at 117 K in continuous-wave mode,” *Opt. Express* **13**, 3331 (2005).
- [19] B. S. Williams, S. Kumar, Q. Hu, and J. L. Reno, “High-power terahertz quantum cascade lasers,” *Electron. Lett.* **42**, 89 (2006).
- [20] R. Köhler, A. Tredicucci, C. Mauro, F. Beltram, H. E. Beere, E. H. Linfield, A. G. Davies, and D. A. Ritchie, “Terahertz quantum-cascade lasers based on an interlaced photon-phonon cascade,” *Appl. Phys. Lett.* **84**, 1266 (2004).
- [21] G. Scalari, N. Hoyler, M. Giovannini, and J. Faist, “Terahertz bound-to-continuum quantum cascade lasers based on optical-phonon scattering extraction,” *Appl. Phys. Lett.* **86**, 181101 (2005).
- [22] B. S. Williams, “Terahertz quantum-cascade lasers,” *Nature Photon.* **1**, 517 (2007).
- [23] C. Sirtori, C. Gmachl, F. Capasso, J. Faist, D. L. Sivco, A. L. Hutchinson, and A. Y. Cho, “Long-wavelength ($\sim 8\text{--}11.5$ mm) semiconductor lasers with waveguides based on surface plasmons,” *Opt. Lett.* **23**, 1366 (1998).
- [24] J. Ulrich, R. Zobl, N. Finger, K. Unterrainer, G. Strasser, and E. Gornik, “Terahertz-electroluminescence in a quantum cascade structure,” *Physica B* **272**, 216 (1999).

- [25] M. Rochat, L. Ajili, H. Willenberg, J. Faist, H. Beere, G. Davies, E. Linfield, and D. Ritchie, "Low-threshold terahertz quantum-cascade lasers," *Appl. Phys. Lett.* **81**, 1381 (2002).
- [26] M. Rochat, M. Beck, J. Faist, and U. Oesterle, "Measurement of far-infrared waveguide loss using a multisection single-pass technique," *Appl. Phys. Lett.* **78**, 1967 (2001).
- [27] B. S. Williams, S. Kumar, H. Callebaut, Q. Hu, and J. L. Reno, "Terahertz quantum-cascade laser at $\lambda \approx 100 \mu\text{m}$ using metal waveguide for mode confinement," *Appl. Phys. Lett.* **83**, 2124 (2003).
- [28] S. Kumar, B. S. Williams, S. Kohen, Q. Hu, and J. L. Reno, "Continuous-wave operation of terahertz quantum-cascade lasers above liquid-nitrogen temperature," *Appl. Phys. Lett.* **84**, 2494 (2004).
- [29] S. Kohen, B. S. Williams, and Q. Hu, "Electromagnetic modeling of terahertz quantum cascade laser waveguides and resonators," *J. Appl. Phys.* **97**, 053106 (2005).
- [30] K. Unterrainer, R. Colombelli, C. Gmachl, F. Capasso, H. Y. Hwang, A. M. Sergent, D. L. Sivco, and A. Y. Cho, "Quantum cascade lasers with double metal-semiconductor waveguide resonators," *Appl. Phys. Lett.* **80**, 3060 (2002).
- [31] C. Walther, G. Scalari, J. Faist, H. Beere, and D. Ritchie, "Low frequency terahertz quantum cascade laser operating from 1.6 to 1.8 THz," *Appl. Phys. Lett.* **89**, 231121 (2006).

Chapter 7 Conclusions and Future Works

7.1 Conclusions

In this work, the finite planar MIM plasmonic waveguides have been analyzed theoretically and experimentally.

The complete SP mode set for finite MIM waveguides with real metals is solved using the transfer-matrix formalism. Two SP mode pairs originating from the well-known low/high energy branches of single metal film SPs are revealed. The three lowest energy modes remain as bound modes while the highest energy branch exhibits non-radiative (bound) and radiative (leaky) portions separated by a spectral gap. The leaky regime is further divided into antenna and reactive mode regions. The antenna mode, characterized by the propagation of mode energy out of the waveguide, possesses well-defined radiation pattern and is technologically important because it enables direct coupling to free space and novel beam steering devices. Taking into account of spatial dispersion effect, the S_L mode is observed with reduced wave-vector in dispersion curve and increased propagation loss.

The radiative SP modes were investigated theoretically and experimentally by ATR method in Kretschmann configuration and by free space coupling. The single- and double-sided leaky waves excited with prism coupling show differences in energy flux properties when on or off resonance. There exist differences between the minimum ATR reflectance, the phase-matching condition and optimum excitation of leaky modes. Free-space coupling to the antenna leaky wave has been experimentally demonstrated. The leaky wave dispersion relation and its antenna mode radiation pattern are determined

through both angle- and wavelength-dependent reflectance of TM polarized free space incident light.

Realistic finite MIM structures with the inclusion of dye-doped polymer were considered. The propagation of three bound SP modes, each mode within its respective optimized symmetric glass-Ag-Rh6G/PMMA-Ag-glass waveguides, is numerically analyzed for core material exhibiting optical gain at 594 nm. The lossless propagation of S_H mode is predicted for a gain coefficient lower than the reported gain coefficient of 420 cm^{-1} for Rh6G/PMMA. The MIM propagating SPPs in the ATR Kretschmann setup with gain in adjacent medium are simulated. The reflectance and energy flux for various gain values are presented. The addition of core gain actually downgrades its performance.

The waveguide loss, confinement factor and threshold gain for THz QCL SP waveguides are modeled over frequency range 2 - 7 THz. For SI-SP waveguide, the plasma layer thickness, plasma doping and substrate thickness will affect its performance, and the optimum plasma layer thickness and doping at different frequencies are determined in terms of obtaining minimum threshold gain. For MM waveguide, the confinement factor is nearly unity, and the trend of threshold gain can be approximated by that of waveguide loss. For these two waveguides, the variation of mirror coupling loss is not sensitive to structure parameters. The SP leaky waveguide has been proposed. The leak properties can be adjusted by varying plasma layer thickness.

7.2 Suggestions for Future Works

This dissertation has demonstrated, through both numerical simulation and experimental analysis, free space coupling via finite planar MIM leaky mode. Here an

actuator modulator based on the free-space coupling technique is proposed. The designed actuator modulator is illustrated in Fig. 7.1. A thin piezoelectric layer is sandwiched between two Au layers, which also serve as the electrodes. The bottom Au layer is optically thick enough such that leaky wave only exists on the top side. This device operates in this way: when fixing the incidence angle, at a specific incidence frequency, i.e. at the resonance frequency, phase-matching between the *p*-polarized incident and MIM leaky wave occurs, the free space incident laser beam is coupled into the MIM waveguide. Applying an electric field across the piezoelectric core layer will change the core layer thickness via the inverse piezoelectric effect, shifting the resonance frequency, and changing the coupling efficiency of the incident light into the waveguide, and thus modulating the reflected light intensity.

One easy and feasible choice for the thin piezoelectric layer is lead-zirconate-titanate (PZT), which has high piezoelectricity and can easily be formed by RF sputtering or sol-gel process. Zr/Ti ~0.52/0.48 is known as the morphotropic phase boundary, and at this composition, i.e. $\text{Pb}(\text{Zr}_{0.52}\text{Ti}_{0.48})\text{O}_3$ has the best piezoelectric properties. PZT has high breakdown field strength ($> 1\text{MV/cm}$). The displacement ΔL is proportion to the applied actuation voltage. It is expressed by $\Delta L = d_{33}V$, where d_{33} is the piezoelectric strain coefficient in unit pm/V in direction parallel to the direction of the applied field. The sputtered or sol-gel derived PZT thin film doesn't show piezoelectric properties automatically. It needs to be annealed at temperature higher than 450°C to result in the crystallization of the perovskite PZT (111) phase. After that an electric poling process is required.

For PZT (52, 48), d_{33} is normally much larger than 100 pm/V. When applying a 10 V voltage across the MIM structure, the displacement along the applied field direction is larger than 1nm. As shown in Fig.7.1 (b), a 1nm variation in the core layer thickness shifts the resonance wavelength 6nm away and causes around 15% difference in the reflected beam intensity, which is detectable.

In addition, continuous work on experimental verification of the results and predictions presented in Chapter 4, 5 and 6 are interesting, especially the QCL with MIM leaky waveguide for extracting power out of the structure.

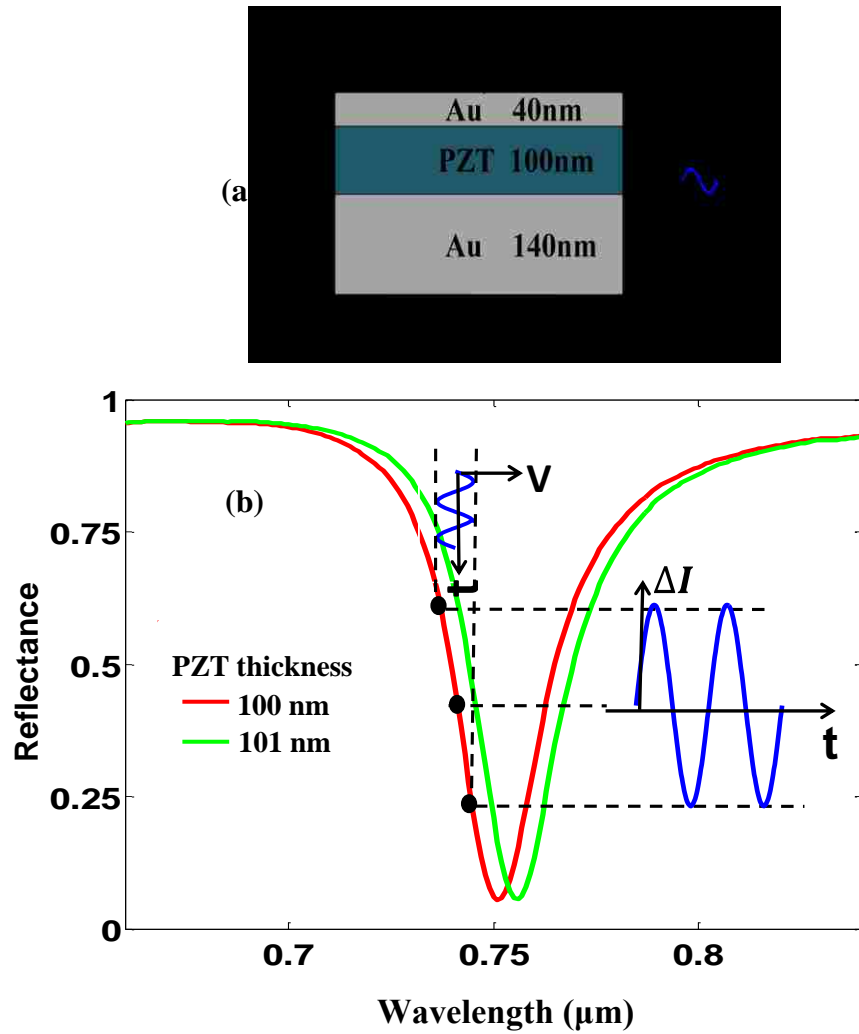


Fig. 7.1 (a) The configuration of actuator modulator based on free-space coupling. (b) Schematic of intensity modulation of the reflected light induced by a periodically varying PZT thickness. The curves (red and green) are modeled with PZT index of 2.5, incidence angle of 30° with respect to the normal direction.

Appendix A General Electromagnetics Theory

A.1 Maxwell's Equations

Maxwell's equations are the set of four fundamental partial differential equations governing all electromagnetic behaviors. Maxwell's macroscopic differential equations for a wave propagating through a non-magnetic medium are:

$$\nabla \times \mathbf{E} = -\frac{\partial \mathbf{B}}{\partial t} \quad (\text{A. 1a})$$

$$\nabla \cdot \mathbf{D} = \rho \quad (\text{A. 1b})$$

$$\nabla \times \mathbf{H} = \mathbf{J} + \frac{\partial \mathbf{D}}{\partial t} \quad (\text{A. 1c})$$

$$\nabla \cdot \mathbf{B} = 0 \quad (\text{A. 1d})$$

The vector quantities are the electric field vector \mathbf{E} in *volts/meter*[V/m], the magnetic field vector \mathbf{H} in *ampere/meter*[A/m], the electric displacement (or electric flux density) vector \mathbf{D} in *coulombs/meter²* [C/m²], the magnetic induction (or magnetic flux density) vector \mathbf{B} in *webers/meter²* or *Tesla*[T], the electric current density vector \mathbf{J} in *ampere/meter²*[A/m²], and ρ is the free charge density in *coulombs/meter³*[C/m³].

Implicit in Maxwell's equations is the continuity equation for the charge and current density, showing the conservation of electric charges. It is expressed as

$$\nabla \cdot \mathbf{J} + \frac{\partial \rho}{\partial t} = 0 \quad (\text{A. 1e})$$

A.2 Constitutive Relations

In a linear isotropic nonmagnetic homogeneous material, the four vectors, \mathbf{E} , \mathbf{H} , \mathbf{B} and \mathbf{D} , involved in the Maxwell's equations (A.1) are related to each other through the constitutive relations

$$\mathbf{D} = \varepsilon_0 \mathbf{E} + \mathbf{P} = \varepsilon_0(1 + \mathcal{X})\mathbf{E} = \varepsilon_0 \varepsilon_r \mathbf{E} = \varepsilon \mathbf{E} \quad (\text{A. 2a})$$

$$\mathbf{B} = \mu_0 \mathbf{H} \quad (\text{A. 2b})$$

where ε_0 is the vacuum permittivity equal to $8.854 \times 10^{-12} \text{ m}^{-3} \text{ kg}^{-1} \text{ s}^4 \text{ A}^2$, μ_0 is the vacuum permeability equal to $4\pi \times 10^{-7} \text{ Hm}^{-1}$, ε_r denotes the relative dielectric permittivity, \mathbf{P} is the polarization density which is aligned with and proportion to the electric field \mathbf{E} through the electric susceptibility \mathcal{X} . \mathbf{P} is zero for free space.

The current density \mathbf{J} and the electric field \mathbf{E} are related through the ohm's law $\mathbf{J} = \sigma \mathbf{E}$, where σ is the conductivity. In a dielectric material, there is no free charges and current, thus $\sigma = \rho = |\mathbf{J}| = 0$.

A.3 Boundary Conditions

The Maxwell's equations (A.1) are valid in regions where material physical properties change continuously. In the presence of an abrupt change of the material properties, such as the interface between two media (labeled with sub-index 1 and 2), \mathbf{E} , \mathbf{H} , \mathbf{B} and \mathbf{D} have to satisfy the boundary conditions derived from the integral form of Maxwell's equations.

$$\mathbf{n}_{12} \times (\mathbf{E}_2 - \mathbf{E}_1) = 0 \quad (\text{A. 3a})$$

$$\mathbf{n}_{12} \cdot (\mathbf{D}_2 - \mathbf{D}_1) = 0 \quad (\text{A. 3b})$$

$$\mathbf{n}_{12} \times (\mathbf{H}_2 - \mathbf{H}_1) = 0 \quad (\text{A. 3c})$$

$$\mathbf{n}_{12} \cdot (\mathbf{B}_2 - \mathbf{B}_1) = 0 \quad (\text{A. 3d})$$

where \mathbf{n}_{12} is the unit normal vector pointing from medium 1 into medium 2. The vectorial equations (A.3a) and (A.3c) indicate that the tangential components of the electric field \mathbf{E} and the magnetic field \mathbf{H} are continuous. The scalar equations (A.3b) and (A.3d) state that the normal components of the electric displacement \mathbf{D} and the magnetic induction \mathbf{B} are continuous.

A.4 The Wave Equation

The electromagnetic wave equation is a second-order partial differential equation that describes the propagation of EM waves through a medium. The wave equations are derived from the Maxwell's equations. In the case that external charge and current are absent, taking the curl of (A.1a) and combined with (A.1c), we get

$$\nabla \times \nabla \times \mathbf{E} = -\mu_0 \frac{\partial^2 \mathbf{D}}{\partial t^2} \quad (\text{A. 4})$$

Applying the basic vector analysis

$$\nabla \times \nabla \times \mathbf{E} = \nabla(\nabla \cdot \mathbf{E}) - \nabla^2 \mathbf{E}$$

$$\nabla \cdot \mathbf{D} = \nabla \cdot (\epsilon \mathbf{E}) = \epsilon \nabla \cdot \mathbf{E} + \mathbf{E} \cdot \nabla \epsilon$$

as well as $\nabla \cdot \mathbf{D} = 0$ which is due to the absence of external source, (A.4) can be written

as

$$\nabla^2 \mathbf{E} + \nabla \left[\frac{\nabla \epsilon \cdot \mathbf{E}}{\epsilon} \right] - \mu_0 \epsilon_0 \epsilon_r \frac{\partial^2 \mathbf{E}}{\partial t^2} = 0 \quad (\text{A. 5a})$$

This is the wave equation for the electric field.

In a manner similar to those leading to (A.5a), we start with (A.1c) to find the wave equation for the magnetic field. The curl of (A.1c) along with $\nabla \cdot \mathbf{B} = 0$ lead to

$$\nabla \times \nabla \times \mathbf{H} = \nabla(\nabla \cdot \mathbf{H}) - \nabla^2 \mathbf{H} = -\nabla^2 \mathbf{H} = \nabla \times \frac{\partial \mathbf{D}}{\partial t}$$

Using the identity

$$\begin{aligned} \frac{\partial}{\partial t}(\nabla \times \mathbf{D}) &= \frac{\partial}{\partial t}(\nabla \times (\varepsilon \mathbf{E})) = \frac{\partial}{\partial t}(\varepsilon \nabla \times \mathbf{E} + \nabla \varepsilon \times \mathbf{E}) \\ &= -\mu_0 \varepsilon \frac{\partial^2 \mathbf{H}}{\partial t^2} + \frac{\nabla \varepsilon}{\varepsilon} \times \frac{\partial \mathbf{D}}{\partial t} \\ &= -\mu_0 \varepsilon \frac{\partial^2 \mathbf{H}}{\partial t^2} + \frac{\nabla \varepsilon}{\varepsilon} \times (\nabla \times \mathbf{H}) \end{aligned}$$

then the wave equation for the magnetic field is expressed as

$$\nabla^2 \mathbf{H} - \frac{\nabla \varepsilon}{\varepsilon} \times [\nabla \times \mathbf{H}] - \mu_0 \varepsilon_0 \varepsilon_r \frac{\partial^2 \mathbf{H}}{\partial t^2} = 0 \quad (\text{A. 5b})$$

For homogeneous medium, ε is not space dependent, thus $\nabla \varepsilon = 0$, then the wave equations (A.5) simplify to the core equations of EM wave theory,

$$\nabla^2 \mathbf{E} - \frac{\varepsilon_r}{c^2} \frac{\partial^2 \mathbf{E}}{\partial t^2} = 0 \quad (\text{A. 6a})$$

$$\nabla^2 \mathbf{H} - \frac{\varepsilon_r}{c^2} \frac{\partial^2 \mathbf{H}}{\partial t^2} = 0 \quad (\text{A. 6b})$$

where $c = 1/\sqrt{\mu_0 \varepsilon_0}$ is the speed of light at free space.

The Helmholtz equations can be derived from the wave equations with time harmonic fields. Given the field time dependence $\exp(-i\omega t)$, the time-varying electric and magnetic fields $\mathbf{E}(\mathbf{r}, t)$ and $\mathbf{H}(\mathbf{r}, t)$, with \mathbf{r} a space vector, are expressed as

$$\mathbf{E}(\mathbf{r}, t) = \mathbf{E}(\mathbf{r}) \exp(-i\omega t) \quad (\text{A. 7a})$$

$$\mathbf{H}(\mathbf{r}, t) = \mathbf{H}(\mathbf{r}) \exp(-i\omega t) \quad (\text{A. 7b})$$

Substituting the time harmonic fields (A.7) into the wave equations (A.6), we get

$$\nabla^2 \mathbf{E}(\mathbf{r}) + \varepsilon_r k_0^2 \mathbf{E}(\mathbf{r}) = 0 \quad (\text{A.8a})$$

$$\nabla^2 \mathbf{H}(\mathbf{r}) + \varepsilon_r k_0^2 \mathbf{H}(\mathbf{r}) = 0 \quad (\text{A.8b})$$

where $k_0 = \omega\sqrt{\mu_0\varepsilon_0} = \omega/c$ is the vacuum wave vector. Equations (A.8) are known as the *Helmholtz equations*.

For simplicity, here we consider a one-dimensional (1D) problem. We assume the waveguide exhibit no spatial variation in the y -direction ($\frac{\partial}{\partial y} = 0$) and the waves propagate along the z -direction. Therefore, the propagating waves are described as $\mathbf{E}(\mathbf{r}) = \mathbf{E}(x, y, z) = \mathbf{E}(x)\exp[ik_z z]$, where k_z is called the propagation constant of the traveling waves and corresponds to the wave vector component in the propagation direction. Plugging this field expression into (A.8a), we get the wave equation formulation for 1D problem as

$$\frac{\partial^2 \mathbf{E}(x)}{\partial x^2} + (\varepsilon_r k_0^2 - k_z^2) \mathbf{E}(x) = 0 \quad (\text{A.9a})$$

Similarly the 1D wave equation for the magnetic field \mathbf{H} is given as

$$\frac{\partial^2 \mathbf{H}(x)}{\partial x^2} + (\varepsilon_r k_0^2 - k_z^2) \mathbf{H}(x) = 0 \quad (\text{A.9b})$$

Given the assumption of time dependence ($\frac{\partial}{\partial t} = -i\omega$), the explicit relations between the field components of \mathbf{E} and \mathbf{H} obtained directly by the curl equations (A.1a) and (A.1c) are expressed as

$$\frac{\partial E_z}{\partial y} - \frac{\partial E_y}{\partial z} = i\omega\mu_0 H_x \quad (\text{A.10a})$$

$$\frac{\partial E_x}{\partial z} - \frac{\partial E_z}{\partial x} = i\omega\mu_0 H_y \quad (\text{A.10b})$$

$$\frac{\partial E_y}{\partial x} - \frac{\partial E_x}{\partial y} = i\omega\mu_0 H_z \quad (\text{A. 10c})$$

$$\frac{\partial H_z}{\partial y} - \frac{\partial H_y}{\partial z} = -i\omega\varepsilon_0\varepsilon_r E_x \quad (\text{A. 10e})$$

$$\frac{\partial H_x}{\partial z} - \frac{\partial H_z}{\partial x} = -i\omega\varepsilon_0\varepsilon_r E_y \quad (\text{A. 10f})$$

$$\frac{\partial H_y}{\partial x} - \frac{\partial H_x}{\partial y} = -i\omega\varepsilon_0\varepsilon_r E_z \quad (\text{A. 10g})$$

The 1D waveguide structure allows two sets of propagating wave solutions with different polarization. One set are the transverse magnetic (TM or p) modes, where the field components $H_x = H_z = E_y = 0$. Another set are the transverse electric (TE or s) modes, where the field components $E_x = E_z = H_y = 0$.

For TM modes, remembering that the 1D waveguide is invariant in the y -direction ($\frac{\partial}{\partial y} = 0$) and waves propagate along the z -direction ($\frac{\partial}{\partial z} = ik_z$), the equations (A.10) simplifies to

$$E_x = \frac{k_z}{\omega\varepsilon_0\varepsilon_r} H_y \quad (\text{A. 11a})$$

$$E_z = \frac{i}{\omega\varepsilon_0\varepsilon_r} \frac{\partial H_y}{\partial x} \quad (\text{A. 11b})$$

The H_y satisfies the TE wave equation, which reduces to

$$\frac{\partial^2 H_y}{\partial x^2} + (\varepsilon_r k_0^2 - k_z^2) H_y = 0 \quad (\text{A. 11c})$$

The equations (A.11) are the governing equations to solve the 1D TM modes.

For 1D TE modes, the analogous governing equations is

$$H_x = \frac{-k_z}{\omega\mu_0} E_y \quad (\text{A. 12a})$$

$$H_z = \frac{-i}{\omega\mu_0} \frac{\partial E_y}{\partial x} \quad (\text{A. 12b})$$

with the TE wave equation

$$\frac{\partial^2 E_y}{\partial x^2} + (\epsilon_r k_0^2 - k_z^2) E_y = 0 \quad (\text{A. 12c})$$

Appendix B Surface Plasmon Polaritons at a Single Interface

As depicted in Fig. B.1, the single planar interface between a metal, lying in $x < 0$ half space with dielectric permittivity ε_1 , and a dielectric, lying in $x > 0$ half space with dielectric permittivity ε_2 , is the most simple geometry sustaining SPPs. We assume the waves propagate along the z -direction.

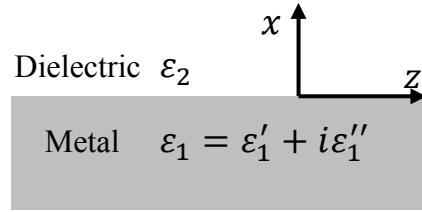


Fig. B.1 Geometry for SPPs propagation at a single planar interface between semi-infinite dielectric and metal.

Let's first check the TM solutions. The fields are described by

$$x \geq 0 \quad \left\{ \begin{array}{l} H_y^+(x) = A^+ \exp[ik_z z - k_{2x} x] \\ E_x^+(x) = \frac{k_z}{\omega \varepsilon_0 \varepsilon_2} H_y^+(x) \\ E_z^+(x) = \frac{i}{\omega \varepsilon_0 \varepsilon_2} \frac{\partial H_y^+(x)}{\partial x} = \frac{-ik_{2x}}{\omega \varepsilon_0 \varepsilon_2} H_y^+(x) \end{array} \right. \quad (\text{B. 1a})$$

$$x \leq 0 \quad \left\{ \begin{array}{l} H_y^-(x) = A^- \exp[ik_z z + k_{1x} x] \\ E_x^-(x) = \frac{k_z}{\omega \varepsilon_0 \varepsilon_1} H_y^-(x) \\ E_z^-(x) = \frac{i}{\omega \varepsilon_0 \varepsilon_2} \frac{\partial H_y^-(x)}{\partial x} = \frac{ik_{1x}}{\omega \varepsilon_0 \varepsilon_1} H_y^-(x) \end{array} \right. \quad (\text{B. 1b})$$

where k_{ix} ($i = 1, 2$) are the transverse wave vectors along the x -axis in these two media.

Note that $k'_{ix} = \text{Re}[k_{ix}] > 0$ ($i = 1, 2$) assure surface waves with fields confined to the interface. Derived from (A.8b), we get the relations

$$k_{ix}^2 = k_z^2 - \varepsilon_i k_0^2, \quad i = 1, 2 \quad (\text{B. 2})$$

The boundary conditions (A.3a) and (A.3c) require the continuity of the tangential electric and magnetic fields at the interface $x = 0$, thus

$$H_y^+(0) = H_y^-(0) \Rightarrow A^+ = A^- \quad (\text{B. 3a})$$

$$E_z^+(0) = E_z^-(0) \Rightarrow \frac{-k_{2x}}{\varepsilon_2} = \frac{k_{1x}}{\varepsilon_1} \quad (\text{B. 3b})$$

Since $\varepsilon_2 > 0$ and $k'_{ix} > 0$ ($i = 1, 2$), equation (B.3b) states that $\varepsilon'_1 < 0$ which can be fulfilled in metals and doped semiconductors at frequencies lower than their bulk plasma frequencies. Therefore the TM surface waves exist only at interfaces between materials possessing opposite signs of the real part of their dielectric permittivities.

Combining (B.2) and (B.3b), we obtain the dispersion relation of SPPs propagating at the single planar interface between two semi-infinite media

$$k_z = k_0 \sqrt{\frac{\varepsilon_1 \varepsilon_2}{\varepsilon_1 + \varepsilon_2}} \quad (\text{B. 4})$$

Similarly, we can check the possibility of TE surface mode. The fields are described by

$$x \geq 0 \quad \left\{ \begin{array}{l} E_y^+(x) = A^+ \exp[ik_z z - k_{2x} x] \\ H_x^+(x) = \frac{-k_z}{\omega \mu_0} E_y^+(x) \\ H_z^+(x) = \frac{-i}{\omega \mu_0} \frac{\partial E_y^+(x)}{\partial x} = \frac{ik_{2x}}{\omega \mu_0} E_y^+(x) \end{array} \right. \quad (\text{B. 5a})$$

$$x \leq 0 \quad \left\{ \begin{array}{l} E_y^-(x) = A^- \exp[ik_z z + k_{1x} x] \\ H_x^-(x) = \frac{-k_z}{\omega \mu_0} E_y^-(x) \\ H_z^-(x) = \frac{-i}{\omega \mu_0} \frac{\partial E_y^-(x)}{\partial x} = \frac{-ik_{1x}}{\omega \mu_0} E_y^-(x) \end{array} \right. \quad (\text{B. 5b})$$

Matching the tangential electric and magnetic fields at the interface $x = 0$, we obtain

$$E_y^+(0) = E_y^-(0) \Rightarrow A^+ = A^- \quad (\text{B. 6a})$$

$$H_z^+(0) = H_z^-(0) \Rightarrow A^+k_{2x} + A^-k_{1x} = 0 \quad (\text{B. 6b})$$

For surface waves, $k'_{ix} > 0$ ($i = 1, 2$), (B.6b) can only be satisfied with $A^+ = A^- = 0$.

This means that no surface modes exist for TE polarization. Therefore, surface plasmon polaritons only exist for TM polarization.

Appendix C Thin Film Transfer Matrix Method

C.1 Transfer Matrix Formulation

The transfer matrix analysis provides an easy formulation to study the physical properties of a multilayer planar waveguide structure, such as the one shown in Fig.C.1. All materials are assumed to be non-magnetic ($\mu = \mu_0$), isotropic and homogeneous. This waveguide consists of N layers labeled with sub-index j , $j = 1, 2 \dots N - 1$; each layer has refractive index n_j and thickness d_j ; The cover and substrate have refractive index n_0 and n_N , respectively. The interfaces between adjacent j th and $(j + 1)$ th layers locate at $x = x_j$. The mode is assumed to propagate along the $+z$ direction.

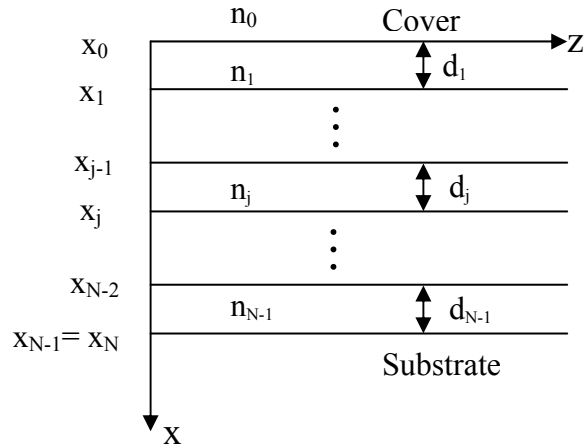


Fig. C.1 Geometry of a multilayer planar waveguide

The electric field of a TE mode and the magnetic field of a TM mode are express as

$$\text{TE: } \vec{E}(x, z) = \hat{y}E(x)\exp[-i(\omega t + \beta z)] = \hat{y}E_0\varphi(x)\exp[-i(\omega t + \beta z)] \quad (\text{C. 1})$$

$$\text{TM: } \vec{H}(x, z) = \hat{y}H(x)\exp[-i(\omega t + \beta z)] = \hat{y}H_0\varphi(x)\exp[-i(\omega t + \beta z)] \quad (\text{C. 2})$$

where β is the complex propagation constant, \hat{y} is the unit vector in the y direction, ω is the radian frequency, $\varphi(x)$ is the complex amplitude, and E_0 and H_0 are scalar constants. Substituting (C.1) and (C.2) into the wave equations (A.6a) and (A.6b) respectively, we obtain the 1D Helmholtz equation regarding the field transverse dependence $\varphi(x)$ in the j th layer,

$$\frac{\partial^2 \varphi(x)}{\partial x^2} + \alpha_j^2 \varphi(x) = 0 \quad (\text{C.3})$$

where $\alpha_j = \sqrt{\beta^2 - k_j^2}$, $k_j = n_j \omega / c$, c is the vacuum light speed.

Equation (C.3) has a simple solution composed of a forward and a backward propagating component and is expressed as

$$\varphi(x) = A_j \exp[\alpha_j(x - x_j)] + B_j \exp[-\alpha_j(x - x_j)] \quad (\text{C.4})$$

where A_j and B_j are un-determined complex amplitude coefficients.

By satisfying the continuity conditions of the electric and magnetic tangential field components at each layer interface, the field amplitude coefficients in adjacent layers can be determined as

$$\begin{pmatrix} A_j \\ B_j \end{pmatrix} = M_j \begin{pmatrix} A_{j-1} \\ B_{j-1} \end{pmatrix} \quad (\text{C.5})$$

where

$$M_j = \frac{1}{2\rho_j} \begin{bmatrix} \left(\rho_j + \frac{\alpha_{j-1}}{\alpha_j}\right) \exp(\delta_j) & \left(\rho_j - \frac{\alpha_{j-1}}{\alpha_j}\right) \exp(\delta_j) \\ \left(\rho_j - \frac{\alpha_{j-1}}{\alpha_j}\right) \exp(-\delta_j) & \left(\rho_j + \frac{\alpha_{j-1}}{\alpha_j}\right) \exp(-\delta_j) \end{bmatrix} \quad (\text{C.6})$$

$$\delta_j = \alpha_j d_j$$

$$\rho_j = \begin{cases} 1 & \text{TE} \\ k_{j-1}^2 / k_j^2 & \text{TM} \end{cases}$$

By repeating (C.6) at each layer interface, amplitude coefficients in the cover and substrate layer can be related via the matrix product

$$\begin{aligned}
 \begin{pmatrix} A_N \\ B_N \end{pmatrix} &= M_N M_{N-1} \cdots M_2 M_1 \begin{pmatrix} A_0 \\ B_0 \end{pmatrix} \\
 &= \begin{pmatrix} T_{11} & T_{12} \\ T_{21} & T_{22} \end{pmatrix} \begin{pmatrix} A_0 \\ B_0 \end{pmatrix} \\
 &= T \begin{pmatrix} A_0 \\ B_0 \end{pmatrix}
 \end{aligned} \tag{C.7}$$

C.2 Application of Transfer Matrix Method in Multilayer Waveguide

As described in Chapter 2.2.1, the modes in a multilayer waveguide structure can be classified into three categories: guided modes, radiation modes and leaky modes. Figure C.2 schematically illustrates the corresponding field distribution (dash lines) and inward- or outward-going exponential components (arrows) in the outermost regions when applying the transfer matrix method to handle these three categories of modes. Only lateral components of the mode field are indicated.

For guided modes, the two bounding media have only outgoing components with exponentially decaying field profile. For double-sided radiation modes, as shown in Fig. C.2(b), both the bounding media have counter-propagating components leading to sinusoidal field distribution. For substrate or cover radiation modes, only the substrate or cover region has two exponential components. For leaky modes, the two outermost media have only outgoing components with exponentially growing field profiles.

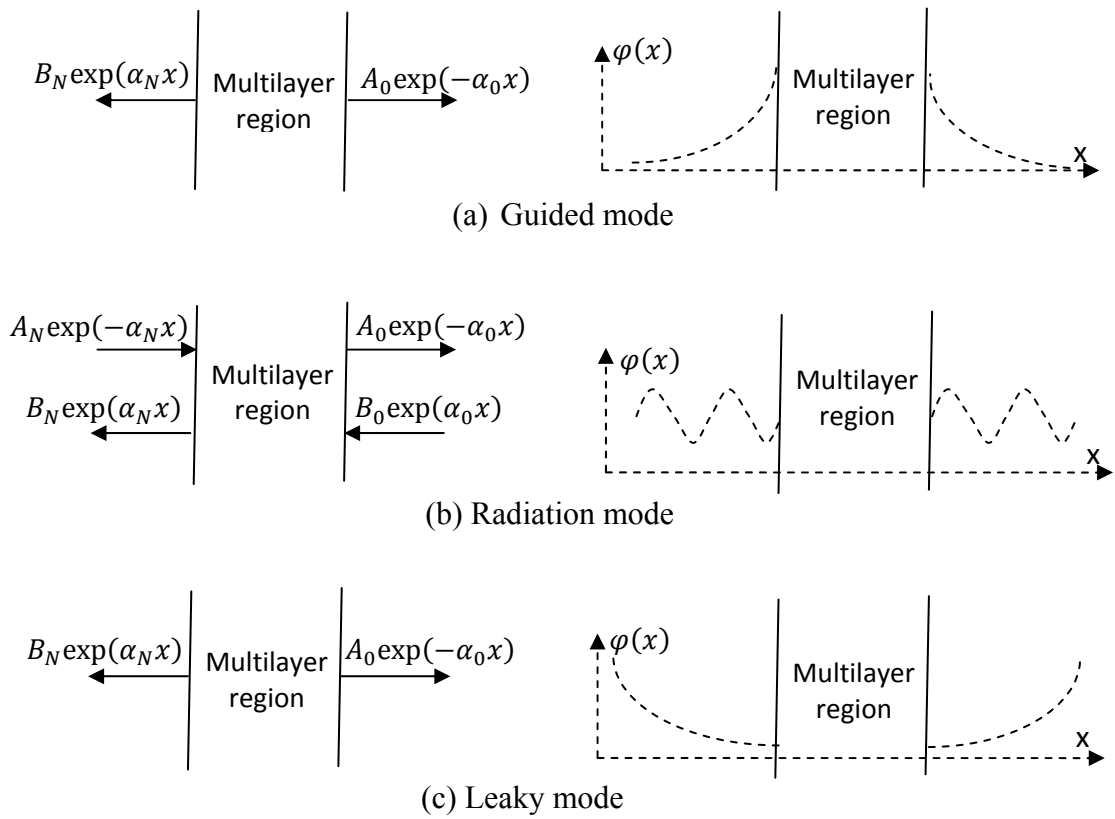


Fig. C.2 The propagating exponential components (arrow) and the field distribution profile (dash) in a multilayer waveguide outermost regions of (a) guided mode, (b) radiation mode, and (c) leaky mode. Note: Only double-sided radiation mode is shown in (b).

Appendix D Complex Root Searching: Newton-Raphson Method

The eigenvalues of non-linear equations cannot be solved analytically. The simplest and most straight-forward root-searching algorithm is Newton-Raphson method. However, its success is closely tied to a good initial guess for the solution and it can fail spectacularly.

Let's first start with a single nonlinear equation $f(x) = 0$, where x is the root of this equation. The Newton-Raphson formula consists geometrically of extending the tangent line at a current point x_i until it crosses zero, then setting the next guess x_{i+1} to the abscissa of that zero-crossing, as shown in Fig. D.1 [1].

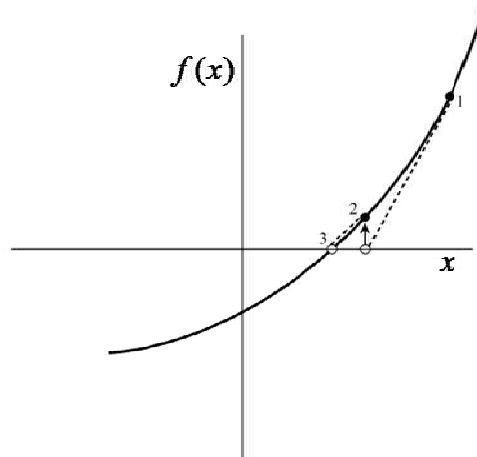


Fig. D.1 Newton's method extrapolates the local derivative to find the next estimate of the root [1].

Mathematically, the $(i + 1)$ th approximation of the root of the equation is given as

$$x_{i+1} = x_i - \frac{f(x_i)}{f'(x_i)} \quad (\text{D. 1})$$

Equation (D.1) can be written as

$$f'(x_i) = -\frac{f(x_i)}{x_{i+1} - x_i} = -\frac{f(x_i)}{\Delta x_i} \quad (\text{D.2})$$

where $\Delta x_i = x_{i+1} - x_i$ is the i th correction term between the $(i + 1)$ th and i th approximations.

The Newton-Raphson method might fail for bad-behaved functions or when root initial guess is far from the true root. For instance, too small value of $f'(x_i)$ might cause the i th correction term to diverge. The initial guess for the root might be so far from the true root as to let the search interval include a local maximum or minimum of the function, this will also makes Newton-Raphson method fail.

Newton-Raphson method is not restricted to one dimension. The method is generalizes to multiple dimensions as below.

The multidimensional vector function \vec{f} is given as $\vec{f}(\vec{x}) = 0$, where \vec{x} is a $n \times 1$ vector of variables $[x_1 \ x_2 \ \dots \ x_n]^T$. This vector function represents the following simultaneous equation set

$$\begin{aligned} f_1(\vec{x}) &= f_1(x_1, x_2, \dots, x_n) = 0 \\ &\vdots \\ f_n(\vec{x}) &= f_n(x_1, x_2, \dots, x_n) = 0 \end{aligned}$$

The iteration for \vec{x} is given by

$$\vec{x}_{i+1} = \vec{x}_i - \left[\frac{\partial \vec{f}}{\partial \vec{x}}(\vec{x}_i) \right]^{-1} \vec{f}(\vec{x}_i) = \vec{x}_i - [\mathbf{J}(\vec{x}_i)]^{-1} \vec{f}(\vec{x}_i) \quad (\text{D.3})$$

where \mathbf{J} is the $n \times n$ Jacobian matrix expressed as

$$\mathbf{J} = \frac{\partial \vec{f}}{\partial \vec{x}} = \begin{bmatrix} \frac{\partial f_1}{\partial x_1} & \dots & \frac{\partial f_1}{\partial x_n} \\ \vdots & \ddots & \vdots \\ \frac{\partial f_n}{\partial x_1} & \dots & \frac{\partial f_n}{\partial x_n} \end{bmatrix} \quad (\text{D.4})$$

Newton-Raphson method converges quadratically. This means near a root, the number of significant digits approximately doubles with each step. The very strong convergence property makes Newton-Raphson a powerful tool.

Appendix E Fundamentals of Plasma Physics

The concepts and principles of plasma physics described in Chapters 1-4 of Ref. [2] are reiterated here. The phasor in the form of $\exp(-i\omega t + i\mathbf{k} \cdot \mathbf{r})$ is assumed.

E.1 Basic Concepts of Plasma Physics

E.1.1 Plasmas in Nature

The plasma state exists as a 4th state of matter along with the gaseous, liquid, and solid states. A plasma can be composed of charged and neutral particles. Positively charged particles are ions (gaseous plasma) and holes (solid-state plasma); negatively charged particles are electrons and negative ions. Hereafter, all quantities for plasma electron (ions, neutrals) are marked by the index e (i, n) and in general by α .

The composition of the plasma can be described as *partially ionized* ($r < 1$) and *completely ionized* ($r = 1$) plasma, where the degree of ionization r is defined as $r = N_e / (N_n + \sum_i N_i)$ where N_α ($\alpha = e, n, i$) denotes particle density.

E.1.2 Plasma Parameters

(i) Plasmas in thermodynamic equilibrium and quasi-equilibrium:

The Maxwell and Fermi distribution functions

The particles constituting a plasma are in random thermal motion. The thermal equilibrium distribution of plasma particles can be described by either the Maxwell-Boltzmann distribution or the Fermi-Dirac distribution.

The Maxwell–Boltzmann distribution

When the distribution functions of plasma particles of type α with momentum p_α (or velocities) is found to be maxwellian, the plasma temperature T_α is introduced to characterize the average kinetic energy of the random particle (type α) thermal motion as

$$\frac{3}{2}k_B T_\alpha = \overline{\left(\frac{m_a v_a^2}{2}\right)} \quad (\text{E. 1})$$

where $k_B = 1.38 \times 10^{-23}$ J/K is the Boltzmann constant; T_α is the temperature of the component a [K]; v_a is the velocity of random thermal motion of particles of type a . The upper line means averaging over all particles of type a . A plasma is called isothermal if all particle types have the same temperature ($T_\alpha \equiv T$), otherwise is called nonisothermal.

For a nonisothermal plasma the Maxwell–Boltzmann distribution of type a is given as

$$f_{Ma} = N_a \left(\frac{m_a}{2\pi k_B T_a}\right)^{3/2} \exp\left(-\frac{p_a^2}{2m_a k_B T_a}\right) \quad (\text{E. 2})$$

where N_a is the concentration (density) of particles of type a . The Maxwellian distribution applies when the temperature is high enough and the density is low enough to render quantum effects negligible and the particles can be considered "distinguishable".

The Fermi–Dirac distribution

Fermi–Dirac statistics applies when quantum effects are important and the particles are "indistinguishable". The Fermi–Dirac distribution applies to fermions, i.e. particles (electrons, holes and hydrogen ions) with half-integer spin following from the

Pauli exclusion principle. Fermi–Dirac statistics become Maxwell–Boltzmann statistics at high temperature or at low concentration.

For plasma at low temperatures and high concentration, the Fermi energy exceeds the thermal energy,

$$E_{Fa} = \frac{p_{Fa}^2}{2m_a} = \frac{(3\pi^2)^{2/3} \hbar^2 N_a^{2/3}}{2m_a} \gg k_B T_a \quad (\text{E. 3})$$

where $p_{Fa} = m_a v_{Fa} = (3\pi^2)^{1/3} \hbar N_a^{1/3}$ is the momentum at the Fermi boundary, $\hbar = h/2\pi$, and $h = 6.63 \times 10^{-34}$ Js is the Planck's constant. The inequity (E.3) is satisfied at low temperatures and high concentrations $N_a \gg 5 \times 10^{15} T_a^{3/2} \cdot (m_a/m)^{3/2}$ with m denoting a free-electron mass. Thus this inequity is also called the degeneracy condition. W[hen (E.3) holds, in such a degenerated plasma, the concept of temperature as a measure of the energy of random particle thermal motion becomes senseless and is replaced by the Fermi energy E_{Fa} , which is independent of the plasma temperature and grows with the particle concentration. Therefore the general equilibrium distribution of fermions of type a over the momentum p_a is defined by the Fermi distribution as

$$f_{Fa} = 2 \left(\frac{2\pi m_a k_B T}{h^2} \right)^{3/2} \left\{ 1 + \exp \left[\left(\frac{p_a^2}{2m_a^2} - E_{Fa} \right) / k_B T_a \right] \right\}^{-1} \quad (\text{E. 4})$$

(ii) Characteristic values of plasma parameters

The characteristic values of the electron plasma in metals and solid-state plasmas in semiconductor are relevant to plasmons. The electron plasma in metals has concentrations $N_e \approx 10^{21}$ to 10^{22} cm⁻³, and the effective mass of a charge carrier is of the order of a free-electron mass ($m_e = m = 9.1 \times 10^{-28}$ g). Under these high concentrations, free electrons in metals appear *degenerate* and the condition of

degeneracy (E.3) is satisfied up to the temperature $T \approx 10^4$ K. The solid-state plasma in semiconductors, containing negative (electrons) and positive (holes) charge carriers, can be either *degenerate* or *nondegenerate*. In semiconductors with a large number of light carriers (electrons) ($N_e \gtrsim 10^{16}$ to 10^{18} cm⁻³) and effective mass $m_e^* \approx 10^{-2}m_e$, the degeneracy occurs at temperatures $T_\alpha < 10^2$ K. The degeneracy of heavy charge carrier (holes) occurs at lower temperatures, while in semiconductors with a small number of carriers ($N_e \lesssim 10^{14}$ to 10^{15} cm⁻³), the electron-hole plasma is usually *nondegenerate*. The above mentioned values of N_α and T_α are approximate and describe only approximate magnitudes.

E.1.3 Plasma Frequency and Debye Length

Plasma must be quasi-neutral, i.e. on the average, it must remain neutral for sufficiently long time and over an region of space. Thus the time and space scale of charge separation need to be considered.

The *electron Langmuir frequency*, *electron plasma frequency*, or simply *plasma frequency*, is a very important plasma characteristic parameter. It is defined as

$$\omega_p = \left(\frac{e^2 N_e}{\epsilon_0 m} \right)^{1/2} \quad (\text{E. 5})$$

The plasma frequency, being independent of temperature, is the same both for the degenerate and non-degenerate plasma and for the plasma in semiconductors $\omega_p = \sqrt{e^2 N_e m^* / \epsilon_0 m}$, where m^* is the carrier effective mass.

The quantity reciprocal to the *plasma frequency*, $\tau \sim 1/\omega_p$, is regarded as a time scale of charge separation. For time averages $t \gg \tau$, the plasma as a whole behaves like a quasi-neutral system due to the particle oscillations.

The space scale of charge separation, defined as the length on which density perturbations of charged particles may be shifted during the period of plasma oscillations as a result of the thermal motion of particles, is determined from another very important plasma characteristic parameter– the *electron Debye length* (r_{De}).

In the non-degenerate plasma,

$$r_{De} = v_{Te}/\omega_p = \sqrt{\varepsilon_0 k_B T_e / e^2 N_e} \approx 7\sqrt{T_e[\text{K}] / N_e} \text{ [cm]} \quad (\text{E. 6})$$

where $v_{Te} = (3k_B T_e / m)^{1/2}$ is the electron thermal velocity .

In the degenerate plasma, the characteristic energy of the random electron motion is the Fermi energy, therefore, $k_B T_e$ in (E.6) is replaced by $6E_{Fe}$

$$r_{De} = \left(\frac{6E_{Fe} \varepsilon_0}{e^2 N_e} \right)^{1/2} = \frac{\sqrt{3} v_{Fe}}{\omega_p} \quad (\text{E. 7})$$

For plasma quasi-neutrality, the characteristic dimensions must be much larger than the Debye length. Only under these conditions may a system of charged particles be regarded as a plasma developing the typical collective effects.

E.2 Principles of Electrodynamics of Media with Dispersion in Space and Time

E.2.1 Dispersion in Time and Space

The dependency of dielectric permittivity tensor (dielectric tensor in short) on ω (the wave vector \mathbf{k}) defines the frequency (spatial) dispersion of the electromagnetic field in the medium. Derived from Maxwell's equations, the dielectric permittivity tensor can be expressed as

$$\varepsilon_{ij}(\omega, \mathbf{k}) = \delta_{ij} + \frac{i}{\omega} \sigma_{ij}(\omega, \mathbf{k}) \quad (\text{E. 8})$$

where δ_{ij} is the unit tensor and $\sigma_{ij}(\omega, \mathbf{k})$ is the complex conductivity tensor of the medium.

For isotropic medium the dielectric tensor $\varepsilon_{ij}(\omega, \mathbf{k})$ can be written as

$$\varepsilon_{ij}(\omega, \mathbf{k}) = \left(\delta_{ij} - \frac{k_i k_j}{k^2} \right) \varepsilon^{tr}(\omega, \mathbf{k}) + \frac{k_i k_j}{k^2} \varepsilon^{lo}(\omega, \mathbf{k}) \quad (\text{E. 9})$$

and the complex conductivity tensor of the medium takes the similar form

$$\sigma_{ij}(\omega, \mathbf{k}) = \left(\delta_{ij} - \frac{k_i k_j}{k^2} \right) \sigma^{tr}(\omega, \mathbf{k}) + \frac{k_i k_j}{k^2} \sigma^{lo}(\omega, \mathbf{k}) \quad (\text{E. 10})$$

The indices i and j refer to the three space dimensions. The tensors $k_i k_j / k^2$ and $\delta_{ij} - k_i k_j / k^2$ are projectors into the directions parallel and perpendicular to the wave vector \mathbf{k} , thus $\varepsilon^{tr}(\omega, k)$ and $\varepsilon^{lo}(\omega, k)$ are called the *transverse* and *longitudinal dielectric permittivity*, respectively, and correspondingly characterize electromagnetic properties of the medium with respect to the transverse and longitudinal field. Equation (E.8) holds for both transverse and longitudinal components separately

$$\varepsilon^{tr,lo}(\omega, \mathbf{k}) = 1 + \frac{i}{\omega} \sigma^{tr,lo}(\omega, \boldsymbol{\kappa}) \quad (\text{E. 11})$$

E.2.2 Electromagnetic Waves in the Medium

With assumption of no external sources and a plane monochromatic wave in the form of $\exp(-i\omega t + i\mathbf{k} \cdot \mathbf{r})$, three homogeneous wave equations for field \mathbf{E} components are given as

$$\left[k^2 \delta_{ij} - k_i k_j - \frac{\omega^2}{c^2} \varepsilon_{ij}(\omega, \mathbf{k}) \right] E_j = 0 \quad (\text{E. 12})$$

Solutions of (E.12) exist only if the determinant of the coefficient tensor in (E.12) equals to zero,

$$\left| k^2 \delta_{ij} - k_i k_j - \frac{\omega^2}{c^2} \varepsilon_{ij}(\omega, \mathbf{k}) \right| = 0 \quad (\text{E. 13})$$

Equation (E.13) is the *dispersion equation* connecting the frequency ω with the wave vector \mathbf{k} .

For isotropic medium, given the dielectric tensor in equation (E.9), (E.13) decomposes into two equations

$$\varepsilon^{lo}(\omega, \mathbf{k}) \mathbf{E}^{lo} = 0 \quad (\text{E. 14})$$

$$\left[k^2 - \frac{\omega^2}{c^2} \varepsilon^{tr}(\omega, \mathbf{k}) \right] \mathbf{E}^{tr} = 0 \quad (\text{E. 15})$$

where \mathbf{E}^{tr} ($\mathbf{E}^{lo} = \mathbf{E} - \mathbf{E}^{tr}$) is the transverse (longitudinal) electric field component perpendicular (parallel) to the wave vector \mathbf{k} . Consequently the dispersion equation for the isotropic medium consists of two separate equations

$$\varepsilon^{lo}(\omega, \mathbf{k}) = 0 \quad (\text{E. 16})$$

$$k^2 - \frac{\omega^2}{c^2} \varepsilon^{tr}(\omega, \mathbf{k}) = 0 \quad (\text{E. 17})$$

These above two equations give the conditions of existence for longitudinal and transverse waves, respectively.

E.3 Equations of Plasma Dynamics

E.3.1 Kinetic Equation with a Field

The particle distribution function is a function of the coordinates \mathbf{p} , \mathbf{r} and t . The quantity $f_\alpha(\mathbf{p}, \mathbf{r}, t) d\mathbf{p} d\mathbf{r}$ means the number of particles of type α at time t in the phase space interval $d\mathbf{p} d\mathbf{r}$. Thus the density of particles at the point \mathbf{r} , t is given by

$$N_\alpha(\mathbf{r}, t) = \int d\mathbf{p} f_\alpha(\mathbf{p}, \mathbf{r}, t) \quad (\text{E. 18})$$

With the simplest mode that particles are assumed to be completely independent, the variation of particle distribution in a phase space volume near the point \mathbf{p} , \mathbf{r} is only due to particle inflow and outflow through the surface enclosing the volume. Since particles are neither created nor lost, we get

$$\frac{df_\alpha(\mathbf{p}, \mathbf{r}, t)}{dt} = \frac{\partial f_\alpha}{\partial t} + \frac{\partial f_\alpha}{\partial \mathbf{p}} \frac{d\mathbf{p}}{dt} + \frac{\partial f_\alpha}{\partial \mathbf{r}} \frac{d\mathbf{r}}{dt} = 0 \quad (\text{E. 19})$$

According to motion equations,

$$\frac{d\mathbf{p}}{dt} = \mathbf{F}_\alpha \quad \frac{d\mathbf{r}}{dt} = \mathbf{v} \quad (\text{E. 20})$$

where the Lorentz force acting on the particles of type α is given as

$$\mathbf{F}_\alpha = e_\alpha \left(\mathbf{E} + \frac{\mathbf{v}_\alpha \cdot \mathbf{B}}{c} \right) \quad (\text{E. 21})$$

Therefore, for charged particles of type α , the kinetic equation is expressed as

$$\frac{\partial f_\alpha}{\partial t} + \mathbf{v} \frac{\partial f_\alpha}{\partial \mathbf{r}} + e_\alpha \left(\mathbf{E} + \frac{\mathbf{v} \cdot \mathbf{B}}{c} \right) \frac{\partial f_\alpha}{\partial \mathbf{p}} = 0 \quad (\text{E. 22})$$

When deriving (E.21), the electric and magnetic fields, $\mathbf{E}(\mathbf{r}, t)$ and $\mathbf{B}(\mathbf{r}, t)$, are assumed to be given. However, inside Maxwell's equations (See Appendix (A.1)), which can determine these two fields, the charge and current density depend on the distribution functions

$$\rho = \sum_\alpha e_\alpha \int d\mathbf{p} f_\alpha(\mathbf{p}, \mathbf{r}, t), \quad \mathbf{j} = \sum_\alpha e_\alpha \int \mathbf{v} f_\alpha(\mathbf{p}, \mathbf{r}, t) d\mathbf{p} \quad (\text{E. 23})$$

Therefore, equation (E.22), where the particle distributions f_α determine the sources of the EM field supporting the phase space flow, is called the *kinetic equation with a self-consistent field* or *Vlasov's equation*. This is only valid for cases neglecting particles interaction.

E.3.2 Boltzmann Kinetic Equation

The Vlasov equation derived in the previous section is valid only if the interactions of particles can be ignored. Taking account of particle collisions causes a nonzero right-hand side of (E.19)

$$\frac{\partial f_\alpha}{\partial t} + \mathbf{v} \frac{\partial f_\alpha}{\partial \mathbf{r}} + F_\alpha \frac{\partial f_\alpha}{\partial \mathbf{p}} = \left(\frac{\partial f_\alpha}{\partial t} \right)_{col} \quad (\text{E. 24})$$

where $\left(\frac{\partial f_\alpha}{\partial t} \right)_{col}$ describing the variation of distribution function due to particle collisions is called the *collision integral*. Considering only elastic collisions, which conserve energy and momentum, the expression of $\left(\frac{\partial f_\alpha}{\partial t} \right)_{col}$ is known to be the *Boltzmann elastic collision integral*.

For a completely ionized plasma, only collisions of charged particles are essential. Here, we only present the simple idea and omit the rather complex mathematical calculation of (E.24) to reach the well-known *Landau equation*—the Vlasov kinetic equation for a completely ionized plasma taking account of two-particle coulomb collision. The *Landau equation* is solved to get the perturbed particle density function, then \mathbf{j} and σ_{ij} are obtained according to (E.23) and (E.30), and finally the corresponding dielectric permittivity is obtained through (E.8).

E.4 Dielectric Permittivity of a Homogeneous Isotropic Plasma

Without the appliance of electromagnetic fields, the distribution function of type α particle in a nondegenerate plasma is Maxwellian (See (E.2)), and in a degenerate plasma, when condition (E.3) holds, the Fermi distribution function (See (E.4)), is adopted.

First we consider the dielectric permittivity of a collisionless spatially homogeneous isotropic plasma, which can be obtained by solving the kinetic equation with a self-consistent field, i.e. Vlasov's equation. This approximation is valid for collisionless plasma with collision processes occurring on a time scale shorter than the mean free time or possessing a space scale smaller than the mean free path.

The dielectric permittivity is determined by adding a small perturbation to the equilibrium distribution function $f_{0\alpha}(p)$. Such a deviation occurs due to small fluctuations of the electric and magnetic fields $\mathbf{E}(t, \mathbf{r})$ and $\mathbf{B}(t, \mathbf{r})$ which in turn are caused by the perturbation of the equilibrium. The perturbed distribution function is written as:

$$f_a(\mathbf{p}, \mathbf{r}, t) = f_{0a}(\mathbf{p}) + \delta f_a(\mathbf{p}, \mathbf{r}, t) \quad (\text{E. 25})$$

Suppose the perturbation $\delta f_a(\mathbf{p}, \mathbf{r}, t)$ and the values of the perturbed fields \mathbf{E} and \mathbf{B} to be small. Substituting (E.25) into Vlasov's equation (E.22) and neglecting the second order terms, the linearized Vlasov for the perturbed distribution function is obtained as

$$\frac{\partial \delta f_a}{\partial t} + \mathbf{v} \frac{\partial \delta f_a}{\partial \mathbf{r}} + e_a \mathbf{E} \frac{\partial f_{0a}(\mathbf{p})}{\partial \mathbf{p}} = 0 \quad (\text{E. 26})$$

In unperturbed (equilibrium) state, the plasma is quasi-neutral with no current and charge. According to (E.23), the induced charges and currents owing to the perturbing fields \mathbf{E} and \mathbf{B} are given as

$$\rho = \sum_{\alpha} e_{\alpha} \int f_a d\mathbf{p} = \sum_{\alpha} e_{\alpha} \int \delta f_a d\mathbf{p} \quad (\text{E. 27})$$

$$\mathbf{j} = \sum_{\alpha} e_{\alpha} \int \mathbf{v} f_a d\mathbf{p} = \sum_{\alpha} e_{\alpha} \int \mathbf{v} \delta f_a d\mathbf{p} \quad (\text{E. 28})$$

The self-consistent fields \mathbf{E} and \mathbf{B} are determined by ρ and \mathbf{j} through the Maxwell's equations. The summation extends over the species index of the charged particles except the neutrals in collisionless plasmas.

Because of the linearity of (E.26) and of the field equations, there is no coupling between the Fourier expand perturbations. Thus the solution of (E.26) is written as

$$\delta f_a = -i e_a \mathbf{E} \frac{\partial f_{0a}}{\partial \mathbf{p}} (\omega - \mathbf{k} \cdot \mathbf{v})^{-1} \quad (\text{E. 29})$$

Substituting this expression into (E.28), the induced current density is given as

$$j_i = -i \sum_{\alpha} e_{\alpha}^2 \int d\mathbf{p} \frac{v_i E_j \frac{\partial f_{0\alpha}}{\partial p_j}}{\omega - \mathbf{k} \cdot \mathbf{v}} \equiv \sigma_{ij}(\omega, \mathbf{k}) E_j \quad (\text{E. 30})$$

where σ_{ij} is the conductivity tensor.

Following (E.8), the complex dielectric permittivity tensor is expressed as

$$\varepsilon_{ij}(\omega, \mathbf{k}) = \delta_{ij} + \frac{i}{\omega} \sigma_{ij}(\omega, \mathbf{k}) = \delta_{ij} + \sum_{\alpha} \frac{e_{\alpha}^2}{\omega} \int d\mathbf{p} \frac{v_i}{\omega - \mathbf{k} \cdot \mathbf{v}} \frac{\partial f_{0\alpha}}{\partial p_j} \quad (\text{E. 31})$$

E.4.1 Dielectric Permittivity of a Collisionless Nondegenerate Plasma

The longitudinal and transverse permittivities of a collisionless nondegenerate plasma obeying the Maxwellian distribution function are obtained from (E.11) and (E.31) and are expressed as

$$\varepsilon^{lo}(\omega, k) = 1 + \sum_{\alpha} \frac{\omega_{p\alpha}^2}{k^2 v_{T\alpha}^2} \left[1 - I_+ \left(\frac{\omega}{k v_{T\alpha}} \right) \right] \quad (\text{E. 32})$$

$$\varepsilon^{tr}(\omega, k) = 1 - \sum_{\alpha} \frac{\omega_{p\alpha}^2}{\omega^2} I_+ \left(\frac{\omega}{k v_{T\alpha}} \right) \quad (\text{E. 33})$$

with $I_+(x) = x e^{-x^2/2} \int_{-\infty}^x e^{\tau^2/2} d\tau = -i\sqrt{\pi/2} x W(x/\sqrt{2})$.

E.4.2 Dielectric Permittivity of a Collisionless Degenerate Plasma

In parallel, the longitudinal and transverse permittivities of the degenerate plasma obeying the Fermi distribution function at zero temperature are obtained as

$$\varepsilon^{lo}(\omega, k) = 1 + \sum_{\alpha} \frac{3\omega_{p\alpha}^2}{k^2 v_{F\alpha}^2} \left[1 - \frac{\omega}{2k v_{F\alpha}} \ln \frac{\omega + k v_{F\alpha}}{\omega - k v_{F\alpha}} \right] \quad (\text{E. 34a})$$

$$\varepsilon^{tr}(\omega, k) = 1 + \sum_{\alpha} \frac{3\omega_{p\alpha}^2}{2\omega^2} \left[1 + \left(\frac{\omega^2}{k^2 v_{F\alpha}^2} - 1 \right) + \left(-\frac{\omega}{2k v_{F\alpha}} \right) \ln \frac{\omega + k v_{F\alpha}}{\omega - k v_{F\alpha}} \right] \quad (\text{E. 34b})$$

where $v_{F\alpha} = p_{F\alpha}/m_{\alpha} = (3\pi^2)^{1/3} \hbar N_{\alpha}^{1/3}/m_{\alpha}$ is the velocity of particles of type α on the Fermi surface.

In the range of fast waves, where the phase velocity exceeds the Fermi velocities of the electrons and the ions (holes)

$$\frac{\omega}{k} \gg v_{Fe}, v_{Fi} \quad (\text{E. 35})$$

Then (E.34) takes form as

$$\varepsilon(\omega, k) = 1 - \frac{\omega_{pe}^2}{\omega^2} \left(1 + \frac{3}{5} \frac{k^2 v_{Fe}^2}{\omega^2} \right) = 1 - \frac{\omega_{pe}^2}{\omega^2} \left(1 + \frac{1}{5} k^2 r_{De}^2 \right) \quad (\text{E. 36})$$

where electron Debye length $r_{De}^2 = 3v_{Fe}^2/\omega_{pe}^2$. This function is limited to condition $k^2 r_{De}^2 \ll 1$.

The dielectric permittivity of the degenerate plasma in the limit $k^2 r_{De}^2 \gg 1$ and the range of intermediate phase velocities $v_{Fi} \ll \omega/k \ll v_{Fe}$ is beyond our interest and will not be described here.

E.4.3 Dielectric Permittivity of a Degenerate Plasma Taking Account of Particle Collisions

In fully ionized plasmas, the collision integral (See (E.24)) is used to describe charged particle collisions. To first order i.e. only consider the collision contribution from two particles (electrons and ions). The Landau kinetic equation is solved to obtain dielectric permittivity with inclusion of binary particle collisions. The details will not be presented here.

For our interesting material, the metal degenerate electron plasma gas, taking account of energy dissipation becomes much simple. According to the classical damped

oscillator theory, the longitudinal dielectric permittivity with both temporal and spatial dispersion as well as energy damping factor is expressed as

$$\begin{aligned}\varepsilon(\omega, k) &= 1 - \frac{\omega_{pe}^2}{\omega(\omega + i\gamma)} \frac{1}{1/\left(1 + \frac{3}{5} \frac{k^2 v_{Fe}^2}{\omega + i\gamma}\right)} \\ &\approx 1 - \frac{\omega_{pe}^2}{\omega(\omega + i\gamma)} \frac{1}{1 - \frac{3}{5} \frac{k^2 v_{Fe}^2}{\omega + i\gamma}} = 1 - \frac{\omega_{pe}^2}{\omega(\omega + i\gamma) - \frac{3}{5} k^2 v_{Fe}^2}\end{aligned}\quad (\text{E. 37})$$

This formula is satisfied with condition $\omega/k \gg v_{Fe}$.

References

- [1] W. H. Press, B. P. Flannery, S. A. Teukolsky and W. T. Vetterling, *Numerical recipes in C : The art of scientific computing*, Cambridge university press,(1992).
- [2] A. F. Alexandrov, L. S. Bogdankevich, and A. A. Rukhadze, *Principles of Plasma Electrodynamics*, Springer-Verlag, New York (1984).